NTNU – Trondheim
Norwegian University of
Science and Technology

SAPO-34 with Copper: Investigation of hierarchical pore characteristics and interactions with copper for catalytic applications

Trygve Dagsloth Jakobsen

Chemistry
Submission date: May 2014
Supervisor: Karina Mathisen, IKJ

Norwegian University of Science and Technology
Department of Chemistry

Trygve Dagsloth Jakobsen

SAPO-34 with Copper:

Investigation of hierarchical pore characteristics and interactions with copper for catalytic applications

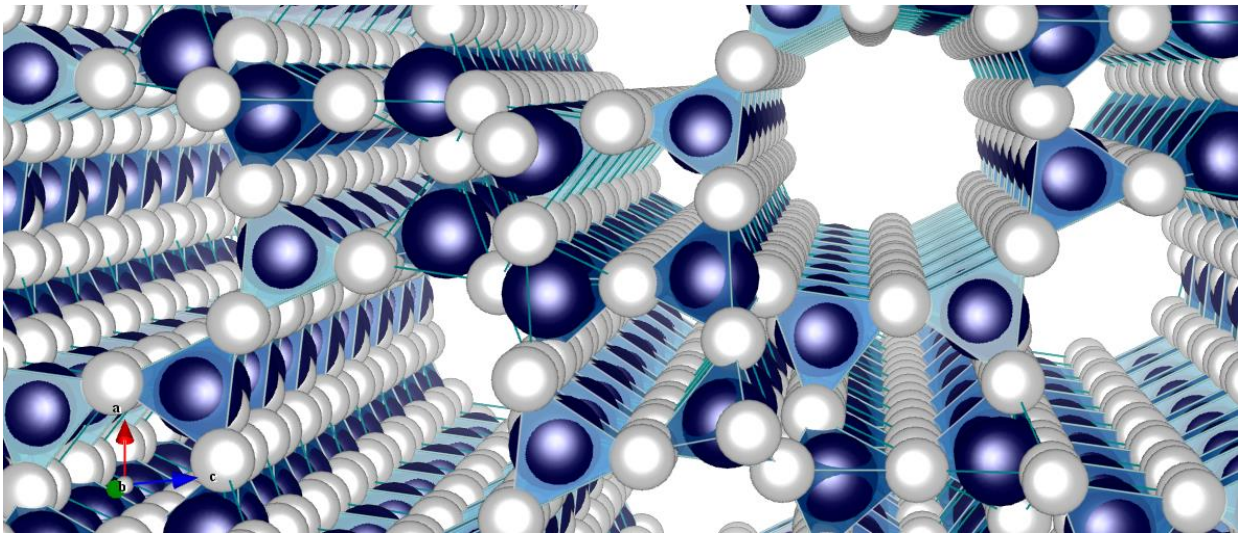

Supervisor: Associate professor Karina Mathisen

NTNU – Trondheim
Norwegian University of
Science and Technology

Acknowledgements

Firstly, I would like to thank my wonderful supervisor, Karina, for constantly encouraging me and pushing me to learn, always making sure I keep going. I think we both were a surprise to each other. Karina was, however, not my only source of knowledge and wisdom. The entire Structural chemistry group has been invaluable in the process of teaching me all that I should by now know, and giving me the experience of being part of a workplace of professionals and academics. From day one I knew that I was no longer merely a student, but part of an international community which depends on cooperation, fresh ideas, accumulated experience and communication. Furthermore, I would like to thank Tina Kristiansen, who has spent more of her personal time than anyone else trying to push theory and practice into my skull. Your patience with me is unparalleled. Katrine L. Bøyesen has helped me frequently, both with practical assignments and moral support. I hope you will enjoy the next era of your life, the post-University existence, with grown-ups. Stian Forselv has also been of great assistance. I have never met anyone more willing to always spend a half hour explaining something I wasn't originally wondering about.

I would like to thank Dr. Justin Hargreaves and his PhD student Nicholas Spencer for a wonderful and educational stay at the Department of Chemistry, University of Glasgow. Funding for the stay was granted by *A/S M. H. Lundgreens Enkes Fond* and *Norsk Hydros Forskningsfond ved NTNU*, for which I could not be more grateful. The Research Council of Norway must also be given credit for sending a lowly master-student both to Lund, Sweden and Grenoble, France (twice). I want to thank the staff of the Swiss-Norwegian Beamlines (SNBL) at the European Synchrotron Radiation Facility (ESRF) for all their assistance. The staff at beamline I811 at MaxLab was also much appreciated, as they entertained us with song and dance on our own national day. The cover illustration was created using Vesta.[1]

When it comes to making my years in Trondheim a most memorable affair, there are none more important than my fellow classmates, with whom I've procrastinated growing up. Many are worth mentioning, but most important are Cornelis van der Wijst and Kent-Ove Sylte who can always appreciate a bad joke or a good story, Ingrid Husby, my eternal lab-partner, my synchrotron buddy, Karsten Kirste and Thomas Bakka, I don't even…

My father deserves much gratitude for planting the seed of my interest in chemistry and technology. Without our Wednesday café visits I would probably have pursued a different path. Regarding the discipline required to complete the projects I have undertaken, I can thank none other than my mother. The task of instilling in me the ingredients of durability and stubbornness was in her hands. My brother too, deserves many thanks for always keeping me grounded, and giving me a sense of perspective. My dear Ida is responsible for always keeping my humor up, always making me laugh, and for that, I thank you.

Trondheim, May 2014.

Trygve Dagsloth Jakobsen

Abstract

Hierarchical SAPO-34 was produced using the dry gel conversion method,[2] where an amorphous, mesoporous silicoaluminophosphate was subjected to steam treatment with the presence of organic template. This resulted in a crystalline, microporous SAPO-34 structure, with mesopores present within crystalline particles. The pore system can be classified as bimodal or multimodal, and the term hierarchical is also often used.[3, 4] Several techniques were employed in order to determine the presence of mesopores, including thermogravimetric analysis coupled with differential scanning calorimetry (TGA-DSC), N_2-physisorption (BET) and coke deposition with subsequent microanalysis, as well as analysis by the formerly mentioned techniques. The material was found to be of moderate mesoporosity with mesopores in sizes around 6 nm. The micropore diameter inherent to the SAPO-34 structure is 0.38 nm.

Copper was ion-exchanged into the conventional and hierarchical SAPO-34, and an incorporated CuSAPO-34 was also synthesized for means of comparison. The three different types of samples were tested for activity in the reaction selective catalytic reduction of NO with hydrocarbons (SCR-HC),[5] both in dry and wet feed. The hierarchical SAPO-34 was found to be more active than conventional Cu-SAPO-34, and all samples retained good activity in wet feed as well. The hierarchical Cu-SAPO-34 was subjected to an *in-situ* red/ox cycling experiment with dry and wet feed during X-ray absorption spectroscopy (XAS). The results showed that the copper species alternate freely and reversibly between Cu(II) and Cu(I), with changes in gas feed (reducing/oxidizing). These properties were not affected by the presence of water vapor in the gas feed, which is a sign of good hydrothermal stability.

Sammendrag

Fotokjemisk smog og dårlig luftkvalitet er et økende problem i mange av verdens byer. Det forårsaker alvorlige helseproblemer, sur nedbør og forstyrrer det naturlige nitrogenkretsløpet. Nitroogenoksider (NO_X) er en klasse gasser som forårsaker smog og kommer hovedsakelig fra industri, kull- og gassdrevne kraftverk og kjøretøy.[6]

Siden 1970-tallet har treveis-katalysatoren jevnlig fått forbedret prestasjon rettet mot rensingen av utslipp som nitrogenoksider, karbonmonoksid (CO) og hydrokarboner fra bensindrevne kjøretøy. En av de største ulempene med den moderne bilkatalysatoren er avhengigheten av edelmetallene platina, palladium og rhodium, som ikke bare er veldig kostbare, men også sjeldne ressurser. Rhodium er det dyreste og mest sjeldne av de tre og mesteparten av metallet som blir utvunnet årlig går til produksjon av katalysatorer.[7]

En annen utfordring, av lignende størrelsesorden, er at treveis-katalysatoren ikke er i stand til å effektivt redusere nitrogenoksider fra dieselmotorer, på grunn av eksosens lave konsentrasjon av karbonmonoksid og hydrokarboner. Paradoksalt nok behøves det to forskjellige typer forurensende stoffer, reduktanter og oksidanter, for å rense hverandre. På grunn av dette har flere alternative katalysatorsystemer sett dagens lys, ettersom utslippskravene fortsetter å bli strengere med få års mellomrom. Tungtransport og andre store kjøretøy har begynt å ta i bruk selektiv katalytisk reduksjon med ammoniakk (NH_3-SCR). Disse systemene tilsetter ammoniakk til eksosstrømmen, og lar den fungere som reduksjonsmiddel i stedet for hydrokarboner og CO. Utviklingen av denne teknologien har vært et stort gjennombrudd for demping av NO_X-utslipp i transportsektoren, men er vanskelig å implementere i personbiler.

Midt på 1990-tallet ble silikoaluminofosfater med kobberinnhold foreslått som en mulig katalysator for deNO_X-prosessen i dieselbiler.[8] Mye av potensialet ligger i kobber-metallets pris og tilgjengelighet, som er å foretrekke fremfor edelmetaller. Spesielt den mikroporøse SAPO-34, en type molekylær-sil, besto kravene om å være både katalytisk aktiv og stabilt under de harde betingelsene. Et betydelig problem dukket likevel opp, nemlig begrensningene i massetransport gjennom porene i mikroporøse materiale. Denne egenskapen kan begrense både katalytisk konversjon og katalysatorens livstid, som begge er ufravikelige krav til et slikt system. For å forbedre diffusjonsbegrensningene, ble det eksperimentert med mer komplekse

poresystemer på 2000-tallet. Innføringen av sekundære porenettverk av større diametre, inne i de mikroporøse partiklene, viste seg å besitte betydelig bedre egenskaper i kobber-innholdende zeolitt-typer rettet mot deNO_X-prosessen.[9] SAPO-34 har også hatt stor fremgang som følge av bimodale poresystemer for industrielle formål.[10] Bimodale og multimodale poresystemer kalles gjerne hierarkiske materialer, på grunn av den stegvise oppbygningen.

Formålet med denne oppgaven er å syntetisere hierarkisk SAPO-34 og analytisk utforske materialet for å oppnå mest mulig kunnskap om poresystemet så vel som andre viktige egenskaper ved den. En rekke teknikker har blitt tatt i bruk for å utføre dette, inkludert Røntgen-diffraksjon (XRD), termogravimetrisk analyse (TGA) og N_2-fysisorpsjon. En mer uvanlig metode til dette formålet, deponering av koks på materialene har også blitt studert. Deponeringen ble etterfulgt av mikroanalyse av koksmengder og de tidligere nevnte teknikker. En vurdering av informasjonen fra de forskjellige teknikkene med hensyn på påvisning av hierarisk porøsitet vil også bli diskutert.

I tillegg har kobber blitt tilsatt til både hierarkisk og konvensjonell SAPO-34 slik at de kan sammenlignes i forhold til ytelse mot selektiv katalytisk reduksjon. Dette inkluderer testing av egenskaper som aktivitet, temperatur-avhengighet og hydrotermisk stabilitet. For å grundig studere tilstandene til det aktive kobberet i reduserende og oksiderende miljø ble Røntgen-absorpsjonsspektroskopi (XAS) benyttet. Kobberets rolle i den katalytiske reaksjonen er avhengig av dens evne til alterner mellom to forskjellige oksidasjonstilstander, som hver dekker forskjellige trinn i den katalytiske reaksjonssyklusen. XAS muliggjør observasjonen av disse oksidasjonstilstandene, så vel som antallet av og identiteten til de nærmeste nabo-atomene til Cu, samtidig som redoks-reaksjonene pågår. To faktorer er særlig viktige med hensyn på kobberets rolle; reversibelhet av tilstander i en red-oks syklus og grad reduserbarhet da Cu(I) ofte blir ansett som særlig aktivt. Disse to faktorene vil bli testet også etter tilsats av vanndamp i fødegassen, en parameter har vist seg å være desktruktiv på kobber katalysatorers effektivitet.

Table of contents

List of abbreviations

AFAC	Amplitude reduction factor
AFI	Zeolite framework type code
AlPO	Aluminophosphate
BET	Brunauer-Emmet-Teller
BJH	Barrett-Joyner-Halenda
CHA	Zeolite framework type code (Chabazite)
CHN	Microanalysis of elements C, H and N
DSC	Differential scanning calorimetry
DEA	Diethylamine
ESRF	European Synchrotron Radiation Facility
e.g.	for example
et al.	and others (citing several authors)
eV	electron volts
EXAFS	Extended X-ray absorption fine structure
FT	Fourier transformed
g	gram
GC-MS	Gas chromatography with mass spectrometer
HC	Hydrocarbon
HR-TEM	High resolution transmission electron microscopy
ICP-MS	Inductively coupled plasma mass spectrometry
i.e.	that is/meaning that
in-situ	analysis simultaneous to reaction
IUPAC	International union of pure and applied chemistry
K	Kelvin
L	Liter

LMCT	Ligand-to-metal charge transfer
m	meter
M	Molar
MFC	Mass flow controller
MFI	Zeolite framework type code
mg	milligram
min	minutes
mL	milliliter
MS	Mass spectrometer
MTO	Methanol-to-Olefins
mW	milliwatts
nm	nanometers
NO	Nitric oxide
PEG	Poly(ethylene) glycol
PEO	Poly(ethylene) oxide
PO	Propylene oxide
PSD	Pore size distribution
P-XRD	Powder X-ray diffraction
RT	Room temperature
SAPO	Silicoaluminophosphate
SCR	Selective catalytic reduction
SNBL	Swiss-Norwegian beamlines
TEAOH	Tetraethylammonium hydroxide
TEPA	Tetraethylenepentamine
TGA	Thermogravimetric analysis
TMOS	Tetramethoxysilane
TPD	Temperature-programmed desorption
TPO	Temperature-programmed oxidation

wt%	Weight percent
XANES	X-ray absorption near-edge structure
XAS	X-ray Absorption Spectroscopy
XRD	X-ray diffraction
ZSM-5	Zeolite type
Å	Ångstrøm (10^{-10} m)

1. Introduction

Photochemical smog and poor air quality is an increasing problem in many of the world's cities. It causes several severe health problems, acid rain, and disturbs the natural nitrogen cycle. Nitrogen oxides (NO_X) are a class of gases which cause smog formation, and come mainly from industry, coal- and gas-fired power plants and road vehicles.[6]

Since the 1970's the automotive three-way catalytic converter has become increasingly efficient in the cleaning of emissions of nitrogen oxides, carbon monoxide and hydrocarbons from vehicles powered by gasoline. One of the major drawbacks concerning the modern catalytic converter is the utilization of precious metals platinum, palladium and rhodium, which are not only expensive but also scarce resources. Most of the world's Rh consumption is spent in catalyst production.[7]

Another, equally challenging feature, is that the three-way converter is inefficient for cleaning nitrogen oxides from diesel engines, because the exhaust gas contains low concentrations of hydrocarbons and CO. As quite the paradox, pollutants of different types, reductants and oxidants, are required to clean each other. Therefore, several alternative catalyst systems have arisen as a response to increasingly stringent restrictions on emissions. For heavy-duty vehicles the ammonia selective catalytic reduction (NH_3-SCR) systems have become widely available. These systems add ammonia to the exhaust, which acts as a reducing agent to compensate for the lack of other reductants. This has been a big breakthrough for NO_X-abatement, but it is difficult to implement in regular-sized cars, calling for other solutions.

In the mid-1990's silicoaluminophosphates containing copper was suggested as possible catalysts for the deNO_X process in diesel cars.[8] Much of the material's potential lies in the price and availability of copper, which is preferable to the currently applied noble metals. Specially, the microporous SAPO-34 type molecular sieve proved to be both active and stable under the harsh conditions. One significant problem, however, is mass transfer limitations associated with microporous materials. These limitations can have adverse effects on both catalytic conversion and catalyst lifetime. To ameliorate the diffusion trouble, research on adding meso- and macroporosity to the microporous system began in the 2000's. Introduction

of secondary pore networks of larger sizes within the microporous particles, called bimodal or multimodal pore systems, proved effective for other copper containing zeolitic compounds in the deNO_X process.[9] SAPO-34 has also seen progress with the utilization of bimodal pore systems for industrial purposes.[10] Such kinds of bimodal and multimodal pore systems are called hierarchical materials.

The purpose with this thesis is to successfully synthesize hierarchical SAPO-34 and analytically investigate the material in order to obtain extensive knowledge about the pore system as well as other important qualities inherent to it. Several techniques have been utilized in order to confirm meso-, and/or macroporosity, including X-ray diffraction, thermogravimetric analysis coupled with differential scanning calorimetry, and N_2-physisorption. A less common method which has been applied is coke deposition on the material in combination with elemental microanalysis and the above-mentioned techniques.

In addition, copper has been added to hierarchical and conventional SAPO-34 in order to compare the two with respect to performance in selective catalytic reduction using propene as a model reductant. This includes activity testing, temperature dependence of activity, and hydrothermal stability. In order to closely inspect the states of the active copper species in reducing and oxidizing environments, X-ray absorption spectroscopy (XAS) has been applied. The role of copper in the catalytic reaction depends on its ability to alternate between two different oxidation states reversibly, which are responsible for different steps in the catalytic reaction cycle. XAS enables the probing of these oxidation states, as well as the number and identity of the nearest neighboring atoms to Cu, during the course of redox reactions.

2 Theory

2.1.Air pollution

The earth's population is growing, and with it the number of factories, power plants and cars on the road. A direct effect of this is the increasing problem of poor air quality in cities around the world. The atmospheric pollution is attributed to the emission of several species, among them carbon monoxide, hydrocarbons, sulfur dioxide, particles, and most relevant for this thesis, NO_x.[6]

NOx is a collective term for the colorless and odorless NO, and the pungent, red-brown NO_2. Both of the two gases are harmful; however NO_2 is by far the most toxic. It causes inflammation of lung tissue for weeks and months, and can, depending on exposure time and concentration, result in death. NO is not quite as toxic, but will attach to hemoglobin in blood in the same manner as CO, and hinder oxygen transport efficiency. NO_x is one of the three ingredients necessary for the formation of photochemical smog, along with hydrocarbons and ultraviolet light. Photochemical smog is indicated by the formation of ozone and other oxidants in the air, and is recognized by reduced visibility, eye irritation, cracking of rubber and deterioration of materials.[6]

Figure 2.1: Beijing on a smoggy day. Photograph by Feng Li/Getty Images[11].

Several sources contribute to the emission of NO_x. According to Roy and Baiker *et al.* more than 30 % comes from road traffic in European countries and roughly 40 % from the transportation sector in the USA.[12] Industry and power production also contribute a great deal. The main sub-source of NOx in the road traffic category consists of diesel vehicles which run on a lean-burn gas mixture, i.e. a high air/fuel ratio (>14.7). Under these oxidizing conditions the traditional three-way catalytic converter is not efficient for NO_x reduction. This is not a problem with the gasoline engine which runs on a stoichiometric mixture (air/fuel=14.7).

2.2.Catalysis

2.2.1. Principles of catalysis

A catalyst is a substance which accelerates a chemical reaction without itself being consumed. This field of study can roughly be divided into two different categories; heterogeneous, where the reactants and catalyst are in different phases, and homogeneous where they are in the same phase. This thesis will only deal with the matters of heterogeneous catalysis, in which the catalyst is generally a solid, while the reactants can be either gaseous or liquid.[13]

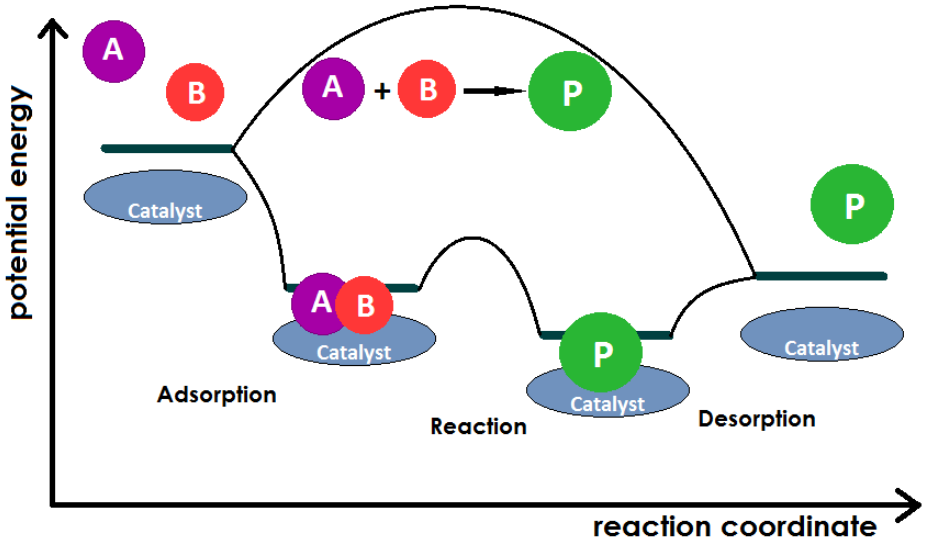

Figure 2.2: Schematic of general catalytic reaction compared to the same reaction in the gas phase.

As mentioned, catalysts accelerate chemical reactions, while the thermodynamic conditions remain unaltered. Breaking the bonds between atoms in the gas phase is often a process

requiring extremely high activation energies. In heterogeneous catalysis gaseous or liquid reactants are adsorbed on a surface, providing them with an alternative, more complex route to react and become the desired product. The goal of catalysis is for this route to obtain activation energies of minimal proportions. In heterogeneous catalysis this route is formed by way of adsorption of the reactants on the surface of the catalyst where they may react and subsequently desorb (Figure 2.2). Once the product desorbs the catalyst is reactivated and again becomes receptible for another reaction.[13]

Heterogeneous catalysts are tailored specifically for the chemical reaction in question, and must fulfill several requirements in order to be deemed economically viable as commercial applications in the fields of chemical industry, petroleum refinement, exhaust cleaning, power production, etc. The basis for any catalyst is that it must exhibit a high activity of conversion of reactants towards the desired product. This factor is also intertwined with the selectivity of the reaction. Depending on the number and complexity of different reactants, the resulting products can vary between many different compounds. It is also very important that any byproducts produced do not deactivate the catalyst in any way, and if this should be the case, a simple method of regenerating the catalyst would at the least have to be developed. If the probability of catalyst poisoning is high, the lifetime will generally be short, and this is a problem with respect to both the price of the catalyst and resulting downtime of the reactor while the catalyst is being changed. There must always be a balance between activity, lifetime and the cost of the catalyst in order for it to be useful in practical, mass-producible applications.[14]

Since many catalytic reactions take place under conditions of high temperatures and pressures, sometimes large pressure drops from one end of the catalyst to the other, it is important that the catalyst has high mechanical and thermal stability to avoid crushing, attrition, sintering of metals. High chemical and hydrothermal stability is also critical in many processes due to the harsh chemical environments and/or presence of high P/T steam.[14]

Solid catalysts can take many forms and for the sake of simplicity the more elaborate systems will not be dealt with here. Typically modern catalysts consist of an active phase where the chemical reaction takes place, a support material with high surface area which stabilizes the active phase and a promoter for improving catalyst properties such as activity, selectivity, resistance to poisoning, etc. The active species in heterogeneous catalysts are in most cases d-

band metals and metal oxides, while the support is often highly stable metal oxides, such as SiO_2, Al2O3 or ZrO_2. The support material is at the center of this thesis and will be dealt with in detail. The promoters however are not of great importance in this work.[14]

2.2.2. The automotive catalyst

The restrictions on vehicle emissions have become increasingly stringent over the past twenty years and in 2014 a new and more ambitious standard, the Euro 6,[15] is put into effect. The new emission restrictions will put even more pressure on automobile manufacturers to better their exhaust clean-up systems for removal of CO, NO_x, hydrocarbons and particles.

Most combustion engines carry the same basic exhaust system. After each combustion reaction the polluting gases are pushed out of the cylinder, through the exhaust manifold to the catalytic converter. Most cars on the road today are also equipped with one or two λ-probes[7] which measure the oxygen content after combustion. No further detail will be given to the mechanics aspect, as the focus will be on the catalytic converter.

For gasoline vehicles a "Three-way Catalyst" is installed and generally this is very effective for cleaning the pollutants in question. This is partly because the gasoline engine runs on a stoichiometric air/fuel ratio of 14.7, which balances the amounts of oxidizing and reducing species. The commercial Three-way converter consists of Pt, Pd and Rh (active phase) dispersed over an Al_2O_3 support. It is called a Three-way converter because of the three chemical reactions taking place simultaneously on the catalyst, which are listed in Table 2.1.

Table 2.1: The reactions in a three-way catalyst.[7]

Reaction	Most efficient catalysts
$\mathbf{CO + O_2 \rightarrow CO_2}$	Pt, Pd
$\mathbf{C_xH_y + O_2 \rightarrow CO_2}$	Pt, Pd
$\mathbf{NO + CO \rightarrow N_2 + CO_2}$	Rh, Pd

This combination of catalyst species and thermodynamic conditions enables the three-way catalyst to effectively clean all pollutant gases even though this is possible only within a very narrow operating window. The challenge concerning diesel vehicles (and stationary sources) is that the diesel engine runs on a lean mixture, i.e. air/fuel >14.7. As a consequence the reducing species (CO and remaining hydrocarbons) are oxidized by O_2 before they have a chance to reduce NO to N_2. Therefore diesel cars are generally equipped with catalysts containing only Platinum and Palladium, leaving the NO_x issue unaddressed.

2.2.3. Selective catalytic reduction (SCR)

A major obstacle concerning possible catalysts for diesel-engines is the very wide operational range. Exhaust temperatures vary from 100-200 °C during idling to 500 °C or more at full-throttle.[15] The oxygen concentration also varies from 3-20% depending on the mode of operation, and a SCR-catalyst would have to reduce NO and NO_2 selectively to N_2 throughout this wide parameter window. In addition it would need to withstand the water vapor (2-15%), which is inevitably present in all hydrocarbon combustion effluents. It is because of all this that a deNO_X catalyst with sufficient efficiency and flexibility across the whole operating range of the lean-burn engine has not yet been developed.[15]

The three main technologies for NO_X abatement from mobile lean-burn sources being performed research on are: direct NO decomposition, NO_X storage and/or reduction (NSR) and selective catalytic reduction (SCR).[15] Direct NO decomposition into N_2 and O_2 does not require any additional reducing agents. ZSM-5 ion-exchanged with copper is recognized as among the most active for this reaction, but unfortunately also exhibits poor stability in the presence of water at high reaction temperatures.[16] NO_X storage reduction is based on alternating between lean (oxygen-rich) and rich (fuel rich) conditions. The lean cycles are long and allows the hydrocarbons and CO to be oxidized while NO is stored on basic sites on the catalyst *e.g.* barium. Each lean cycle is followed by a short pulse of rich feed containing residual fuel species which reduce NO.[15, 17]

Selective catalytic reduction generally refers to the addition of ammonia (NH_3) or urea to the exhaust feed from an external tank, which acts as a reductant on NO.[15] The ammonia-SCR technology is practical for stationary NO_X sources and implementable on heavy-duty vehicles,

however, not very well suited for passenger cars. It requires an additional tank filled with the reducing agent, and there's also a risk of ammonia slip to the environment. This technology therefore relies on the driver's concern for the environment, because the urea/ammonia tank also requires frequent refills. NH_3-SCR is, however, not the only promising SCR technology. Selective catalytic reduction with hydrocarbons (HC-SCR) applies residual hydrocarbons in the exhaust as the reductant. HC-SCR has been studied since the mid-1990's, and copper on silicoaluminophosphates was early depicted as a viable possibility.[8, 18, 19] Cu-ZSM-5 has very high potential in terms of catalytic activity, but the material suffers from the same problems in SCR, as are present in direct decomposition. Hydrothermal stability is an important factor also with this reaction. The deactivation of Cu-ZSM-5 is frequently studied,[5] but a more stable alternative is needed, and silicoaluminophosphates have exhibited good hydrothermal stability for other reactions.[20]

2.3 Materials

Zeolites are defined as crystalline, microporous aluminosilicates, and some types can be found in nature, while others are only synthesized in the laboratory.[21] If a crystalline, microporous structure contains other elements than Si, Al and O it is defined as a zeotype. The framework structures are built as segments of tetrahedrally coordinated T-atoms, most commonly Si, Al and P, each bound to four oxygen atoms. The T-atoms therefore constitute the corners of the structures, while O-atoms function as bridges. Notably, these structures are defined by the formidable ring sizes which are large enough to be permeable to molecules. Even 14—ring (ring consisting of 14 tetrahedra) zeolites have been synthesized making possible reactions with large organic molecules.[22] In synthesis the key to creating a desired homogeneous crystalline phase is the choice of template, or organic structure-directing agent (OSDA). These are large bulky molecules, often containing amines, which force the crystalline structure to form around them. Once the material has solidified, the template molecules can be desorbed and combusted in air at high temperatures, leaving only the inorganic temperature-stable framework. Due to the large internal surface, many zeolites/zeotypes exhibit specific surface areas in the range of 400-600 m^2/g.

Within the bounds of the same crystalline structure, the molar composition of T-atoms can be varied extensively. The common zeolite ZSM-5 is produced with SiO_2:AlO_2 ratios from 20 to 280.[23] Among other properties, the composition has a profound effect on the acidity of the substance. Brønsted acid sites arise from the charge difference between the T-atoms, *e.g.* Al(III) and Si(IV). The resulting negative charge can be neutralized by adding a cation, such as the proton displayed in Figure 2.3 (right).

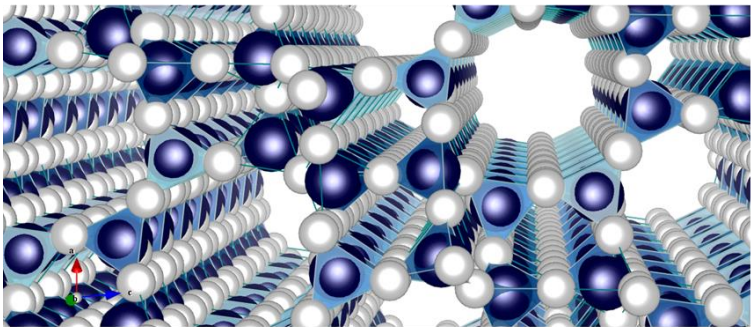

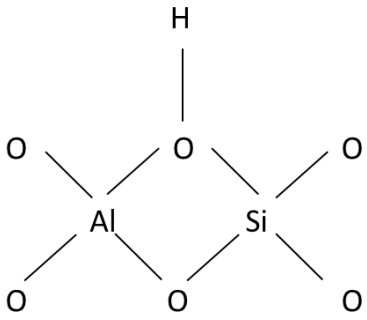

Figure 2.3: Pore system of 8-rings in the zeotype SAPO-34 (left).[1] The blue atoms indicate T-atoms. A Brønsted site is displayed as result of different-charge T-atoms (right).

Brønsted acidity is one of the properties (along with shape selectivity) which make zeolites so well suited for its many applications, such as catalytic cracking of aromatics [21], ion-exchangers in detergents,[24] membranes for separation of CO_2/CH_4,[25] etc. Ion-exchange will be dealt further attention specifically in section 2.3.3 as this is critical for the experimental work performed in this thesis.

2.3.1. SAPO-34

SAPO-34 is a zeotype consisting of Si, Al and P tetrahedral atoms and O as bridge between all T-atoms. Several different SAPO structures exist, and SAPO-34 shares topology with the mineral chabazite (CHA).[26] It is deemed a small-pore zeotype, with a micropore diameter of 0.38 nm · 0.43 nm.[27] The framework consists of distorted hexagonal prisms connected by four-membered rings, resulting in large, oval cavities called cages. Each cage is connected to 6 other cages through 8-member oxygen rings, and these rings determine the pore diameter. The size of the cage is 0.75 nm in diameter and 0.82 nm high.[28] The pore structure is three-dimensional.

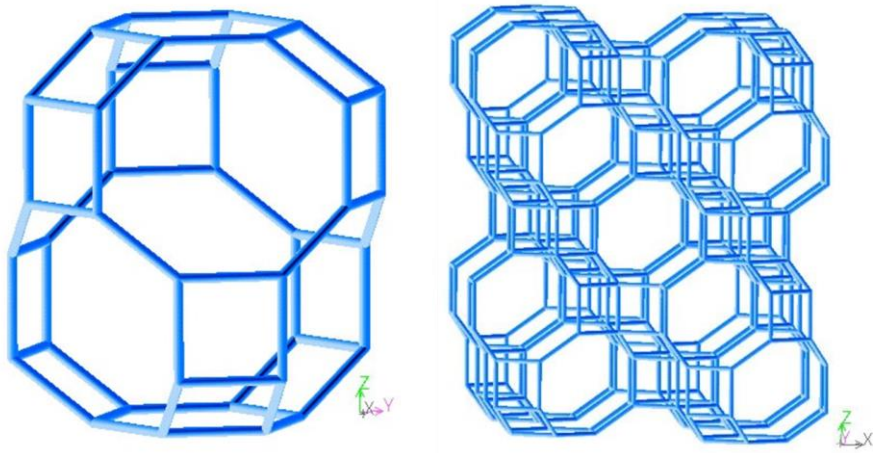

Figure 2.4: Cage structure (left) and supercell (right) of the chabazite topology. [29]

The SAPO-34 material is frequently studied and well-understood, and a multitude of patents on the synthesis and application exist.[30-32] The majority of patents and scientific work on this zeotype and the analogous chabazite has been performed with respect to the methanol-to-olefin (MTO) catalytic reaction. Specifically, SAPO-34 has proven to be an excellent catalyst for the conversion to the lighter olefins (oligomers) ethylene, propylene and butylene. In

particular the small size of the pores provides a high degree of shape selectivity, excluding the release of larger molecules from the cage.[33]

Wilson *et al.* has reported that SAPO-34 has moderate acid strength.[28] Acid site density is not universally dependent on Si content, because the Si form varies throughout samples. Within the same sample Si might be present both as single sites, which is necessary to retain acid sites, and Si island formations. Since Si only produces acid sites in the conjunction with P, the matter on the inside of the Si islands will be useless in this respect. For samples low in Si, however, the presence of Si is for the most part of the single site type. For this thesis only low Si SAPO-34 samples have been produced, and the single site can therefore be assumed.

2.3.2. Hierarchical SAPO-34

Materials such as zeolites and zeotypes tend to have relatively large surface areas due to their porous nature. Most of this surface area is situated on the inside of the structure while a small fraction is displayed on the external surface. The pores are categorized by their widths[34] as seen in Table 2.2. Hierarchical materials are structures containing both micropores and mesopores,[35] which could potentially give beneficial diffusion properties.

Table 2.2: The different pore categories defined by size.

Type of pore	Pore width
Micropore	< 2 nm
Mesopore	2 - 50 nm
Macropore	> 50 nm

Two of the main problems occurring in microporous materials during catalytic reactions are poor diffusion properties hindering over-all conversion, and inter-relatedly the deposition of carbonaceous species, or coke, which leads to pore clogging. Especially small-pore zeotypes such as SAPO-34 struggles with these challenges,[36, 37] and since the 1990s several methods have been developed in attempts to ameliorate the effects.[4]

If the catalytic activity is of a reasonably high magnitude, mass transfer will usually become the limiting factor in microporous catalysts, cancelling out the advantage that comes with high specific surface area, and any other efficiency-inducing factors. Diffusion, which is the main mechanism of mass transfer, is vital for applications in catalysis as the overall rate of reaction is only as fast as its slowest step. Molecule diffusion in intracrystalline pores is inherently slow, and consequently only the outer regions of catalyst particles will partake in the conversion. The main factors of porous diffusion in particles is explained by the Thiele modulus in the equation,[4]

$$\Phi = (r_{intrinsic}/r_{diffusion}) = L \cdot\sqrt{(k_v/D_{eff})} \ ,$$

where L is the diffusion length, k_v is the intrinsic rate coefficient and D_{eff} is effective diffusivity. When the Thiele modulus is high much of the catalyst particle is rendered unutilized, while at Φ close to 0, the entire particle is made use of. According to this formula there are two ways to improve mass transfer, the first is to decrease diffusion length and the other is to increase the degree of diffusivity, which most commonly involves modifying the pore system.

In order to decrease the diffusion length, *L*, one can either decrease the particle size or apply a thin layer of microporous material onto a mesoporous or macroporous support.[4] Nanosized SAPO-34 particles have been synthesized with microwaves in colloidal solutions,[38, 39] and it was found that catalyst lifetime was improved as a function of this. Also application of a SAPO-34 membrane onto a meso/macroporous support has been performed,[40] resulting in a composite material.

The intracrystalline molecular diffusion is analogous to the gridlock of traffic in large cities, with conflicting paths of vehicles moving towards different directions, in the same manner as reactants entering catalyst particles while products are attempting to exit. A solution to the traffic diffusion problem, which has been introduced to many cities, the superhighways, might also be a suitable method for improving the diffusional properties of zeolites and zeotypes. In practice this involves creating internal mesopores in the microporous particles, either during or after the crystallization process. The chemical reaction still takes place in the micropores, where the active catalyst phase is present, but accessibility of pore area is improved. According to Kustova *et al.*[9] the introduction of mesopores into Cu-ZSM-5 and Cu-ZSM-11

represented a substantial improvement on catalytic activity towards direct NO decomposition, which is directly related to this project.

The two methodical categories are classified as bottom-up and top-down.[4] The top-down approach generally involves performing post-synthesis procedures on zeolites. Desilication is a method which uses alkaline solutions to withdraw Si-atoms from the framework, thereby creating mesopores within the crystal. With SAPO-34 and other silicoaluminophosphates, however, it is a problem which can occur during regeneration conditions, where coke is burned in the pores, creating steam from the combustion reaction.[41, 42] Si islands can be formed and the amount of Brønsted acid sited decreases. It has been reported that SAPOs react to desilication in different manners than zeolites.[43] While zeolite stability seems to benefit from desilication, it can be detrimental to the stability of SAPO-34.

Because of the above-mentioned reasons it is desirable to investigate the possibilities of producing a hierarchical (bimodal) pore system with well-defined pores through the bottom-up approach. Synthesis of hierarchical SAPO-34 has been performed using different templates. In 2005, cross-linked polyacryliamide (C-PAM) was used as template to produce submicron-sized SAPO-34 particles which exhibited porosity in the meso- and macro-regime.[44] A template-free synthesis method was reported in 2009 which utilized the natural layered material kaolin as supplier of both silica and alumina.[10] This one-step synthesis could have tremendous potential with respect to the economic aspects, considering the simplicity of the recipe. The mesopore diameter was found to be in the range 30-40 nm, and the results were indicative of slit-shaped pores. The use of microwave technology during synthesis of nanosized particles has also been used to reduce crystallization times from several days to only a few hours.[3]

Hard templates such as carbon nanoparticles and carbon nanotubes have also been added to the synthesis mixture in order to create a bimodal pore structure in SAPO-34 crystals.[27] It was found that only the nanotubes caused a mesoporous network which is accessible from the outer regions of the particle, resulting in highly improved diffusional properties and deactivation rates during MTO reaction. The nanoparticles (d=20 nm) had no effect on the catalytic properties, on account of the isolated mesopores only being accessible through micropores.

Recently Cui *et al.*[45] prepared samples with different mesopore volumes correlated to the amount of template, in this case polyethylene glycol (PEG, average mol. weight=2000 g/mol). This is a one-step procedure, and a supramolecular nanocrystal self-assembly mechanism is proposed. In theory the PEG molecules form micelles which the nanocrystals aggregate upon. The mean mesopore diameter was found to vary slightly from sample to sample, between 10 and 25 nm. Crystallinity had been impinged on in hierarchical samples, but they were clearly phase-pure, and the effect on acid density seemed to be minimal.

Dry gel conversion was performed by Yang *et al.*[2] in 2010, which might be considered a backwards method of producing hierarchical materials. This procedure is more common in introducing mesoporosity to Zeolite Beta[46] and MFI-type zeolites.[47] In principle, an amorphous, meso/macroporous silicoaluminophosphate is initially prepared with the use of the template polyethylene oxide (PEO, 1,000,000 average mol. weight) which is essentially the same molecule as PEG (mentioned above), except that chain lengths are longer. The formation mechanism of the amorphous SAPO is called spinodal decomposition, which is a type of phase separation that happens homogeneously throughout the synthesis mixture.[48] Parameters such as template/Al ratio are critical for tuning the synthesis so that the phase separation happens at the same time as the sol-gel transition. After a gelation period, ambient drying and calcination follows, afterwhich the dry, carbon-free gel is impregnated with the TEAOH template and subjected to steam treatment. During this step the micropores are created. According to the results both mesopores and macropores of sizes ~4 nm and ~6 μm, respectively, are present in the samples. In combination with the 0.38 nm micropores inherent in the SAPO-34 structure, this synthesis procedure could be considered to produce a multimodal pore system, containing pores in the micro-, meso- and macro-regime. Likewise to the others, this hierarchical SAPO-34 system showed improved diffusional properties and deactivation rates, but a major drawback is the number of steps, and many days, required before a complete catalyst is ready. This makes the synthesis, although elegant in its own right, quite unsuitable for commercial purposes. Although, the latter argument could be used about using noble metals in catalysts too, but the situation still stands.

2.3.3. Cu introduction

There are three main methods of introducing Cu and other cations into zeotypes: ion-exchange, impregnation and incorporation. Impregnation is not included in this thesis and will not be covered here.

Ion-exchange is a large and well-documented field; however the basic principle is quite simple. The Brønsted acidic sites (H^+) are exchanged for cations, most often in basic solution. Several variations of the procedure has been performed, among others solid state ion-exchange of Cu(II) onto SAPO-34,[49, 50] and hydrothermal ion-exchange of Cu(II) onto AlPO-5.[51]

The possible cation sites in the SAPO-34 structure is displayed in Figure 2.5.[26] Computational chemistry has shown that the adsorptive properties of NO on Cu are strongly dependent on the position of Cu in the framework.[52, 53] Monovalent Cu substitutes one acid site, and divalent Cu substitutes two, however, stability of the Cu position is promoted by close proximity to framework negative charges.

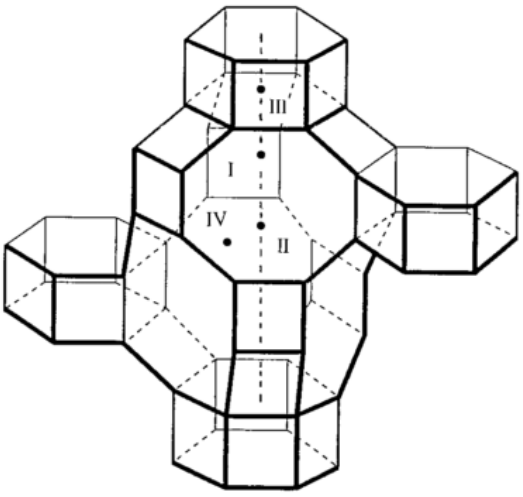

Figure 2.5: Cation sites in the SAPO-34 cage. The sites are denoted by roman numerals.[26]

Incorporation of cations into the framework of zeotypes is can be performed by adding the metal directly into the initial synthesis mixture. Theoretically, the cation would take the place

of a tetrahedral atom, bound to four oxygen atoms, also known as an isomorphous substitution. Replacing aluminum with a divalent transition cation also yields an acid site. However, characterization of the incorporated metals is generally difficult. Martínez-Franco *et al.*[54] synthesized incorporated Cu-SAPO-34 directly using a Cu-template complex in the initial mixture. The synthesis gave good control of the amount of copper in the sample, and the material also performed well for NH_3-SCR of NO_X.

2.4.X-ray Absorption Spectroscopy (XAS)

XAS is an element-specific bulk sampling technique which provides information like valence state, site geometry, neighbouring elements, coordination number and shell distances. XAS requires an intense and energy-tunable X-ray source,[55] and is an established synchrotron technique. Many scientific fields have seen advances due to the application of this technique, and especially catalysis research, has benefited greatly. Party, the reason for this is that XAS is able to provide information on structural and electronic properties during reaction conditions (in-situ).[56] While many techniques require ultra-high vacuum, XAS is able to study heavy elements, *e.g.* transition metals in gas and liquid. Another important advantage is that no long-range order is required in the samples to be inspected, making it possible to investigate amorphous materials, small metal clusters[57] and even single site metal species such as ion-exchanged copper.[51, 58, 59] These two features in combination make X-ray absorption spectroscopy very well-suited for material research towards catalytic applications.

2.4.1. Synchrotron light source

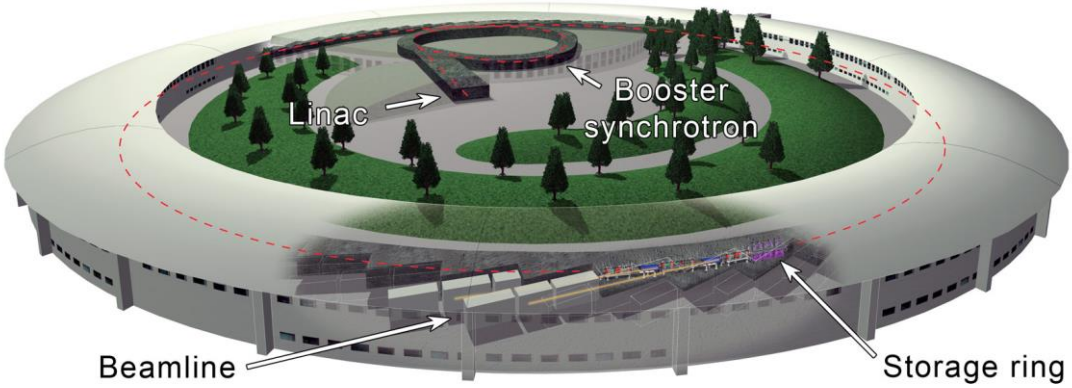

Figure 2.6: Lay-out of a synchrotron, including linear accelerator (linac), booster synchrotron, storage ring and beamlines.

Figure 2.6 displays the vital parts of a synchrotron.[60] The linear accelerator (linac) within the circle produces electrons in the form of bunches, and accelerates them to speeds high enough to enter the booster synchrotron, where they are accelerated nearly to the speed of light. A few times a day the booster synchrotron opens in order to refill the large storage ring with electrons. The storage ring is a large circular vacuum tube for the electrons to travel through,

and they can fly around it for hours before refilling is needed. Along the storage ring are several magnets with different purposes, but mainly there are three types: focusing magnets, bending magnets and undulators (or insertion devices). The focusing magnets keep the electrons flying close to their ideal orbit within the ring. The main task of the bending magnet is to bend the beam of electrons so that they move around the circle instead of straight forward, and this bending produces radiation when electrons are forced to change direction. Undulators force the electron to move back and forth laterally to the original trajectory and henceforth produce a highly focused and bright beam of X-rays which can be tuned to desired energies. The white beam produced from bending magnets and undulators is sent to individual beamlines. Before entering the experimental hutch where scientific experiments are performed, the "white light" (continuous-spectrum radiation) produced passes through an optics hutch. The optics hutch contains a set of slits and monochromators tailored to reduce the white light into a beam of light in the X-ray regime with known size and intensity, and energy levels which can be controlled continually at the request of the scientist.

2.4.2 X-ray absorption

X-ray absorption relates to the photoelectric effect where a core-level electron is ionized by the incoming X-ray exhibiting energy equal to, or higher, than the electron binding energy. The resulting drop in transmitted X-ray intensity through the sample due to absorption from the atom is detected. Figure 2.7 shows the XAS spectrum divided into the two regions, XANES and EXAFS. X-ray absorption near-edge structure (XANES) provides information about valence state and local site symmetry of the absorber, while extended X-ray absorption fine structure (EXAFS) can yield atomic distances, number of surrounding atoms and identity of the nearest atoms.

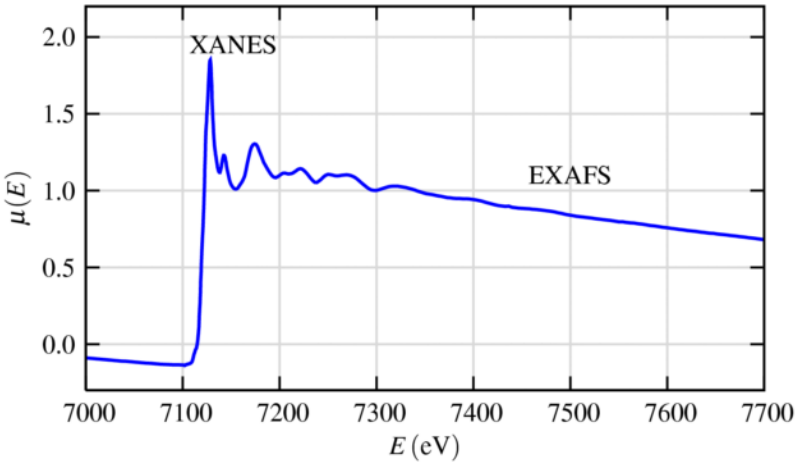

Figure 2.7: The XAS spectrum is divided into the XANES region, before and around the absorption edge, and the EXAFS region, from the edge to the end of the spectrum.[55]

2.4.3 XANES

The position of the absorption edge, E_0, is dependent on the valence state, and increases for more positive states. Copper metal (foil) has a K-edge (1s) at 8979 keV, which is within a practical energy range because only a small amount of the beam is absorbed by air. Copper species have the drawback that the true E_0 is often obscured by the pre-edge and/shoulder, however, these features can be very useful indeed for detecting the different valence states.

Figure 2.8 shows the XANES regions of four of the Cu model compounds most commonly used in comparison to synthesized samples.

Pre-edges are transitions of core-level electrons to bound, unoccupied states. They can be observed at lower energies than the absorption energy, and are present in all the models compounds shown below. The very characteristic pre-edges of metallic Cu-foil and monovalent Cu(I) arises due to a 1s-4p transition. The 3d orbital is completely filled for both of these states, and thus the 4p orbital is the lowest unoccupied orbital. Divalent model compounds CuO and $Cu(OH)_2$ exhibit pre-edges which are barely visible at 8977 eV.[61] The 3d orbital is not completely filled, and a 1s-3d transition is therefore possible. The reason why the pre-edge are so small is that they are forbidden by the Laporte selection rule, which states that for site symmetries possessing an inversion center (*i*), electronic transitions must change spin states. CuO and $Cu(OH)_2$ are of tetragonally-distorted octahedral geometry, and thus centrosymmetric (*i*), which forbids the transition.[62] It is the rise of the 1s-4p transition pre-edge which identifies reduction of Cu(II) to Cu(I), and enables qualitative analysis of the fraction of valence states.

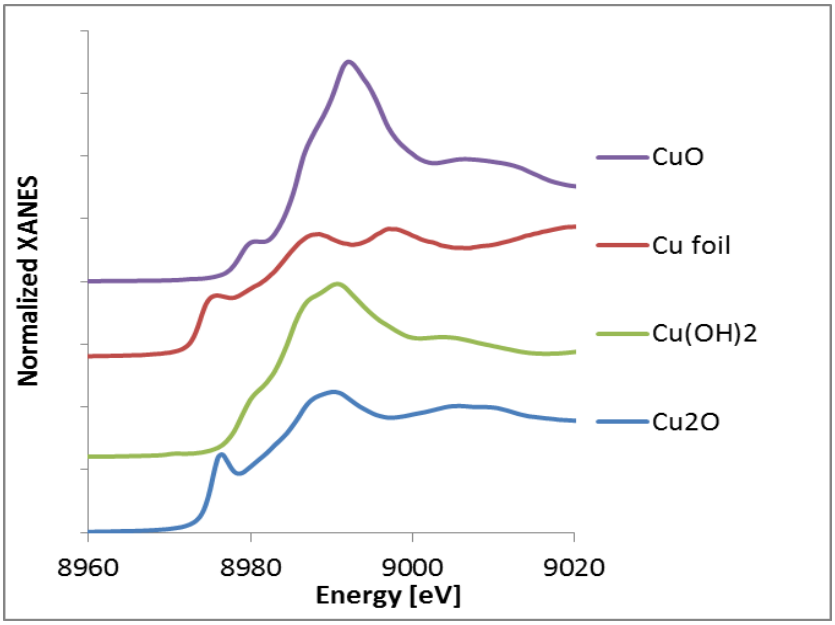

Figure 2.8: The XANES spectra of model copper compunds.

2.4.4 EXAFS

Figure 2.9 illustrates the single-scattering events of the photoelectron from the absorber (A) to the neighboring atom (B) which backscatters it back again. The photoelectron first moves as a spherical wave from the absorber, A (left), and is subsequently backscattered from the surrounding atoms (right). This creates an interference pattern with constructive and destructive sections, which causes the sinusoidal shape of the absorption curve in the EXAFS region.[56]

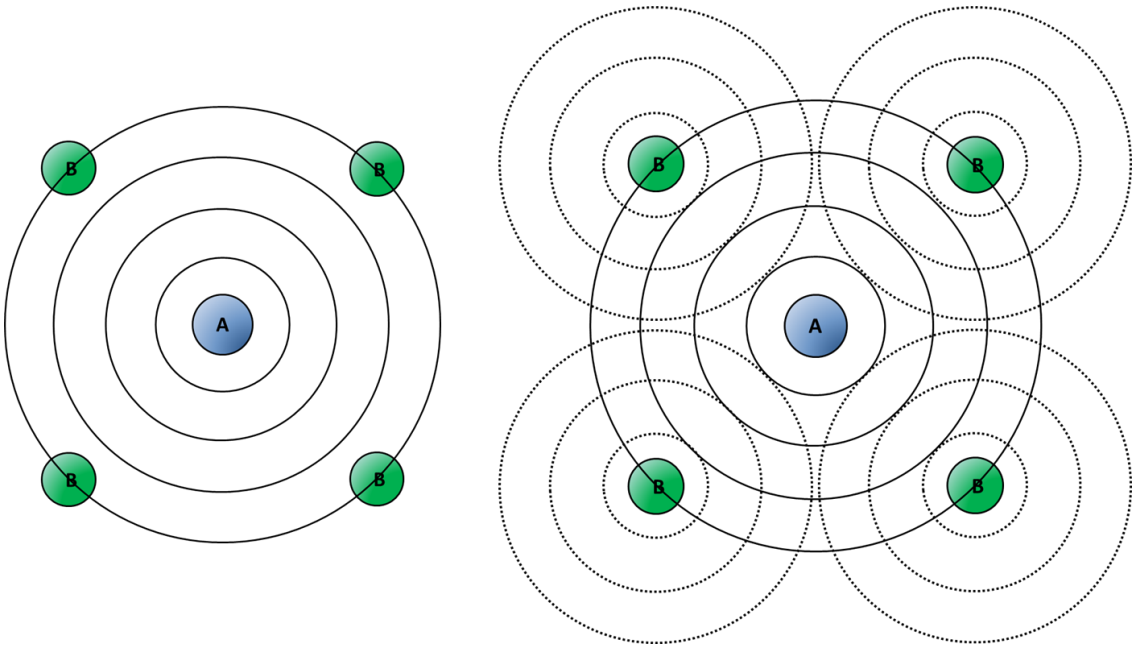

Figure 2.9: The ejection of the photoelectron and the backscattering process causing EXAFS.

The fine structure function, χ(E), determines the oscillations in the EXAFS region:

$$\chi(E) = \frac{\mu(E) - \mu_0(E)}{\Delta\mu_0(E)}$$

μ(E) is the measured absorption coeffiecient, *μ_0(E)* is a smooth background function, and *Δμ(E)* is the height of the jump. Beacause of the photoelectron wave behavior of the EXAFS the X-ray energy is converted to the wave number of the photoelectron, *k:*

$$k = \sqrt{\frac{2m(E - E_0)}{\hbar^2}}$$

E_0 is the absorption energy, m is the electron mass, and ħ is the reduced Planck's constant. $\chi(k)$ is the sum of all sinusoidal waves with different frequencies due to backscattering from several coordination shells. $\chi(k)$ is descrbed by the EXAFS equation:[55]

$$\chi(k) = \sum_j \frac{N_j f_j(k) e^{-2k^2\sigma_j^2}}{kR_j^2} \sin[2kR_j + \delta_j(k)]$$

where:

- *j* refers to the backscatterer
- $A_j(k)$ is the total amplitude
- N_j is the number of atoms in coordination shell *j* (multiplicity)
- R_j is the distance from the absorber to the atoms in coordination shell *j*
- F_j is the backscattering amplitude from an atom in coordination shell *j*
- σ_j^2 is the Debye-Waller factor which represents the thermal vibration and static disorder for backscatterer *j*
- $e^{(-2R/\lambda(k))}$ is inelastic loss due to the scattering process of neighboring atoms or the medium in between. λ is the mean free path of the photoelectron.
- $\delta_j(k)$ is the phaseshift exhibited on the photoelectron

Before synthesized samples can be refined, model compunds have to be refined in order to determine the amplitude and phase shift. These parameters can subsequently be transferred to the sample, so that the results, R_j, N_j and σ_j^2 can be extracted. The interatomic distance is related to the sine wave frequency, while the Debye-Waller factors and multiplicities are extracted from the amplitude, F_j.

The total phase of the backscattered photoelectron wave at the central atom is a product of not only the photoelectron travelling the interatomic distance twice, but also of the potentials of the absorber combined with that of the scatterer. The potential of the absorber accelerates the

photoelectron wave both when leaving and returning, and the backscatterer's potential also accelerates the wave, resulting in a reduced travel time. The time reduction is called the phase shift, and the total phase is the kinetic energy of the photoelectron, minus the phase shift.[56]

The amplitude is only a function of the backscatterer atom, and not of the absorber. It generally increases with increasing atomic number, and the position also moves towards higher values of *k*.

2.5.Other characterization techniques

2.5.1. X-ray diffraction (XRD)

X-ray diffraction is a technique most commonly applied to identify bulk crystalline phases. The X-rays are emitted from a target which is bombarded with electrons, and they are divided into two different categories. When the electrons slow down close to the target a continuous background spectrum of Bremsstrahlung is emitted. The other and more interesting category consists of narrow lines of monochromatic x-rays. The Cu Kα line has energy of 8.04 keV and a wavelength of 0.154 nm, and comes into existence when a primary electron creates a core hole which is filled by an electron from the L-shell. When the L-shell electron moves down it emits the Kα X-ray.[63]

$$n\lambda = 2d\sin\theta$$

X-ray diffraction is based on Braggs law explained by equation 2.X, where n is an integer called the order of reflection, λ is the wavelength of the X-rays, d is the distance between the lattice planes and θ is the angle between the incoming X-rays and the normal to the reflecting lattice plane.

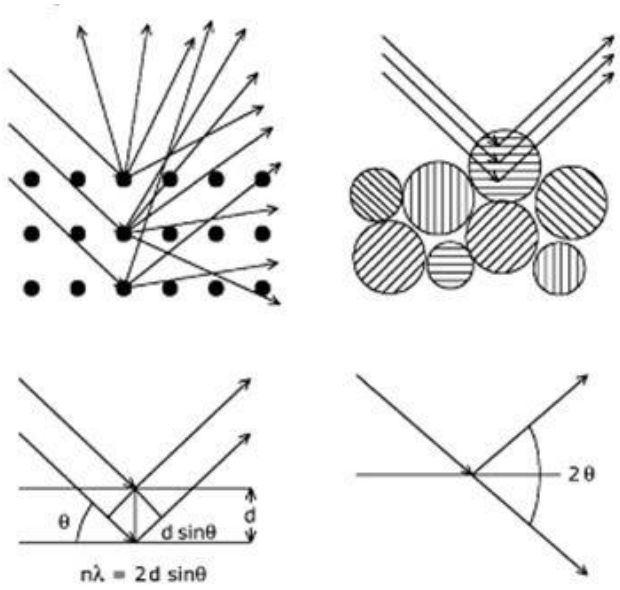

Figure 2.10: Illustration of the elastic scattering of electrons by polycrystalline powder.[63]

The XRD-instrument consists of a stationary X-ray source and a movable detector which measures the intensity of diffracted X-rays as a function of 2θ. Figure 2.11 shows the elastic scattering of X-ray photons by atoms in a periodic lattice. As seen on the upper right of the figure, only a fraction of the particles in a polycrystalline powder will contribute to the resulting diffraction pattern. This can be ameliorated by rotating the sample, and thereby allowing a larger fraction of particles to contribute and give higher peak intensity.

XRD is useful as a quick method of fingerprinting crystalline materials due to its deep-penetrating qualities, but provides little information about the surface, and the presence of amorphous phases.

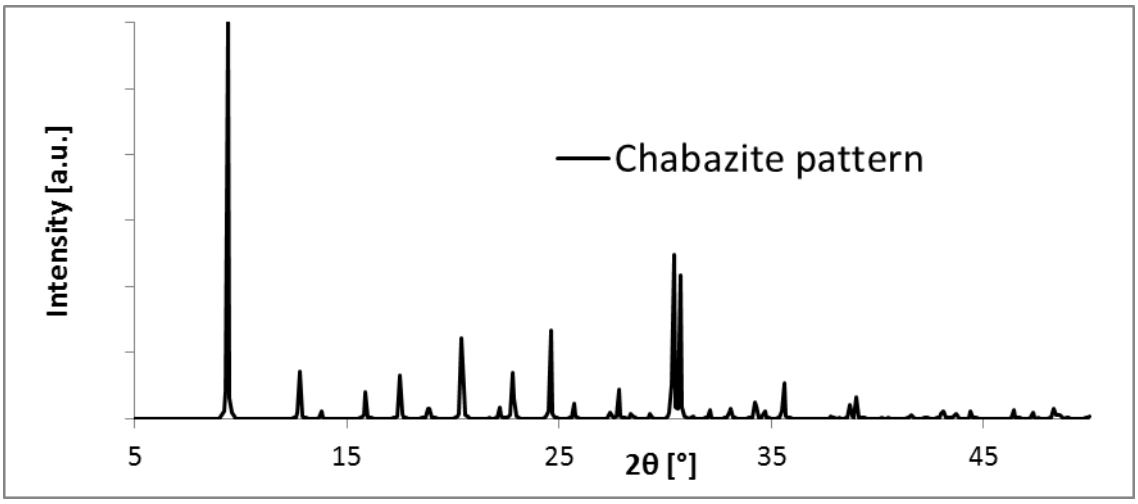

Figure 2.11: Powder XRD pattern of the mineral chabazite as calculated from the Atlas of zeolite framework types.[29]

Figure 2.11 displays the powder diffraction pattern of the zeolite chabazite[29] which shares topology with SAPO-34. The chabazite pattern from a crystallographic database can be used in comparison to the diffraction patterns of SAPO-34 samples to establish whether the sample is phasepure or not, and also to identify other phases than the desired one.

XRD cannot be used to distinguish between conventional and hierarchical SAPO-34 since they both are defined by the same crystallographic parameters, and exhibit the same peaks in the same places.

2.5.2. N2 adsorption-desorption isotherms (BET)

The BET method[64] named after Brunauer, Emmet and Teller is a well-established means of determining the specific surface area of solid materials. The method is based on the principle of physisorption of an inert gas onto the surface of the material in question, while measuring the pressure. In this thesis only N_2 is used as the adsorbate, and the measurements must be performed at 77 K which is the liquefaction temperature of N_2 at atmospheric pressure. When plotting the amount of gas adsorbed and desorbed against the relative pressure (P/P_0), where P_0 is the saturation pressure, an isotherm is observed. According to IUPAC [34] the physisorption isotherms are divided into six categories of different shapes, and four subcategories of hysteresis loops (Figure 2.12) where the gas is desorbed at lower pressures than the points of adsorption.

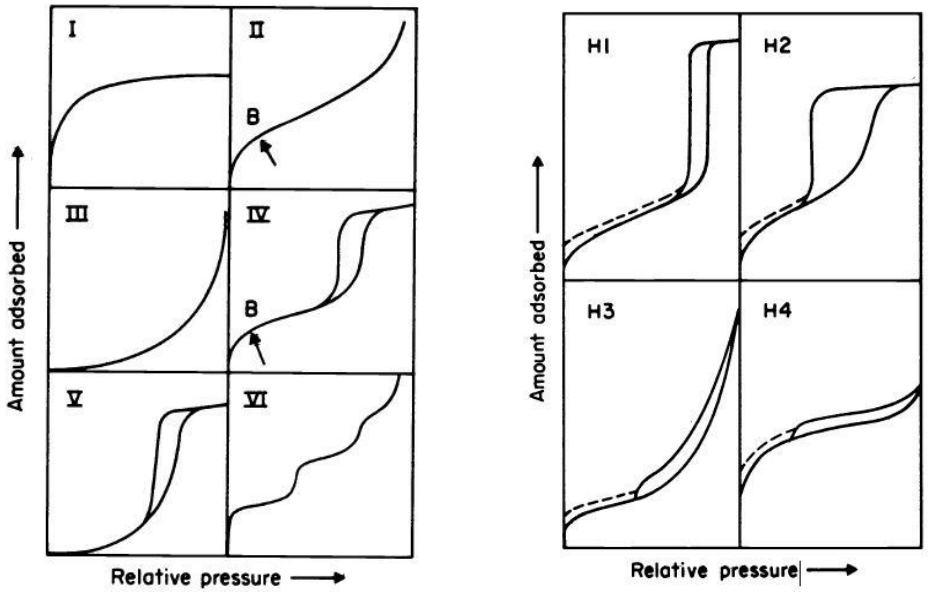

Figure 2.12: The different physisorption isotherms and hysteresis loops.[65]

From a selection of data points within the linear section of the isotherm, the slope α and intersection η are derived by linear regression. These values are inserted into the BET equation:

$$\frac{P}{V_a(P_0-P)} = \frac{1}{\chi V_0} + \frac{(\chi-1)}{\chi V_0}\frac{P}{P_0} \equiv \eta + \alpha\frac{P}{P_0} \quad ,$$

where P is the pressure, P_0 is the saturation pressure, V_a is the total amount of gas adsorbed, and V_0 is the amount adsorbed in one monolayer. χ is the ratio of desorption rate constants for the second and first layer of gas.

Isotherms of type I and III are unlikely to yield an actual value of the specific surface area, but types II and IV are well suited for this purpose. Type I isotherms are most commonly associated with microporous structures such as zeolites, while mesoporous structures usually exhibit type IV isotherms, where the hysteresis loop is attributed to capillary condensation taking place in the mesopores. The shape of the initial part of the isotherm is caused by unrestricted monolayer-multilayer adsorption on the external surface or in macropores. Hysteresis loops are generally a product mesoporosity, but the difference in shapes corresponds to different pore shapes. Figure 2.13 shows that analysis of hysteresis loops are not always straight forward with respect to trends in mesoporosity. The calculated mesopore volume for PT-0.1 lies between the volumes of PT-0.025 and PT-0.5, even though the hysteresis is almost negligible.

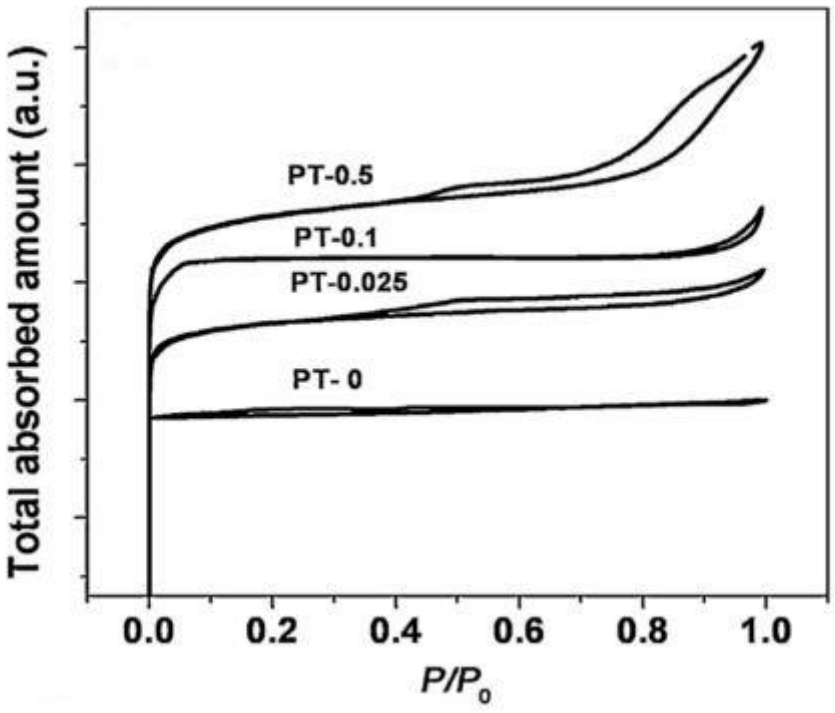

Figure 2.13: Hysteresis loops from hierarchical materials with different amounts of template in the synthesis mixture, and correspondingly different mesopore volumes. From the work of Cui *et al.*[45]

The BET theory is based on the following main assumptions:[64]

- The surface of the material consists of a great number of discrete equivalent adsorption sites (a homogeneous surface).
- At a certain vapor pressure a varying number of molecules are adsorbed on any one site. They are stacked on top of each other to form a number of layers.
- The heat of adsorption and the condensation constant (the fraction of arriving molecules per second actually condensing on empty sites) in in all layers above the first are the same and equal to those of the bulk liquid.
- At saturation the number of layers becomes infinite. As a consequence the theory is from a theoretical point of view only valid for a non-porous material.
- A molecule covered by another molecule cannot evaporate.
- There is no interaction "horizontally" between molecules in different sites.
- At dynamic equilibrium the number of molecules evaporating from a layer is equal to the number condensing on the layer below.

Physisorption measurements can also be used for determination of pore size distributions, by way of the classical pore size model developed by Barret, Joyner and Halenda (BJH).[66] For computation of the pore size distribution, the Kelvin equation is applied. Condensated liquid, in this case N_2, within the mesopores, will have a meniscus. The curvature of this meniscus is directly related to the pore width, and its shape is dependent on the shape of the pore. Cylindrical pores will generally cause the meniscus to be hemispherical, while slit-shaped pores give rise to a hemicylindrical meniscus.[67]

One of the most misinterpreted results from N_2-physisorption is the tensile strength effect (TSE).[35] It exhibits itself as a narrow peak in the pore size distribution, at 3.8 nm, or roughly 4 nm for less accurate instruments. The TSE phenomenon is much more common to observe on the desorption branch than on the adsorption branch, and is caused by a forced closure of the hysteresis loop.

2.5.3 TGA-DSC

Thermogravimetric analysis is a technique which monitors the mass loss of a sample during heating in continuous gas flow.[68] The TGA instrument measures only the mass of the sample, however, a mass spectrometer (MS) can offer complementary information by analysis of effluent gases. Automatic calculations of the first derivative of mass loss can also be adequate to make analysis clearer.

The differential scanning calorimetry (DSC) which often accompanies the TGA, detects whether the reaction taking place in the sample chamber is endothermic or exothermic. During endothermic reactions, such as desorption of water, the DSC-peak corresponding to a mass loss will point to a more negative value than the normal. Combustion reactions, which are exothermic, will show positive peaks.

Relevant for the project, there are two main categories of measurements depending on what type of information is required. Temperature-programmed oxidation (TPO) is performed with air- or oxygen-rich flow, to monitor oxidation, e.g. combustion of organic species. TPO can be applied to measure coke-deposition or monitor template removal. Temperature-programmed desorption is performed in an inert gas flow, such as argon, and consequentially no combustion will occur. Hence all mass loss happens via desorption of species from the surface and pores.

3. Experimental

3.1.Synthesis

3.1.1. SAPO-34

Conventional SAPO-34 was synthesized by the hydrothermal method. Firstly, all reactants were weighed in beakers and immediately covered with parafilm: deionized water (H_2O, 35.50 g), phosphoric acid (H_3PO_4, 15.42 g), aluminum isopropoxide ($Al((CH_3)_2CHO)_3$, 27.210 g), silica (Ludox, 40 wt% suspension in water, 6.00 g) and tetraethylammonium hydroxide (TEAOH, 40 wt%, 42.21 g) to yield the theoretical gel composition:

$Al : P : 0.3Si : 0.9TEAOH : 28H_2O$.

The phosphoric acid was weighed in a large beaker which was to eventually contain the entire synthesis mixture. The beaker was set to stir with a magnetic stirrer and the water was carefully added to the acid. The aluminum isopropoxide was added and stirred by hand until dissolved enough for the magnetic stirrer to function properly. The mixture was left to stir for approximately 1 hour. The silica was then added quickly, and the pH measured to be 3-4. The TEAOH was subsequently added and once dissolved the pH was indicated to be 13. The mixture was set to stir for 30 minutes whereupon it was divided into two and transferred to two stainless steel autoclaves with Teflon liner. Both autoclaves were approximately half full, and were heated at 190 °C for 72 hours and 96 hours, respectively.

The resulting samples were washed with deionized water and centrifuged before being transferred to a petri dish and dried overnight at 100 °C. The dry powder was mortared and calcined at 550 °C for 17 hours in order to remove the organic species.

3.1.2. Hierarchical SAPO-34

Theoretical gel composition:

$Al : P : 0.4Si : 31H_2O : 5C_2H_5OH : 6{\cdot}10^{-5}PEO : 3PO$

Hierarchical SAPO-34 was synthesized by dry gel conversion of amorphous silicoaluminophosphate as described by Yang *et al.*[2]. Silicoaluminophosphate was prepared

by mixing the following substances in the order they are mentioned while stirring with a magnetic stirrer: Aluminum chloride hexahydrate ($AlCl_3 \cdot 6(H_2O)$, 42.70 g), tetramethoxysilane (TMOS, 10.00 g), diammonium hydrogen phosphate ($(NH_4)_2HPO_4$, 23.31 g), deionized water (H_2O, 100.01 g), ethanol (C_2H_5OH, ~96%, 40.00 g), polyethylene oxide (PEO, 1.00 g) and propylene oxide (PO, 26.00 g) to yield the theoretical gel composition:

$Al : P : 0.4Si : 31H_2O : 5C_2H_5OH : 6 \cdot 10^{-5}PEO : 3PO.$

The resulting gel was transferred to two identical plastic centrifuge tubes and sealed. The tubes were left to gelate at 60ºC for 48 h. The caps were subsequently removed from the tubes and the wet gel was left to dry at 60ºC in air for 72 h. The samples were then mortared and calcined for 8 h at 550ºC.

The resulting amorphous silicoaluminophosphate powder was impregnated with tetraethyleneammonium hydroxide (TEAOH, ~40%) and transferred to stainless steel autoclaves with Teflon liner. Within the autoclave the samples were subjected to steam treatment at 200ºC for 72 h. The samples were then centrifuged and washed with deionized water, and dried in petri dishes covered with foil over night at 100ºC. Calcination followed at 550 ºC for 8h to remove the organic structure directing agent from the pores.

3.1.3. Ion exchange

Six conventional and three hierarchical samples of SAPO-34 were ion-exchanged with either copper dinitrate ($Cu(NO_3)_2$) or copper tetramine ($[Cu(NH_3)_4]^2$). The total number of samples ion-exchanged thus amounts to twenty. The different variations are listed in Table 3.1.

Table 3.1: Summary of all ion-exchanged conventional and hierarchical samples, including variable parameters: crystallization time, template, Si:Al ratio, Cu precursor and Cu concentration.

Pore system	Sample name	Crystal-lization time [hrs]	Template	Si:Al molar ratio	[$Cu(NO_3)_2$] in ion-exchange [mol/L]	[$Cu(NH_3)_4^{2+}$)] in ion-exchange [mol/L]
Conventional	SAPO34-1	96	TEAOH	0.2	0.03	0.03
Conventional	SAPO34-2	192	TEAOH	0.2	0.03	0.03
Conventional	SAPO34-3	48	DEA	0.2	0.03	0.03
Conventional	SAPO34-4	48	DEA	0.2	0.03	0.03
Conventional	SAPO34-5	72	TEAOH	0.3	0.03	0.03 & 0.015
Conventional	SAPO34-6	96	TEAOH	0.3	0.03	0.015
Hierarchical	H-SAPO34-1	72	TEAOH	0.4	0.03	0.03
Hierarchical	H-SAPO34-2	72	TEAOH	0.4	0.03	0.03 & 0.015
Hierarchical	H-SAPO34-3	72	TEAOH	0.4	0.03	0.03

A 250 ml solution of $Cu(NO_3)_2$ was made in the concentrations listed in Table 3.1 from a $Cu(NO_3)_2 \cdot 3H_2O$ salt. This solution was distributed into two beakers in equal amounts. One beaker was left unchanged for ion-exchange, while the other was set aside for pH adjustment. Concentrated ammonia (NH_3) was diluted with deionized water to a concentration of 5 M and added dropwise and carefully into the second beaker while stirring. Once the light blue liquid had turned dark blue the solution was confirmed to be $[Cu(NH_3)_4]^{2+}$ by measuring the pH, and no more ammonia was added. 15 ml of $[Cu(NH_3)_4]^{2+}$ was added to one beaker and 15 ml of $Cu(NO_3)_2$ to another. 0.5 g of zeotype sample was added to each beaker and they were set to stir at room temperature for 24 hours. The color difference between the two slurries is shown in Figure 3.1. After 24 hours they were washed with deionized water and centrifuged 5-8 times, before being transferred to a petri dish and left to dry overnight at 100 °C. This is a general procedure for all ion-exchanges performed.

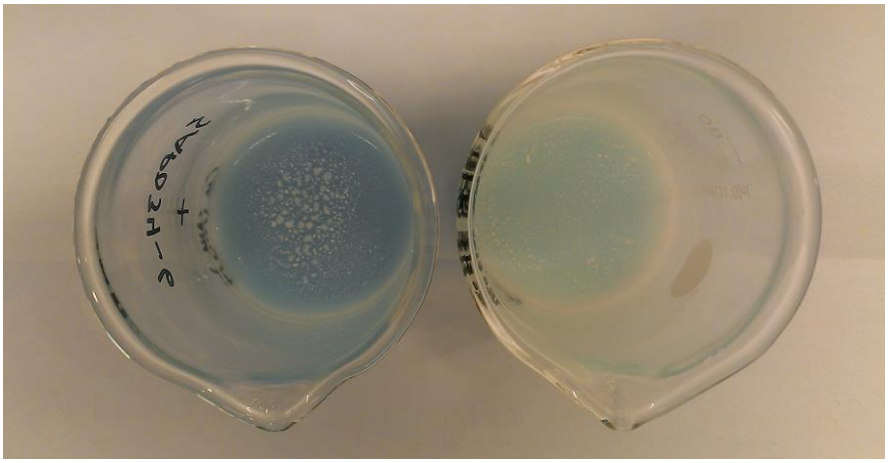

Figure 3.1: Samples in solutions of $[Cu(NH_3)_4]^{2+}$ (0,03 M, left) and $Cu(NO_3)_2$ (0,03 M, right) after 24 hours ion-exchange.

3.1.4. Incorporated Cu-SAPO-34

Incorporated Cu-SAPO-34 was synthesized directly by the hydrothermal method as described by R. Martínez-Franco *et al.*[54]. Firstly, tetraethylenepentamine (TEPA, ~99%, 3.41 g) was introduced to a beaker. Deionized water (H_2O, 2.01 g) and copper(II) sulfate monohydrate

($CuSO_4 \cdot H_2O$, 4.49 g) was added to the same beaker while stirring by magnetic stirrer. The mixture was left to stir for 2 hours until homogeneity was obtained.

Deionized water (H_2O, 24.18 g) and phosphoric acid (H_3PO_4, 85 wt%, 9.22 g) was then added slowly to the mixture and stirred for 5 min, pH resulting in pH~2. Silica (Ludox, 40 wt%, 5.40 g) and alumina (Pseudoboehmite, 71.8 wt% Al_2O_3, 7.10 g) were added simultaneously while stirring. Lastly, diethylamine (DEA, 99 wt%, 5.27 g) was added quite quickly. The mixture, in liquid form, was transferred to an autoclave with a Teflon liner and heated at 150°C for 168 hours (7 days). This yielded a theoretical gel composition of:

Al : 0.8P : 0.36Si : 0.18Cu : 0.18TEPA : 0.72DEA : 18 H_2O.

The resulting gel was centrifuged and washed with deionized water and transferred to a beaker. The sample was dried overnight at 100°C in the dish covered with foil. The sample, in powder form, was mortared and part of it was calcined in air for 17 hours at 550°C to remove the template.

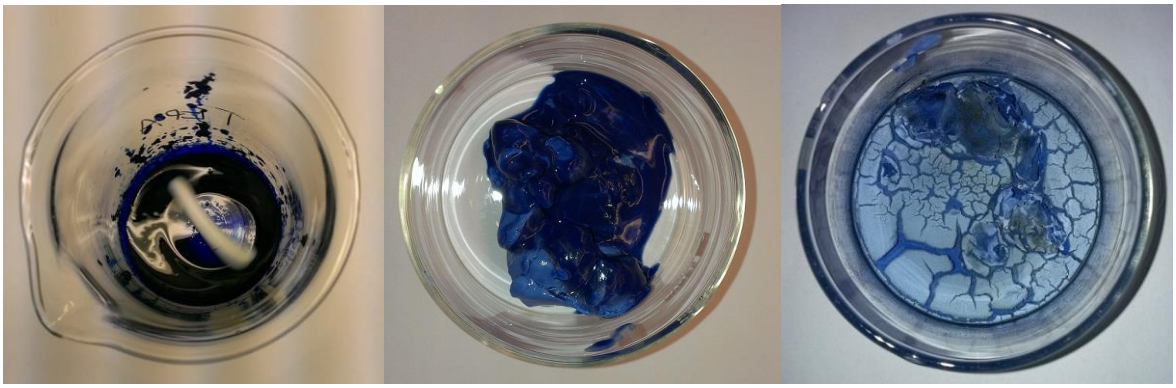

Figure 3.2: Different steps of the synthesis; on the left is the Cu-TEPA mixture while stirring, the middle shows the gel after hydrothermal treatment and the right is after washing and drying.

3.2.Characterization

3.2.1. X-ray diffraction (XRD)

For XRD-measurements a Bruker AXS D8Focus is used. It uses a Cu Kα X-ray tube and solid state LynxEye™ detector and scintillation detector. The measurement parameters include angles from 5 to 50º 2Θ with a slit opening of 0.2 mm and a step size of 0.02º. The counting time was 0.1 seconds per step. The X-ray diffractograms were used to identify the crystalline

phase, and degree of crystallinity. All SAPO-34 samples were compared to the zeolite chabazite (CHA), which is found in the database.

3.2.2. Inductively coupled plasma mass spectrometry (ICP-MS)

ICP-MS elemental analyses were conducted by Syverin Lierhagen (IKJ) on a High Resolution Inductively Coupled Plasma ELEMENT 2, connected to a mass spectrometer. These analyses were performed mainly in order to determine the copper loading in weight percent (wt%) in the samples, and partly to see if the fractions of Al, Si and P were in correspondence with the theoretical composition in the synthesis mixture.

Between 20 and 45 mg of sample was weighed out, transferred to a Teflon tube (25 ml) and decomposed in concentrated nitric acid (HNO_3, 1.5 ml) and concentrated hydrofluoric acid (HF, 0.5 ml). The resulting solution was transferred to a larger Teflon canister and diluted with deionized water until the entire solution weighed 216.6 g. A 16 ml Teflon tube was washed and subsequently filled with the sample solution. Three tubes without sample (blanks) were also prepared for correction of the samples.

3.2.3. TGA-DSC

NTNU:

Thermogravimetric analysis (TGA) and differential scanning calorimetry (DSC) was performed using a Netzsch STA 449C connected to a Netzsch Aërlosqms 403C mass spectrometer. 10-20 mg of as-synthesized sample was heated in synthetic air (80 ml/min) and argon (25 ml/min) from 30 to 650 °C at a ramping rate of 5 °C/min. Loss of mass from the sample was measured in percent of initial sample, and simultaneously DSC was used to measure the corresponding difference in heat. The mass spectrometer detected the individual masses of the evaporated species.

University of Glasgow:

Samples which had undergone coke deposition during MTO reaction were analyzed with a TA Instruments Q500 thermogravimetric analyzer. All samples were analyzed using a method of temperature-programmed oxidation (TPO). The samples were heated in argon and air at a flow rate of 50 ml/min and ramp rate of 10 °C/min from 20 to 800 °C. Typically 8 mg of sample was used.

Selected samples were also analyzed with a method of temperature-programmed desorption (TPD) without oxygen present. The samples were heated in argon only from 20 to 1000 °C at a ramp rate of 10 °C/min.

3.2.4. N_2 adsorption-desorption (BET)

N_2 adsorption and desorption was performed with a Micromeritics Tristar 3000 Surface area and porosity analyzer. Calcined powder samples between 0.1-1g were weighed in the sample tubes which were handled with cotton gloves to avoid grease contamination and static charging. All samples were dehydrated in a Micromeritics VacPrep061 for more than 18 hours before analysis. Dehydration was performed under low vacuum at a temperature of 250 °C. After dehydration the sample tubes were weighed quickly and the difference was recorded before they were mounted to the analyzer.

All sample tubes were fitted with isothermal jackets which adsorb nitrogen to ensure a stabile temperature around the tube. With the same purpose in mind the thermos surrounding the sample tubes was filled with liquid nitrogen the day before. As mentioned in the theory section it is important that N_2-adsorption-desorption is performed at 77 K (-196 °C) which is the boiling point of nitrogen at ambient pressure.

The specific area was calculated by the BET method assuming a cross sectional area of 16.2 $Å^2$ for the nitrogen molecule. The BJH method was used to determine the pore size distribution.

3.2.5. Coke deposition during MTO reaction

In order to obtain information about stability in relation to deactivation involving deposition of carbonaceous species, the SAPO-34 samples were tested in the methanol-to-olefin (MTO) reaction. The reactions and all subsequent sample analyses were performed at WestCHEM School of Chemistry at the University of Glasgow. The MTO reaction was performed in the Laboratory of Professor Justin Hargreaves,[69] with the guidance of PhD student Nicholas Spencer.

A fixed bed micro-reactor was used for the MTO reaction, and the reactor consisted of a quartz reactor tube with a sinter in the center. The tube was fixed vertically and the sample

was placed on top of the sinter. Due to the difference in density between the samples, sample size was measured in volume instead of weight. A bed depth of 2 mm of sample was measured out in the reactor tube, with an inner diameter of 8 mm. All samples had previously been sieved so that the particle size was in the range of 0.25-0.42 mm.

The sample was first heated in 40 ml Ar to the reaction temperature of 300 °C, before a flow of methanol (0.03 ml/min) was introduced via a Knauer K501 HPLC-pump. The reaction proceeded for 5 hours. The gas mixture produced a total Gas Hourly Space Velocity (GHSV) of 3088 h^{-1} and a methanol concentration of 32 %.

The temperature was regulated using a tube furnace with a thermocouple placed in a silica thermowell placed <10 mm above the sample. Reaction lines before and after the reactor tube were kept at ca. 300 °C.

3.3.Catalysis measurements

3.3.1. SCR-HC-deNOx

Figure 3.3 illustrates the set-up for SCR-HC-deNO_x measurements. Helium, NO, O_2 and C_3H_6 was supplied by individual gas cylinders. The following concentrations were applied using mass-flow controllers: 0.2 % NO, 2 % O_2, and 1.3 % C_3H_6. Helium was used as a balance gas to achieve total flow of 15 ml/min. This renders a weight hourly space velocity (WHSV) of 700 g g_{cat}^{-1} h^{-1}. Manual ball valves are also in place to avoid any possible leakage through the MFC reaching the rest of the system.

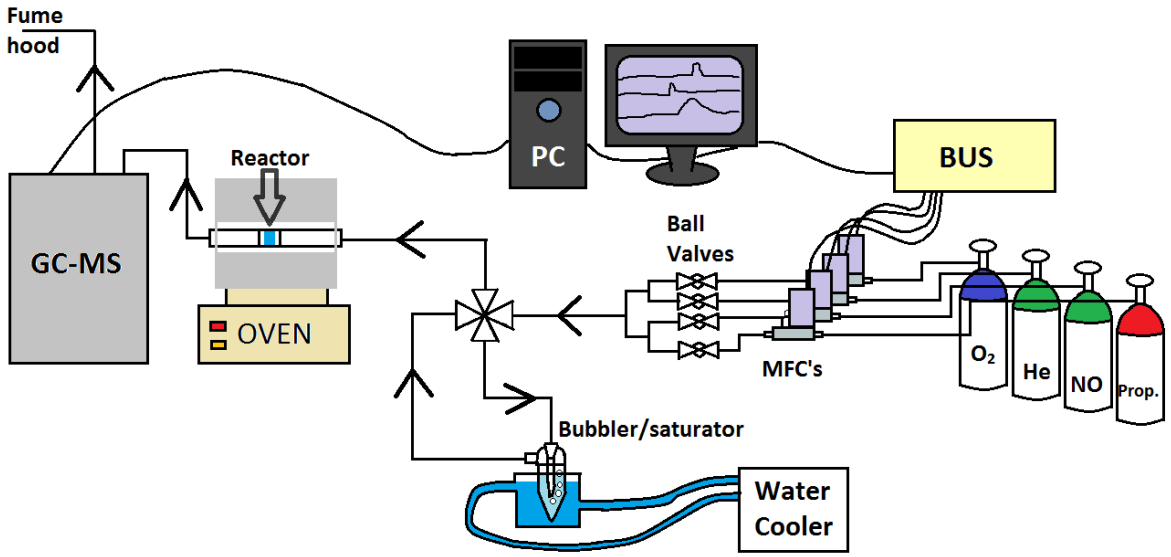

Figure 3.3: Set-up for catalysis measurements.

Water vapor was added to the feed. Between the ball valves and the reactor is a four-way valve. In dry mode the gas will pass straight through this valve towards the reactor. In wet mode the gas will be diverted through a water vapor bubbler saturator cooled to give a partial pressure of 15 % H_2O. The gas is subsequently led back to the four-way valve and towards the reactor.

The porous powder material was pressed into wafers, mortared and sieved to a particle size of 0.25-0.42 mm. 22-24 mg of sample was placed in the center of a quartz tube reactor (length: 30 cm, inner diameter: 4 mm) and held in place by quartz wool. The exhaust gas is led into a gas chromatograph (Agilent 6890 GC) connected to a mass spectrometer (5979C MDS) using a SPB-5 column (60 m, 3 µm film thickness, 0.53 mm i.d.).

The MS was calibrated for NO and N_2 with different concentrations, and temperature programmed calibration of the experiment gas mixture was also performed both in dry mode and wet mode. GC analysis was performed with an oven temperature of 35 °C.

3.4.X-ray absorption spectroscopy (XAS)

3.4.1. Beamline lay-out

XAS data was performed at the Swiss-Norwegian Beam Lines (SNBL) B-station at the European Synchrotron Radiation Facility (ESRF)[60] in Grenoble, France. ESRF produces an electron beam energy of 6 GeV and maximum current of 200 mA in multi-bunch mode. A schematic illustration of the beamline is shown in Figure 3.4.

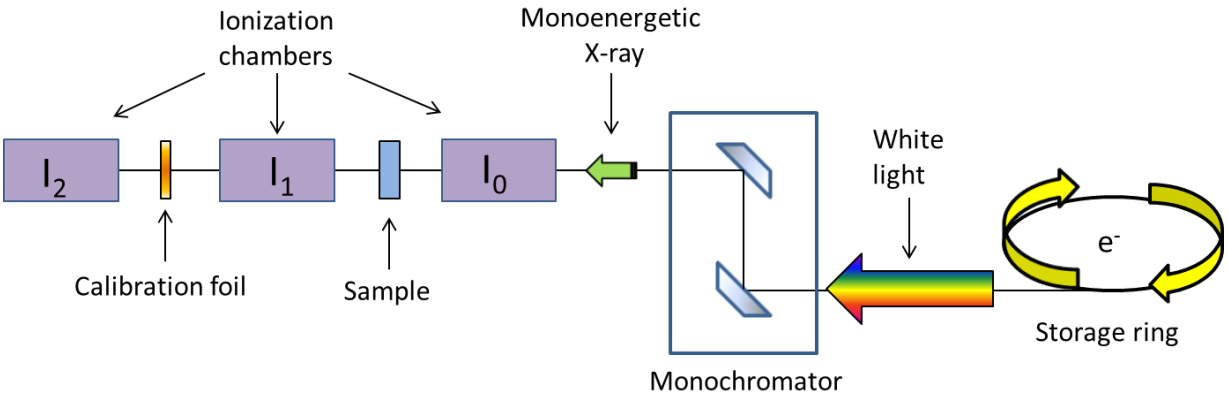

Figure 3.4: Rough schematic of the experimental set-up at BM01-B.

This beamline receives electromagnetic radiation from a bending magnet, but the white light, which consists of frequencies from the microwave region to the high-energetic X-rays, must be fine-tuned before it can be introduced to the sample. SNBL is equipped with a Si(111) channel cut monochromator and a double crystal monochromator which select the X-ray wavelength, by changing the incident angle at which the radiation hits the monochromator. A set of slits and beamstops are also employed both to ensure that the beam spot size is correct and for safety reasons. The spot size for BM01-B is 10 mm horizontally and 0.6 mm vertically. A spectral range of 4-80 keV can be achieved with the monochromator, but for copper samples only the range 8.8-10 keV was measured.[60]

Measurements on the copper k-edge (8979 eV) were performed in transmission mode with ionization chamber detectors. I_0 (17cm long) counts incident photons and I_1 (31cm long) counts the remaining transmitted photons after absorption from the sample. Ionization chamber I_2 measures the transmitted beam after the copper foil which is always exposed simultaneously for calibration purposes. The gas compositions of the ion chambers were 80% N_2 + 20% Ar for I_0 and 75% N_2 + 25% Ar for I_1.

3.4.2. Sample analysis

Ex situ measurements of samples and analysis of model compounds were performed with the sample powder in aluminum sample holders with Kapton® tape on the front and back end to hold the powder in place. Model Cu compounds were diluted with boron nitride to ensure a suitable level of transmittance.

In-situ XAS experiments were performed using an in-situ reaction cell designed by Karina Mathisen and Magnus Rønning as displayed in Figure 3.5.

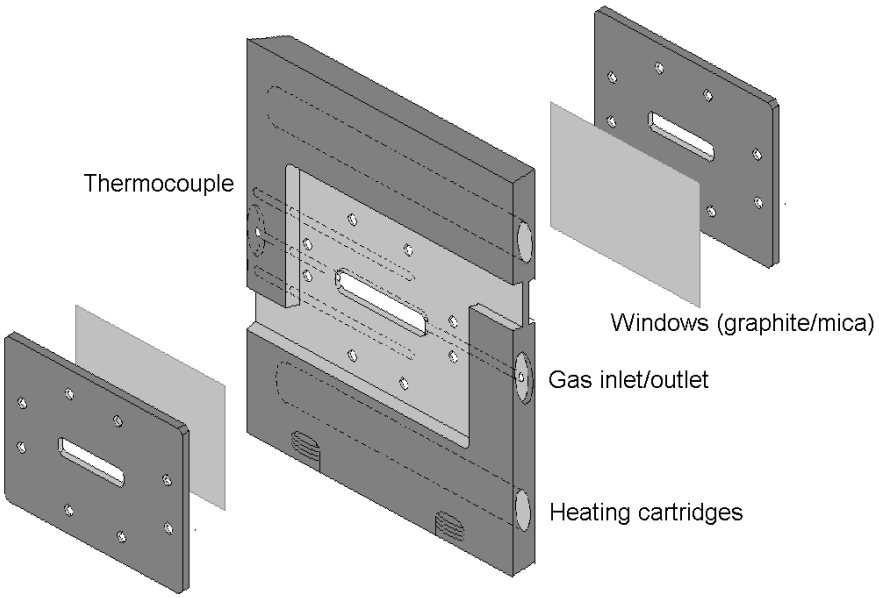

Figure 3.5: In-situ reaction cell for XAS measurements.

The sample powder of was pressed into pellets, ground in a mortar and sieved to a particle size of 0.25-0.42mm to prevent diffusion limitations. 45 mg of sample was loaded in the open cavity of the cell between two pieces of quartz wool to hold it in place. Graphite windows were placed on either side of the cavity to allow beam transmittance. Steel plates were screwed on to hold the windows in place and prevent leakage. The thickness of the cell cavity is 1.5mm, and the cell is made of stainless steel. Gas inlet and outlet lines were attached to the sides of the cell, and connected to mass-flow controllers (MFC) for accurate gas feed composition used for deNO_x measurements. The temperature was controlled by a voltage supplier via two heating cartridges and a thermocouple.

The experimental procedure was replicated from a redox experiment in the work of Kristiansen *et al.*[70] in order to have a means of comparison. After a few measurements at room temperature and open atmosphere conditions the sample H-SAPO34-2 was calcined within the reaction cell in 15 ml/min 20% O_2/80% He. From room temperature the cell was heated to 450 °C at a ramping rate of 10 °C/min, followed by a 20 min dwell period. The cell was subsequently let cool to 350 °C and for the rest of the experiment this temperature was maintained. During the experiment the gas mixture in molar concentrations was as follows: 0.2 % NO and 2 % O_2, or 1.3 % C_3H_6 in alternating fashion. Helium was used as a carrier gas, making up the difference to achieve a weight hourly space velocity (WHSV) of 350 g g_{cat}^{-1} h^{-1}. The vapor bubbler saturator was cooled to give exactly 15% of H_2O in molar concentration. Regardless of feed composition, the total feed volume was constantly 15ml/min. The following experiment consisted of alternating cycles in reducing and oxidizing gas feed (C3H6 and NO/O2, respectively) and also in dry and wet feed as displayed in Table 3.2. At the very end only He was fed with water vapor present.

Table 3.2: Redox experiment divided into alternating cycles. Blue fields indicate wet feed.

Cycle 1		Cycle 2			Cycle 3			Cycle 4	
C_3H_6	NO/O_2	C_3H_6	C_3H_6/H_2O	$NO/O_2/H_2O$	C_3H_6/H_2O	C_3H_6	NO/O_2	C_3H_6	H_2O

All measurements were performed in Quick-XAS mode, in the range of 8800-10000 eV with a 0.5 eV step size and 50 ms counting time. Measurements were being recorded continuously throughout the calcination and experiment. The time required for an entire scan including resetting the monochromator to the initial energy was just above 2 minutes.

3.4.3. Data reduction

The Athena software from IFEFFIT[71] package was used for data reduction. Rebinning was performed with respect to Cu atom absorber, resulting in evenly spaced energy points, and consequently a higher signal-to-noise ratio. In practice closely spaced energy points are averaged to produce one single point. All XAS spectra from Cu samples were calibrated against a metallic Cu foil between ion chambers I_1 and I_2. The Cu K-edge is at 8979 eV. For

XANES analysis the spectra were normalized at 30-150 eV, and from 150 eV to the end of the spectrum for EXAFS analysis. A spline function in Athena was used to subtract the smooth background $\mu_0(E)$ from the normalized data. Deglitching was used sparingly where faults in the monochromator caused glitches. Truncating was performed at the end of the spectra where low signal-to-noise ratios dominated. Care was taken to only truncate as much as strictly necessary in order to retain good resolution in EXAFS analysis.

3.4.4. XANES region

The XANES region is used to extract information about valence state of copper and also about local site symmetry surrounding it. There are several methods to achieve that, however in this context the most useful information which can be retrieved is to which extent the divalent Cu species are reduced to monovalent species in a reducing atmosphere, and if the process is reversible in an oxidizing atmosphere. The position of the edge and shape of the edge region was therefore compared to those of model compounds which are displayed in Figure 3.6. These compounds can be considered extremes, and in the synthesized samples there will often be composite shapes and positions due to the signal being an average of all Cu atoms within the spot size of the X-ray beam.

The absorption edge E_0 was placed at the inflection point of the jump ($\Delta\mu_0$), which is as the first peak in the 1. derivative spectrum of Cu foil. However, with the presence of pre-edge or shoulders masking first inflection point the E_0 would simply be placed as close half height of the jump as possible, without being placed on the pre-edge/shoulder. The energy correction, i.e. difference between known and measured E_0 was transferred to the sample. The absorption energy E_0 was placed for a large array of measurements from the experiment and compared to the model compounds. The practice of this is shown in Figure 3.6 where the black targets indicate the E_0 position on the normalized XANES and the 1. derivative.

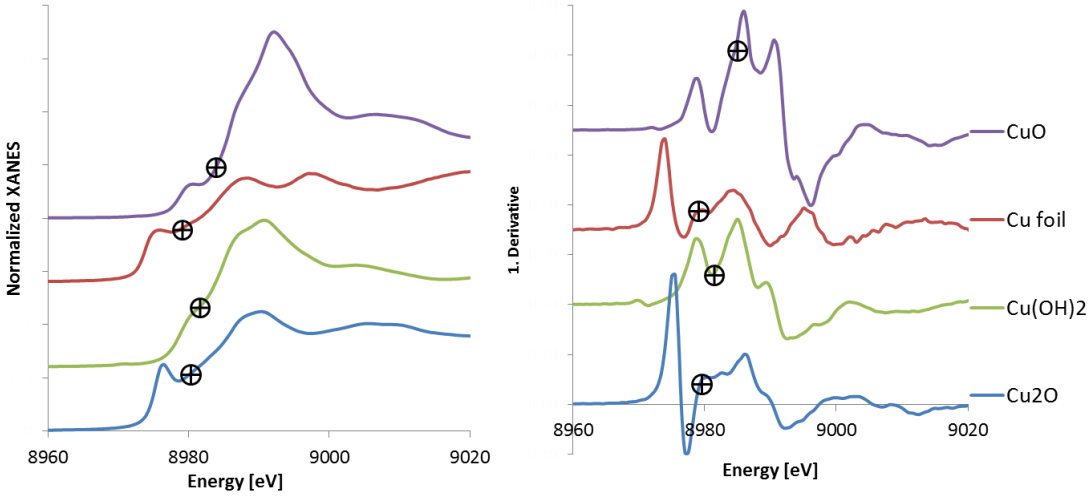

Figure 3.6: Normalized XANES and 1. derivative around the absorption edge. The targets mark the position of the absorption energy for model compounds.

In addition to recording the position of E_0, the position and height of the pre-edge feature, where visible on the normalized XANES, was taken note of.

3.4.5. EXAFS analysis

For the EXAFS analysis the program DL EXCURV was employed. The program calculated the *ab initio* phaseshifts and backscattering amplitude by defining the atoms present in the sample. Least-squares refinements of the theoretical $\chi(k)$ to the experimental $\chi(k)$ was performed using the curved wave theory[56]. A k^3-weighting was used for all samples, and a k-range of 2-13. EXAFS analysis of the models were carried with fixed multiplicities, while shell distances, Debye-Waller factors $2\sigma^2$, and E_F was refined. Once the parameters remained unchanged during refinements, the amplitude reduction factor (AFAC) was refined and transferred to the samples with similar oxidation state by comparison with the XANES. For most measurements only the nearest shell of neighbors was fitted. For samples, refinements executed for individual parameters, *i.e.* multiplicities N, shell distances R, Debye-Waller factors $2\sigma^2$, and the energy correction to E_0, E_F. The reduced chi-squared (χ^2) was calculated for EXCURV98 based on the number of data points, weighting and defined free parameters. When refining a single shell the number of free parameters is 4, and for two shells it is 7. A second shell was only added to a few measurements, when needed.

Fourier filtering was performed to investigate the third shell contributing element. This involved isolating the shell contribution in R-space in the range 2.5-3.5. This contribution was then back-transformed into k-space and refined with the most probable back-scatterer. The best quality of fit indicated the most probable back-scattering element.

4. Results

4.1.X-ray diffraction (XRD)

4.1.1 Conventional SAPO-34

The X-ray diffractograms of four calcined SAPO-34 samples are displayed in Figure 4.1 in the range 5-50°. With the exception of two extra peaks on SAPO34-2 (20° and 22°) all peaks cohere with the chabazite pattern, with high signal-to-noise ratio, showing that the samples are phasepure. The extra peaks, denoted in the figure with stars, could just be impurities, or might come from a different SAPO phase.

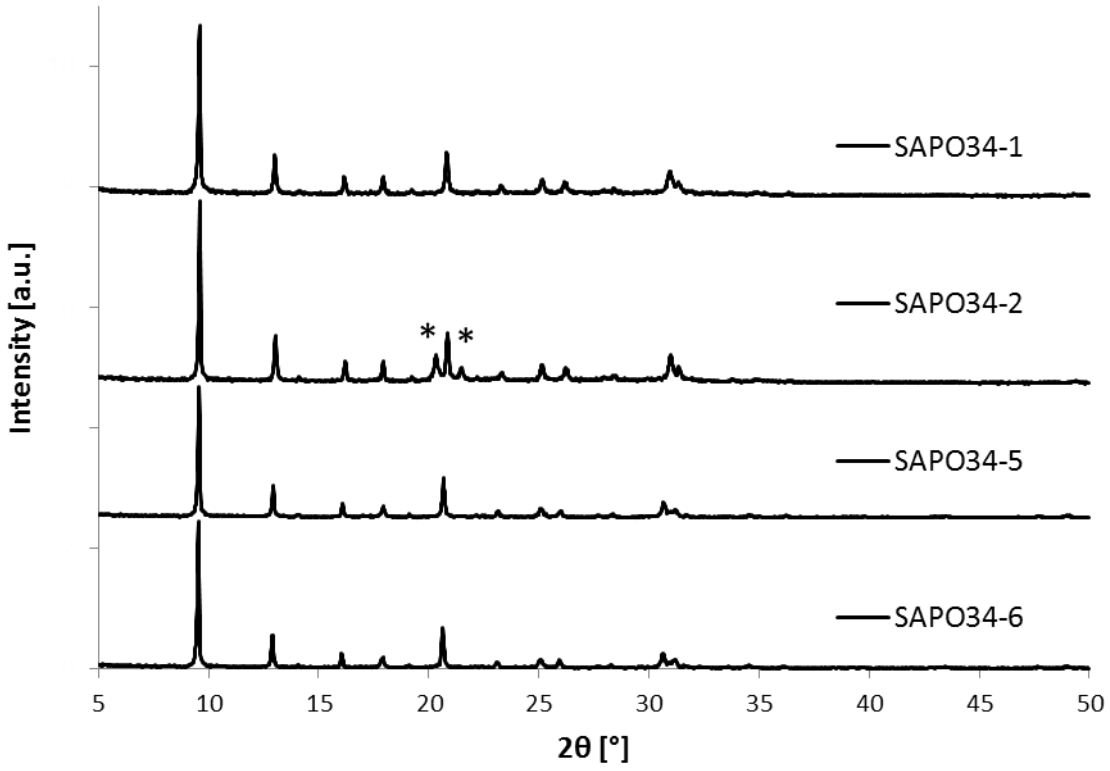

Figure 4.1: Powder diffraction patterns of calcined conventional samples SAPO34-(1, 2, 5 and 6).

4.1.2. Hierarchical SAPO-34

Three diffractograms of calcined hierarchical samples are displayed in Figure 4.2. No substantial extra peaks are observed, and none are missing, and therefore these samples all qualify to be deemed phasepure. This technique is not able to provide additional information on the pore system, other than the 0.38 nm pores inherent to the chabazite topology which is identified in these three samples. Additional characterization is required to determine other structural differences in the material. There is some difference in peak height, which can generally be attributed to actual degree of crystallinity. However different sample holders with different sample cavities have been used and a direct comparison is therefore not applicable.

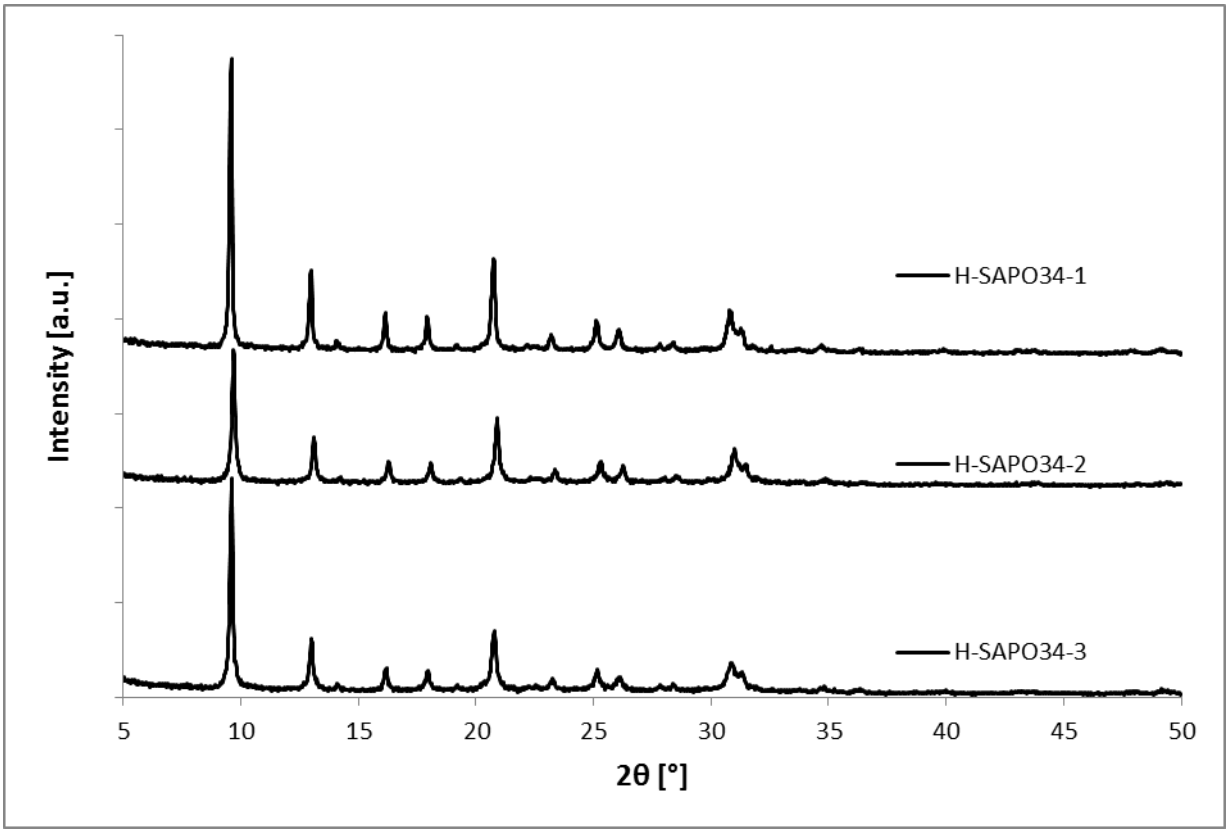

Figure 4.2: Powder diffraction patterns of the hierarchical samples H-SAPO34-(1-3) after calcining.

4.1.3. Ion-exchanged conventional and hierarchical CuSAPO-34

Figure 4.3 shows X-ray diffractograms of the conventional SAPO34-3 and SAPO34-4 and samples after ion exchange with $[Cu(NH_3)_4]^{2+}$ (0.015 M) and $Cu(NO_3)_2$ (0.03 M), respectively. The diffractograms show structure collapse, recognized by the low signal-to-noise ratio and absence of characteristic peaks. Structure collapse following ion-exchange procedures has not previously been reported in the literature. The same collapse occurred in conventional SAPO34-1 and SAPO34-2.

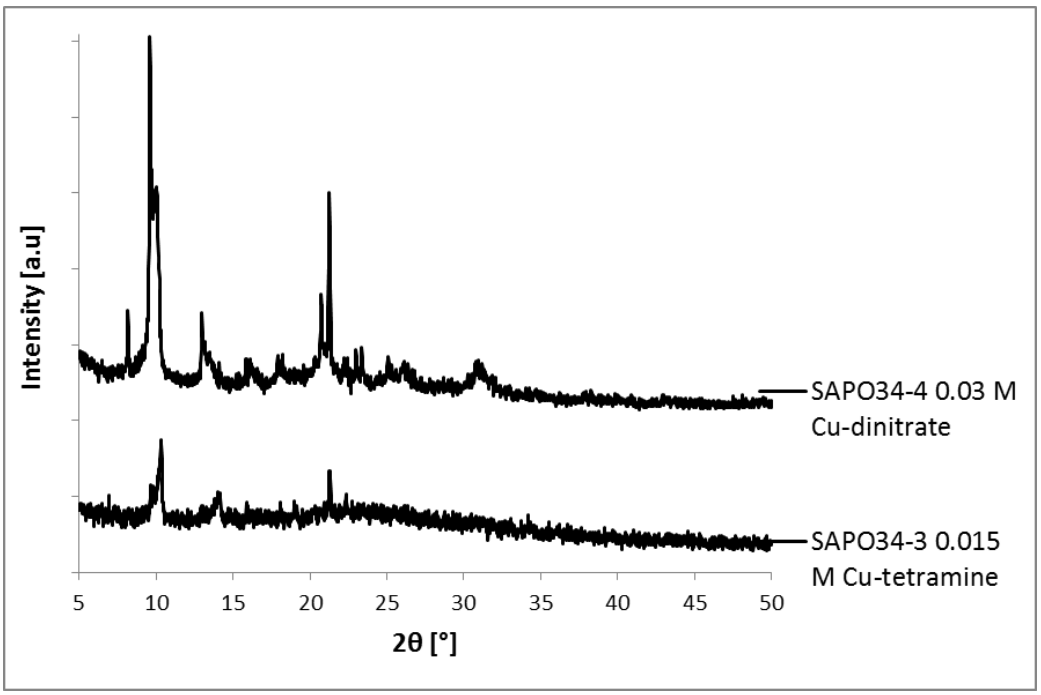

Figure 4.3: Examples of powder diffraction patterns where the crystalline structure has become amorphous during ion-exchange. Si:Al ratios were 0.2 for these samples.

Eventually, it was found that conventional SAPO34-5 and SAPO34-6 were able to withstand being ion-exchanged with lower copper concentrations (0.015 M), with a reasonable uptake of copper. The same synthesis procedure had been used for these samples as for conventional SAPO34-(1-4), but with much higher Si : Al ratios, 0.3 instead of 0.2. The difference between 72 and 96 hours crystallization time is apparently negligible, but the increased Si content has added sturdiness to the material.

After further work had been performed on SAPO34-5 ion-exchanged with 0.015 M tetramine copper(II), an attempt was also made at ion-exchanging the sample with 0.03 M solution (bottom diffractogram). The results, among others are displayed in Figure 4.4, and shows that the aforementioned sample had lost much more crystallinity than the one exchanged at 0.015 M. Conventional SAPO34-5 was chosen for comparison, and only this sample among the conventional samples was performed further experiments on.

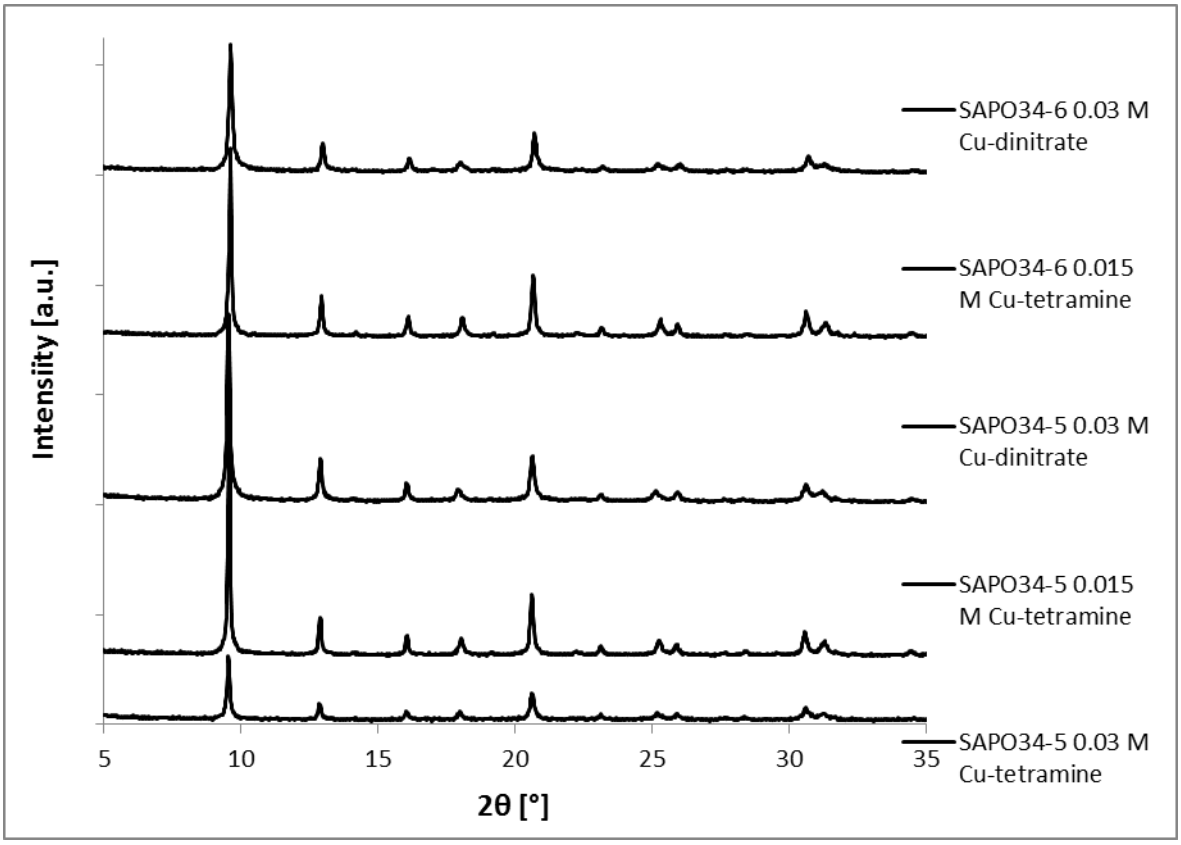

Figure 4.4: Examples of powder diffraction patterns where samples have retained their crystallinity during ion-exchange. Si:Al ratio was 0.3 for these samples.

The hierarchical samples all retained their crystallinity through an ion-exchange with 0.03 M Cu-tetramine, displaying more stability in the conditions in question than the conventional samples. Hierarchical H-SAPO34-2 was chosen among the hierarchical samples for further experiments, on account of the yield of material from the synthesis.

4.1.4. Incorporated CuSAPO-34

Figure 4.5 show diffractograms for copper-incorporated conventional SAPO-34 Incorp-1 and incorp-2. The diffractograms of the incorporated CuSAPO-34 samples show phasepure materials, but only the highest peak gives substantial intensity, while the others are quite low.

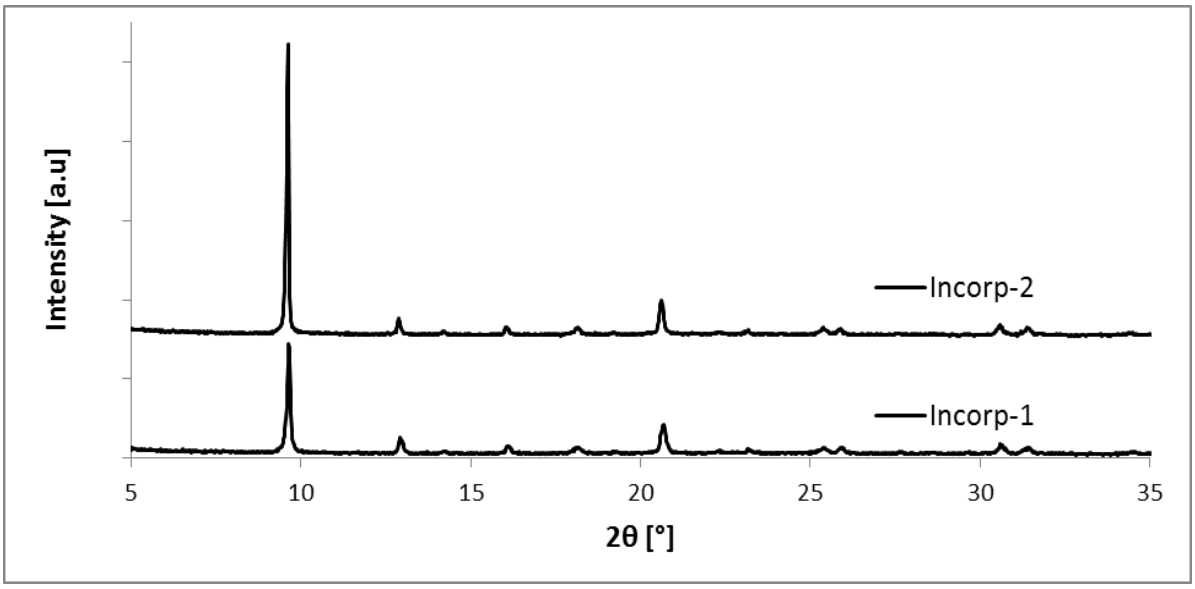

Figure 4.5: Powder diffraction pattern of calcined incorporated CuSAPO-34 (Incorp-1 and -2)

Because of the higher crystallinity, the incorporated CuSAPO-34 sample, Incorp-2, was chosen for further experiments.

4.1.5 Synthesis summary

A summary of all syntheses including ion-exchanges performed is assembled in Table 4.1. The point of this is to make clarifications on the reasons for synthesizing several compounds, and the selection of samples for further investigations. As the table shows all syntheses displayed good crystallinity after calcination, but only a few maintained crystallinity during ion-exchange with tetramine copper(II). The ones which did survive dinitrate copper(II) exchange only took up very small amounts of Cu in the structure, observed visually through the intensity of the blue color.

Table 4.1: All syntheses and ion-exchange procedures are summarized. Green checkmarks indicate phasepurity, while red crosses indicate collapse of crystalline structure. Low uptake of copper was observed visually by the intensity of the blue color.

Type	Sample	Crystallization time [hours]	After calcination	After ion-exchange w/ $Cu(NO_3)_2$	Cu conc. [mol/L]	After ion-exchange w/ $[Cu(NH_3)_4]^{2+}$	Cu conc. [mol/L]
Conventional	SAPO34-1	96	√	X	0.03	X	0.03
Conventional	SAPO34-2	192	√	X	0.03	X	0.03
Conventional	SAPO34-3	48	√	√ *	0.03	X	0.03
Conventional	SAPO34-4	48	No data	X	0.03	X	0.03
Conventional	SAPO34-5	72	√	√ *	0.03	√	0.015
Conventional	SAPO34-5	72	√	-	-	√	0.03
Conventional	SAPO34-6	96	√	√ *	0.03	√	0.015
Hierarchical	H-SAPO34-1	72	√	√ *	0.03	√	0.03
Hierarchical	H-SAPO34-2	72	√	No data	0.03	√	0.03
Hierarchical	H-SAPO34-2	72	√	-	-	X	0.015
Hierarchical	H-SAPO34-3	72	√	√ *	0.03	√	0.03
Incorporated	Incorp-1	168	√	Not performed	-	Not performed	-
Incorporated	Incorp-2	168	√	Not performed	-	Not performed	-

* = Very low uptake of Cu X = Not Phasepure √ = Phasepure

4.2.ICP-MS

The main objective of ICP-MS analysis in this context is to determine the Cu loading in the SAPO-34 samples. This has been essential for the selection of samples for further analysis. As Table 4.2 shows that the samples ion-exchanged with $Cu(NO_3)_2$ exhibited a very low uptake of copper. This was in accordance with the color of the samples, which showed only a faint hue of blue, in contrast to the samples ion-exchanged with $Cu(NH_3)_4^{2+}$ which had a stronger color, and the incorporated SAPO-34 samples which were bluer still.

These results led to the exclusion of $Cu(NO_3)_2$ samples from further analyses as it was important that the copper content was high enough for catalytic measurements and XAS-experiments. Thus the candidates for the thesis were chosen to be SAPO-34-5 and H-SAPO-34-2 ion-exchanged with copper tetramine and Incorp-2. The ion-exchanged samples SAPO34-5 and H-SAPO34-2 will from this point be called Cu-SAPO34-5, and Cu-H-SAPO34-2, while the corresponding samples without copper will retain their initial names, SAPO34-5 and H-SAPO34-2.

Table 4.2: Weight percent compositions of Cu-containing samples.

		[wt%]			
Sample name	Cu(II) precursor	**Al**	**Si**	**P**	**Cu**
SAPO-34-5	$Cu(NH_3)_4^{2+}$	17.9	5.2	15.2	1.4
SAPO-34-5	$Cu(NO_3)_2$	17.6	4.9	15.3	0.5
H-SAPO-34-2	$Cu(NH_3)_4^{2+}$	16.1	5.7	14.3	3.9
H-SAPO-34-2	$Cu(NO_3)_2$	18.1	5.6	16.1	0.6
Incorp-2	Cu-TEPA	20.7	6.0	12.1	6.8

4.3.TGA-DSC

Figure 4.6 shows weight loss and thermal events from TGA-DSC measurements during heating in synthetic air to 650 °C of the as-synthesized samples conventional SAPO34-5 and hierarchical H-SAPO34-2 without copper. There are two main mass events present, the first, at 50-100 °C, is predominately water desorption shown as a ~2% weight loss and as endothermal events by DSC. The second event is attributed to the tetraethyl ammonium template combustion at 350-470 °C detected by the MS as NH_3 and CO_2.

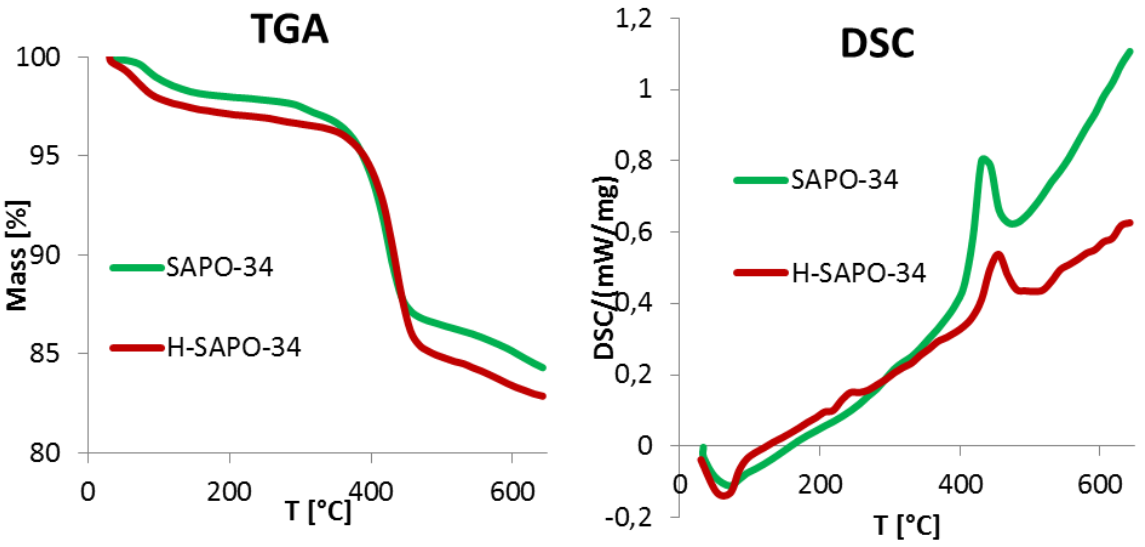

Figure 4.6: Weight loss (left) and corresponding thermal events (right) during heating in synthetic air of the as-synthesized SAPO34-5 and H-SAPO34-2.

The expectation was that a substantial difference would be seen between the conventional and hierarchical samples, with mass losses occurring at lower temperatures in the hierarchical sample than for the conventional. The actual results are much more similar than was expected. The initial water desorption was a bit higher in magnitude for hierarchical than for conventional, and slightly more template was lost. Totally, the mass loss during TGA was 15.7 wt% (conv.) and 17.1 wt% (hier.), respectively. According to Cui *et al.*[45] mass loss increases with increasing mesopore volume, but the hierarchical SAPO-34 samples investigated in that work range from 22 to 31 wt%, while the conventional lost 14 wt%. Considering the degree of mass loss in the samples investigated here, one can argue one of

two: 1. The hierarchical sample has a presence of mesopores, or 2. The difference in mass loss is too small to call the sample hierarchical.

There is a possibility that the ramping rate (5°/min) of the experiment was excessively high, and that a lower rate would render possible a more discernable difference.

Figure 4.7 shows weight loss and thermal events from TGA-DSC measurements of the conventional SAPO-34 incorporated with copper, Incorp-2. Incorp-2 underwent a higher mass loss than the copper-free SAPO-34 samples weight (22.8 wt%) from 25-500 C. DSC shows that the weight loss below 200 °C is endothermic, while the weight loss in the range 200-500 C are exothermal events. The drastic slope on the TGA curve around 350-400 °C corresponds to an exothermal event.

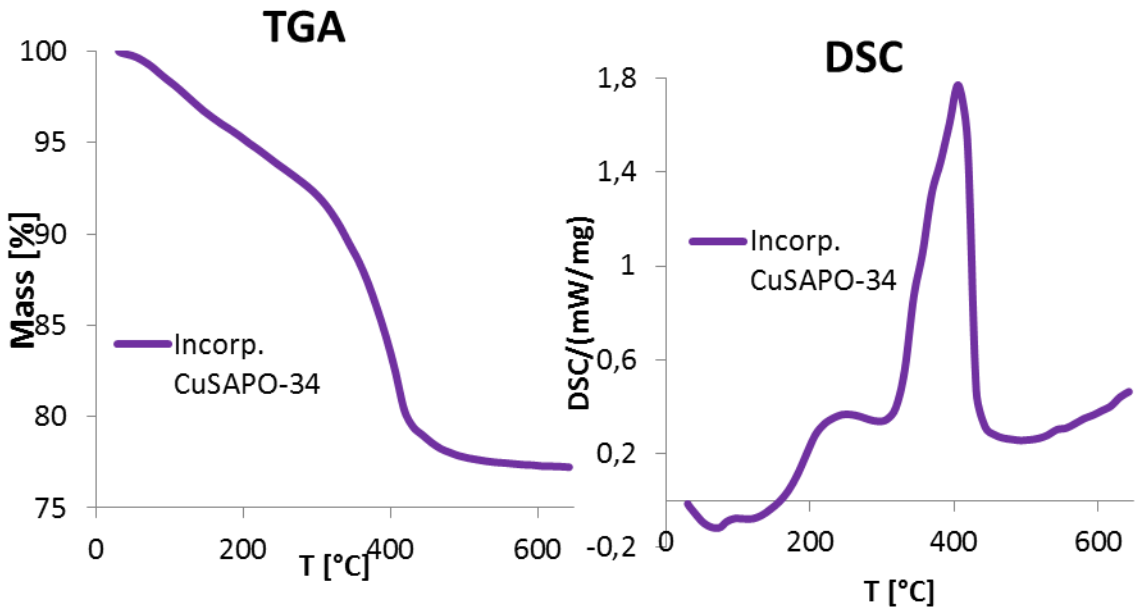

Figure 4.7: Weight loss (left) and corresponding thermal events (right) during heating in synthetic air of the as-synthesized of the as-synthesized sample Incorp-2.

4.4. N_2 adsorption-desorption (BET)

4.4.1. Specific surface area

Table 4.3 lists the specific surface areas of calcined conventional, hierarchical and incorporated Conventional SAPO-34 samples, as well as one ion-exchanged hierarchical SAPO-34. Where not specified, the samples do not contain copper.

Table 4.3: The specific surface areas of several phasepure SAPO-34 samples are listed. The standard deviation for these measurements can be up to 16 m^2/g.

SAPO-34	Sample name	Specific Surface Area [m^2/g]
Conventional	SAPO34-1	**544**
Conventional	SAPO34-2	**527**
Conventional	SAPO34-5	**553**
Hierarchical	H-SAPO34-1	**500**
Hierarchical	H-SAPO34-2	**571**
Hierarchical	H-SAPO34-3	**463**
Hierarchical + ion-exchange	H-SAPO34-3 ion-ex. w/ 0,03M $[Cu(NH_3)_4]^{2+}$	**221**
Incorporated conventional	Incorp-2 (6.8 wt% Cu)	**341**

The specific surface (SSA) is slightly higher for the conventional samples than for the hierarchical (541 and 511 m^2/g, respectively), but the span in SSA is much bigger between the hierarchical samples, so the difference cannot be considered as significant. These differences are quite unexpected as all the hierarchical samples were synthesized at identical conditions without variation in parameters, while the conventional samples had different parameters

(crystallization time and Al/Si ratio). This might be an indicator that the degree of mesoporosity is susceptible to even small variations, and quite difficult to control. This is partly based on the similarity in microporosity between SAPO34-5 and H-SAPO34-2.

The surface areas are similar to what has been reported in the literature; the numbers for both conventional and hierarchical range from 450 to 650 m^2/g. Regarding difference in surface area between conventional and hierarchical SAPO-34 it has been reported both that hierarchical has lower surface area[45] and that there is no discernable difference.[2, 3]

The ion-exchanged H-SAPO34-3 displayed a drastic decline in surface area during ion-exchange even though the XRD patterns show phasepure SAPO-34.

Figure 4.8 shows BET surface area, t-plot micropore area and external surface area of samples SAPO34-5, H-SAPO34-2 and Incorp-2. The majority of the specific surface area for both conventional and hierarchical samples is in the form of micropores, and that the amount of micropore area is very similar for the two. A larger external surface area for the hierarchical sample is in line with the presence of mesopores and macropores.

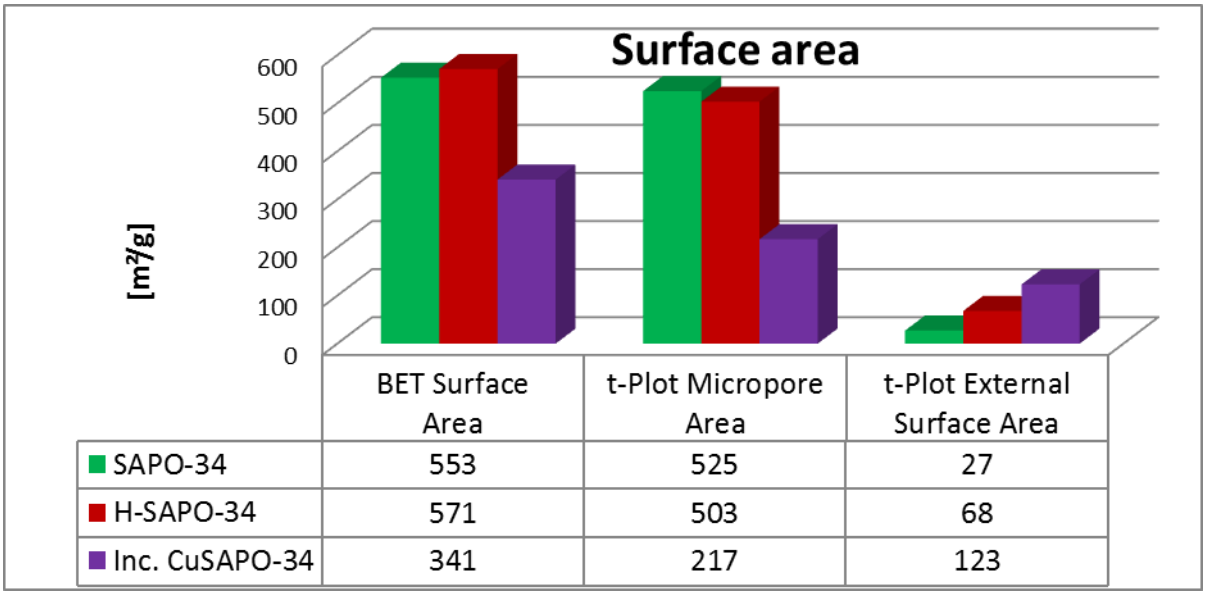

	BET Surface Area	t-Plot Micropore Area	t-Plot External Surface Area
SAPO-34	553	525	27
H-SAPO-34	571	503	68
Inc. CuSAPO-34	341	217	123

Figure 4.8: BET surface area, t-plot micropore area and external surface area of samples SAPO34-5, H-SAPO34-2 (without copper) and copper containing Incorp-2.

4.4.2. Hysteresis

The N_2 adsorption-desorption isotherms of calcined samples SAPO34-5 and H-SAPO34-2 are shown in Figure 4.9. The conventional SAPO-34 displays almost no hysteresis at all, as would be expected from a purely microporous material. The small difference at P/P_0=0.8-0.9 might be explained by interstitial cavities between the particles. In the hierarchical sample a clearer hysteresis can be observed at P/P_0=0.6-0.8, and also in the steep section approaching P/P_0=1. Since the hysteresis loop exhibited by H-SAPO34-2 is two-fold in the sense that there is one closure in the steep section and one in the more horizontal section, it is difficult to explain it with just one category of hysteresis as explained in section 2.5.2. Up to the point of P/P_0=0.85 the isotherms most resemble a H4 category loop, while between relative pressures 0.85 and 1 it looks more like an H1 category loop, as explained by IUPAC [34]. It should be noted that these two categories are extremes to each their end of the scale, while H2 and H3 are considered as intermediates, however, due to the two-fold nature of this hysteresis, a combination might be more suitable. The H1 loop is often attributed to porous materials in agglomerated state, while H4 can be a sign of slit-like pores.

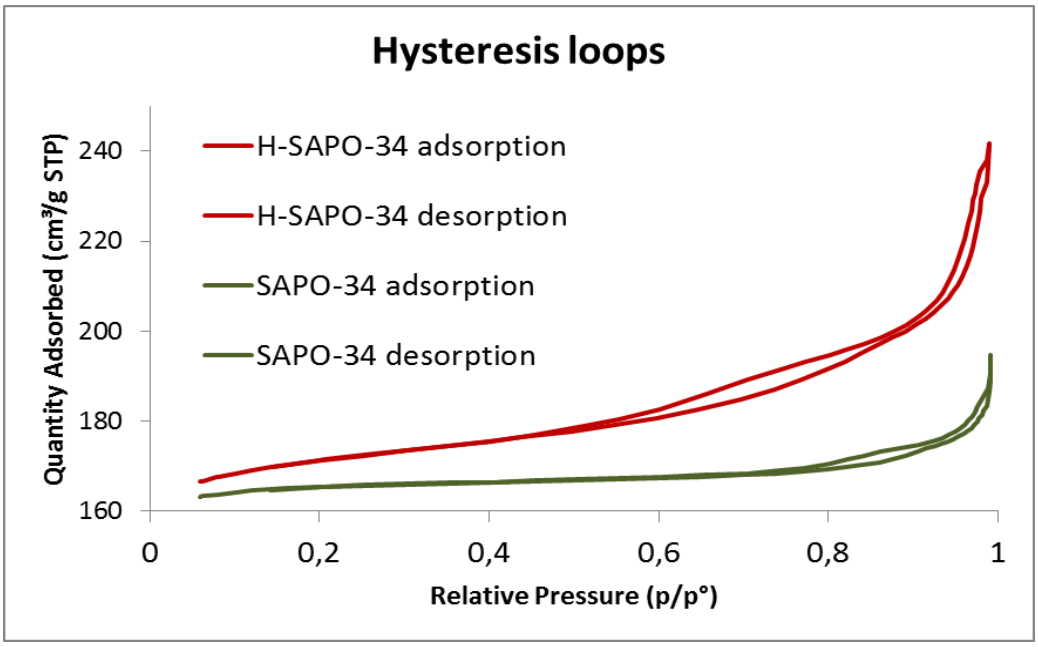

Figure 4.9: The hysteresis loops of conventional and hierarchical SAPO-34 (SAPO34-5 and H-SAPO34-2, respectively) after calcination, without any metal present.

The hysteresis for H-SAPO34-2 is much less pronounced than reported by Yang *et al.* [2] from which the synthesis parameters are extracted.

Figure 4.10 shows results from N_2-physisorption measurements of incorporated CuSAPO-34 (Incorp-2), which shows a significant hysteresis loop, similar to the H3-type. This is indicative of plate-like particles, giving rise to slit-shaped pores. The low adsorption values at relative pressures are linked to a small degree of microporosity. The hysteresis was not reported by Martínez-Franco *et al.*[54] and is quite surprising. Only a slightly higher micropore volume was reported than what was found here (0.14 and 0.10 cm^3/g, respectively).

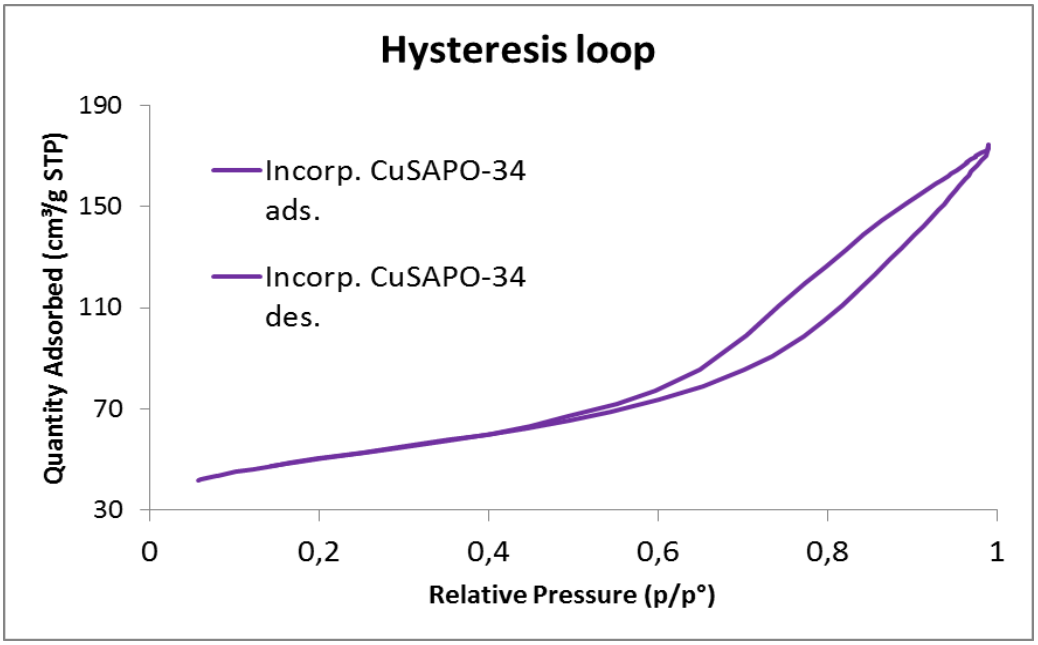

Figure 4.10: The hysteresis loop of Incorporated CuSAPO-34 (Incorp-2) after calcination.

4.4.3. Pore size distribution

The pore size distribution of samples SAPO-34-5 and H-SAPO34-2 as calculated from the BJH method is displayed in Figure 4.11 and Figure 4.12 in the ranges 2-100 nm and 2-20 nm, respectively. The wide distribution spectrum shows that these measurements were not able to discern any narrow peaks in the samples at pore diameters larger than 20 nm. Yang *et al.*[2] reported macropores present around the size of 6 μm, but such results would not be obtainable with N_2-physisorption measurements.

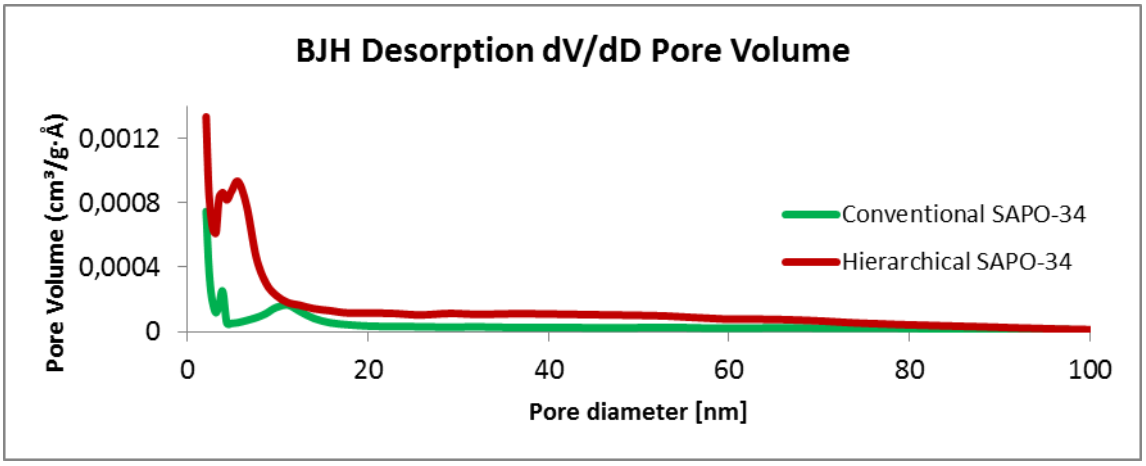

Figure 4.11: Pore size distribution of samples SAPO34-5 and H-SAPO34-2, in the range of 2-100 nm.

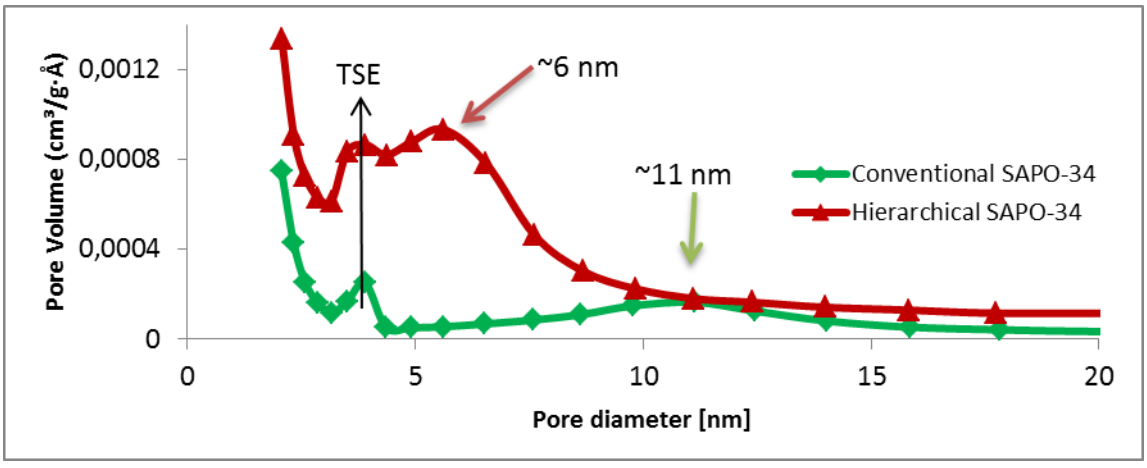

Figure 4.12: Pore size distributions of SAPO34-5 and H-SAPO34-2 in the range of 2-20 nm.

The narrower spectrum is quite informative about the porous nature of the two materials. They both display the phenomenon of tensile strength effect (TSE)[35] around 4 nm, which is a false contribution explained in 2.5.2. A large, contribution around 6 nm on the hierarchical sample can, however, be attributed to real mesopores. It is quite wide, and the tail of the peak

stretches to 10 nm. The conventional sample displays a small, broad peak around 11 nm. It is very probable that this is due to interstitial cavities between particles.

The pore size distribution of incorporated CuSAPO-34 (Incorp-2) is displayed in Figure 4.13 and Figure 4.14. No contributions are observed between 20 and 100 nm. Tensile strength effect is also here present and considered to be false. A large, broad peak around 7 nm is interpreted as real, but quite unexpected. In the same fashion as the hysteresis loop, this mesopore peak has not been reported in the paper where the synthesis procedures are retrieved.[54] The tail of the peak stretches to 20 nm, not dissimilar to hierarchical SAPO-34.

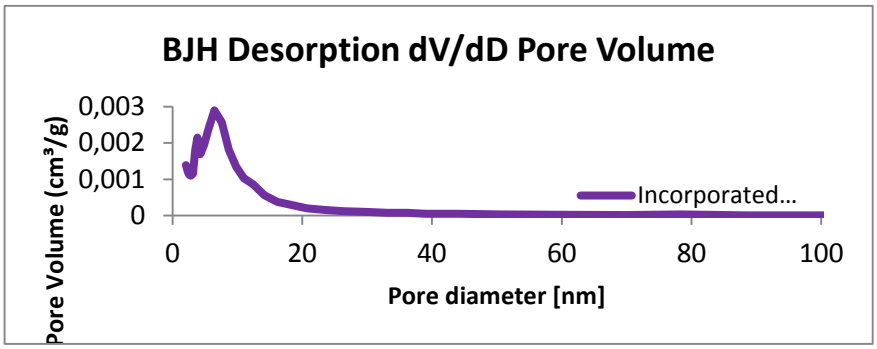

Figure 4.13: Pore size distribution of sample Incorp-2 in the range of 2-100 nm.

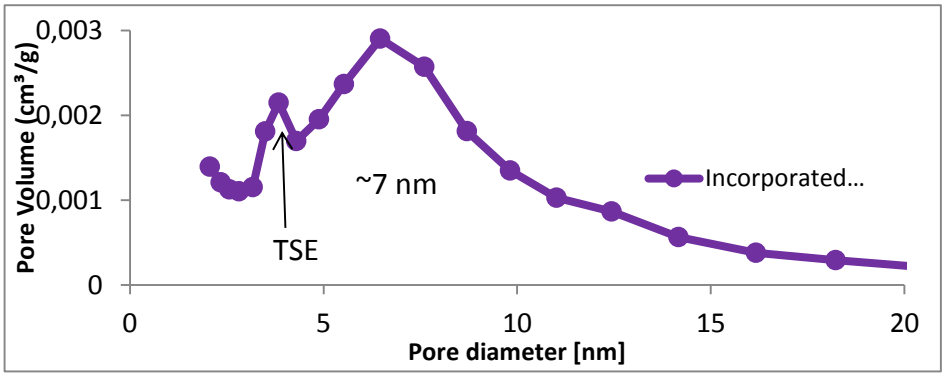

Figure 4.14: Pore size distribution of sample Incorp-2 in the range of 2-20 nm.

4.5 Coke deposition

Elemental CHN analysis of the samples after coke deposition was performed. The results are shown in Figure 4.15.

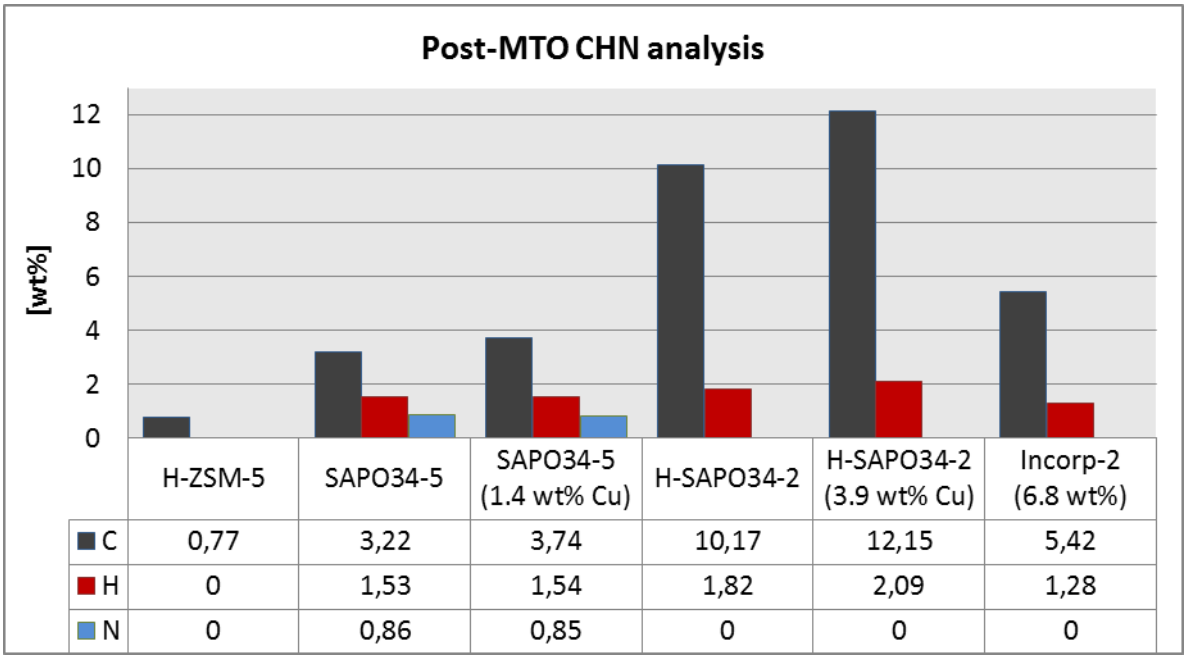

	H-ZSM-5	SAPO34-5	SAPO34-5 (1.4 wt% Cu)	H-SAPO34-2	H-SAPO34-2 (3.9 wt% Cu)	Incorp-2 (6.8 wt%)
C	0,77	3,22	3,74	10,17	12,15	5,42
H	0	1,53	1,54	1,82	2,09	1,28
N	0	0,86	0,85	0	0	0

Figure 4.15: CHN analysis of all samples after undergoing coke deposition.

Two main conclusions can be drawn from this chart:

The first is that the pore system strongly affects coke deposition. Both hierarchical samples accumulate much more coke than the conventional samples. Since conventional SAPO-34 almost only possesses internal surface area (according to BET measurements), all carbon deposited must be on the inside of the micropores. Figure 4.8 also states that both conventional and hierarchical SAPO-34 contain very similar amounts of micropore area/volume, and therefore it is likely that excess coke on hierarchical samples are present in the mesopores. Incorp-2, which should not, but might, possess mesoporosity, is somewhere in between the conventional and hierarchical.

The second conclusion is that copper amount has some effect on coke deposition, but not in the same order of magnitude as the nature of the pore system. There is no linear relationship through the three samples of widely different Cu amounts, however both ion-exchanged samples have incurred a slight increase in coke amount.

The N_2-physisorption (Figure 4.16) curves corroborate the notion that all micropore volume is filled with carbonaceous material after coke deposition.

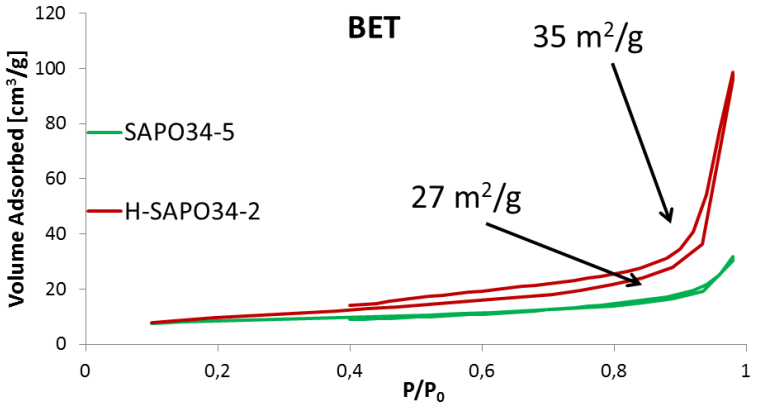

Figure 4.16: N_2-adsorption-desorption isotherms of conventional and hierarchical SAPO-34 without copper after coke deposition. BET surface areas of the individual curves are displayed at the arrow ends.

The specific surface areas have fallen from 553 m^2/g (conv.) and 571 m^2/g (hier.) to 27 m^2/g and 35 m^2/g, respectively. The conventional SAPO-34 displays absolutely no sign of mesopore presence, and the remaining surface is exactly equal to the t-plot external surface area measured for the same sample without coke (27 m^2/g), displayed in Figure 4.8.

Hierarchical SAPO-34 does not show the same degree of exactitude, but after coke deposition a clear hysteresis is visible between the adsorption and desorption curves. This, clearly points to mesopores being present in the sample.

After TPD had been performed on three samples, another round of elemental analysis was performed. The results (yellow borderline) are listed in Figure 4.17, and compared with the results obtained after coke deposition (green borderline). The most interesting feature with these results is that hierarchical SAPO-34 has lost a great deal of carbon (7.2 wt%) while conventional SAPO-34 has lost almost no carbon at all (0.2 wt%). It must also be taken into account the fact that the amount of residual carbon after TPD is very similar between conventional and hierarchical SAPO-34, 2.98 wt% and 2.94 wt%, respectively. Both these features, combined with similar micropore areas, lead towards the conclusion that conventional SAPO-34 contains coke only in the micropores, and the excess coke beyond this amount on hierarchical samples is positioned in the mesopores.

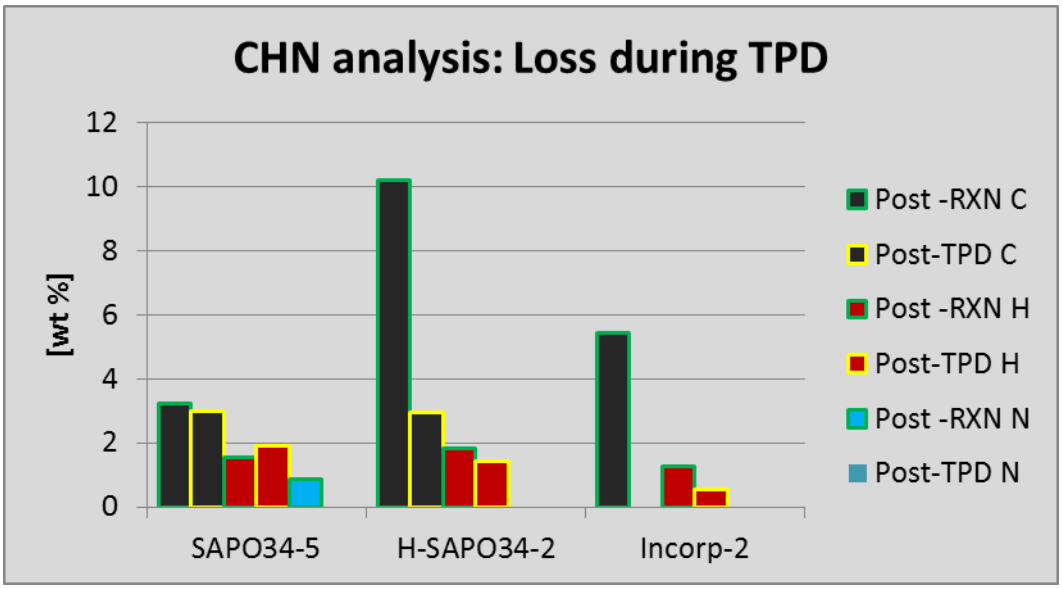

Figure 4.17: CHN analysis of conventional, hierarchical and incorporated SAPO-34 after TPD procedure. They are compared to the post-reaction results displayed earlier.

One of the samples seems to have gained hydrogen during the TPD reaching 1000 °C. This can be attributed to the hydrophilic nature of the zeotype in question, and it is very likely that the compound would have attracted water from air after the TPD measurement. TPO measurements of SAPO-34 samples which had not undergone coke deposition (Appendix C) showed large loss of mass around 100 °C, and this is no doubt water present in the pores. The carbon is used as the main measure of coke content, although hydrogen amount can be used as supplementary information to identify the deposited carbonaceous species.

4.6. SCR-HC-deNO$_X$

Figure 4.18 shows the conversion of NO over conventional and hierarchical ion-exchanged and conventional incorporated SAPO-34 (Incorp-2). The copper loadings were 1.4, 3.9 and 6.8 wt%, respectively. The experiment was performed in both dry and wet feed (15% H_2O). For all temperatures the order in terms of highest to lowest was: incorporated Cu-SAPO-34 > hierarchical Cu-H-SAPO-34 > conventional Cu-SAPO-34. In dry feed the incorporated and hierarchical Cu-H-SAPO-34 reached a maximum at 450 °C, while conventional Cu-SAPO-34 was still increasing. In wet feed the point of maximum conversion seems to be shifted towards higher temperatures. The water feed has not, however had a negative effect on conversion. At 350°C the incorporated SAPO-34 actually exhibits higher conversion in wet feed than in dry, and at 400°C all samples show improved conversion in wet feed.

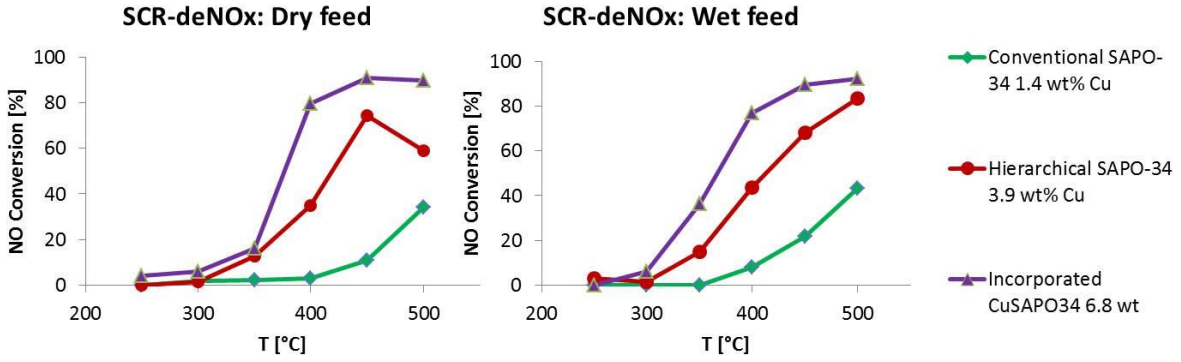

Figure 4.18: Temperature programmed selective catalytic reduction in dry feed (left) and wet feed (right).

Due to problems with the calibration of the mass spectrometer, reliable N_2 selectivities could not be calculated. The MS intensities for N_2 do, however, follow the same patterns as the NO conversion, *i.e.* a fall in NO intensity corresponds to a proportional rise in N_2 intensity. The MS intensities are shown in Appendix D.

4.7.X-ray absorption spectroscopy (XAS)

4.7.1. XANES

XANES spectra from selected sections of the redox experiment performed on Cu-H-SAPO-34 (3.9 wt%) are shown in Figure 4.19. The pre-edge feature rises when the divalent copper is reduced to Cu(I). The shape of the XANES does not differ much between dry and wet feed, indicating that the copper species are stable on the SAPO-34 support in the presence of water at 350 °C. The reversible alternation between the redox pair Cu(I)/Cu(II) also appears to be successful.

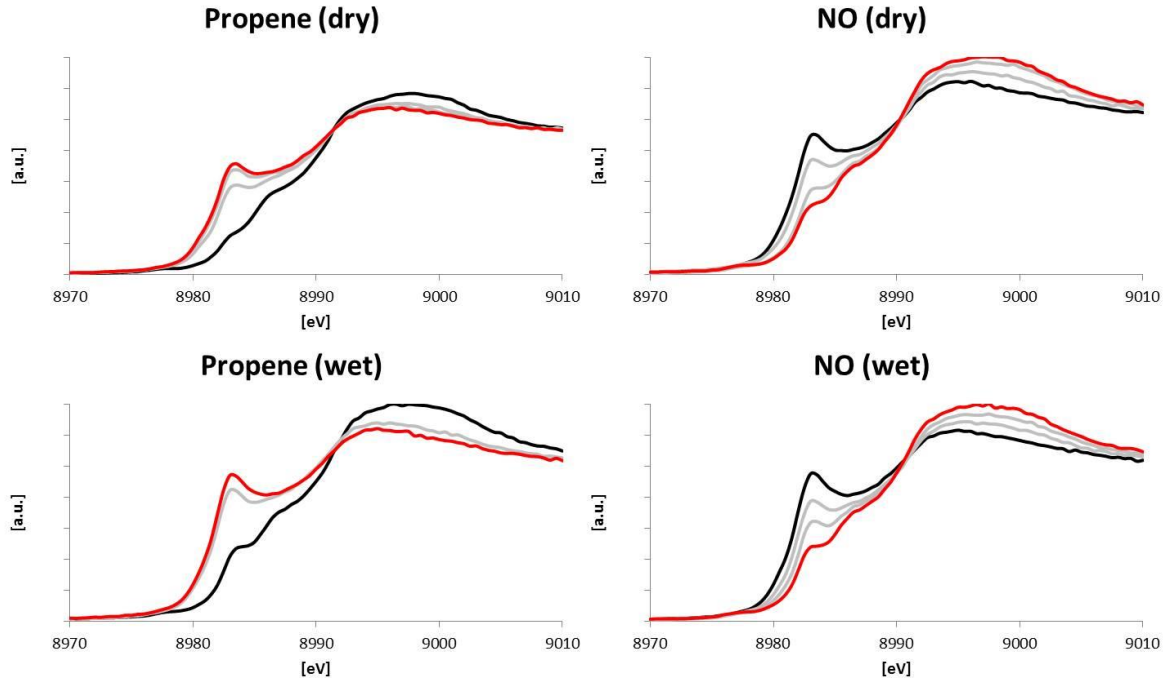

Figure 4.19: XANES spectra showing reduction of Cu(II) by propene (left) and oxidation of Cu(I) by NO (right) in dry feed (top) and wet feed (bottom). Initial spectra are black and final spectra are red.

The absorption energies of selected XANES spectra from each cycle of the *in-situ* redox experiment are presented in Figure 4.20. As described in section 2.4, the positioning of E_0 is not straight forward due to the pre-edge feature which arises for monovalent copper. The feature is normally higher than half height of the jump, and obscures the true value of E_0.

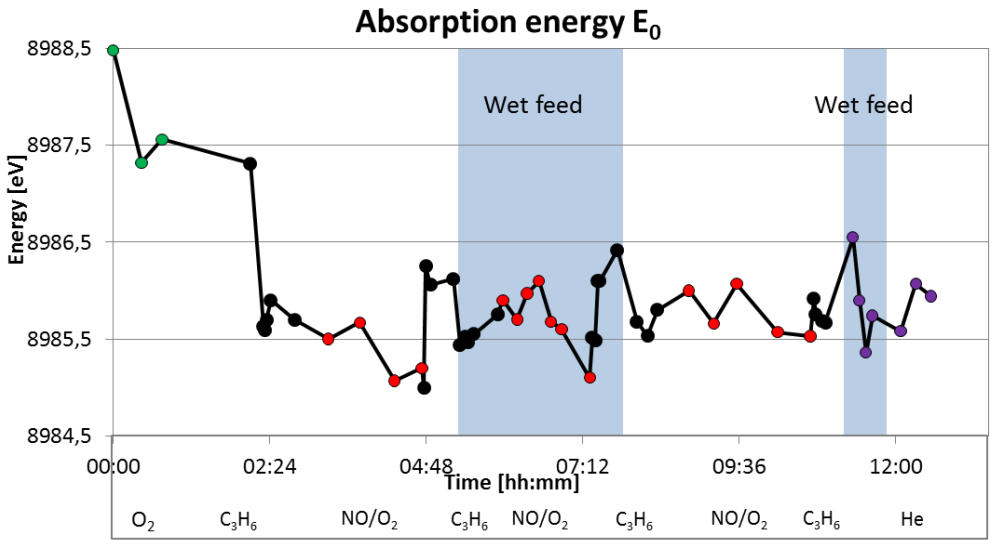

Figure 4.20: Positions of absorption energy, E_0, during *in-situ* redox experiment with hierarchical H-SAPO34-2. The marker colors indicate the feed, which is also displayed underneath the timeline: green=O_2, black=propene, red=NO and purple=He. The blue background indicates wet feed.

The only conclusion which could be drawn from Figure 4.20 is that the absorption energy is not characteristic for measurements of reduction and oxidation of copper species. The shape of the XANES region is no doubt a much better indicator for differentiating between Cu(I) and Cu(II). Once the XANES spectra have been normalized, the height of the pre-edge feature, caused by a 1s-4p transition, relative to the height of the post-edge line is quite characteristic, and a good measure of the fraction of monovalent versus divalent Cu atoms within the X-ray spot size. Figure 4.21 displays the pre-edge heights for the selected spectra in Figure 4.20 which exhibit a pre-edge. When propene feed is applied, the Cu(II) is clearly reduced to Cu(I), and when the propene feed is replaced with NO, the pre-edge immediately begins to decrease, indicating oxidation from Cu(I) to Cu(II).

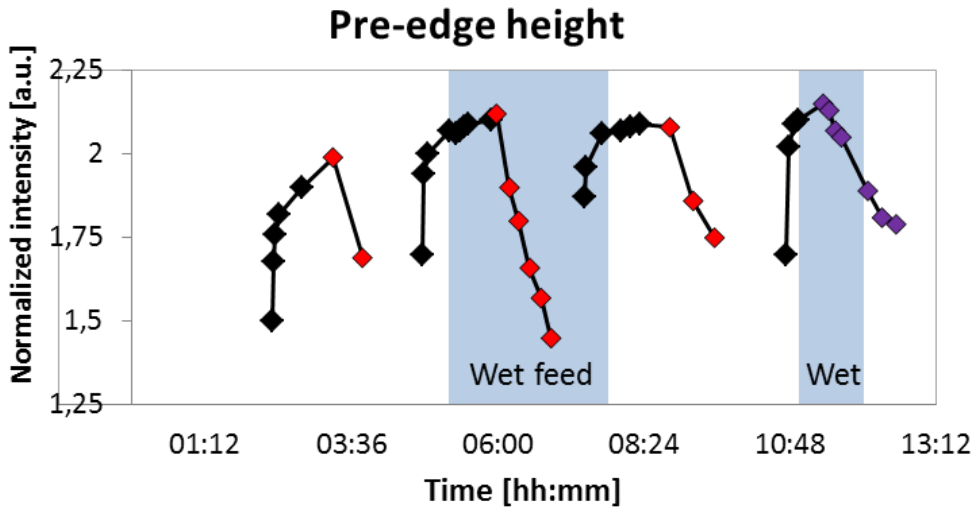

Figure 4.21: Pre-edge height on normalized XANES features measured during *in-situ* redox experiment of hierarchical H-SAPO34-2. The marker colors indicate the feed: black=propene, red=NO and purple=He. The blue background indicates wet feed. The sections between curves are where no pre-edge feature could be observed.

The reduction of Cu(II) by propene is much more rapid than oxidation of Cu(I) by NO. The position of the markers along the timeline show that once the propene feed was switched on, the pre-edge was very quickly restored, while the final stabilization takes somewhat more time. When the feed was switched to NO, the pre-edge decreased much slower before stabilizing.

The presence of water does not seem to have much effect on the redox properties of the material. However, the Cu(I) pre-edge height decreased further in wet NO/O2, indicating higher amounts of Cu(II) in the Cu(II)/Cu(I) mixture than in dry NO/O2. This effect is cancelled in dry feed, meaning that the initial redox behavior is restored in dry feed. The Cu(I) pre-edge is similar in dry feed and wet feed, which and the process continues unhindered. This is a sign of good hydrothermal stability, which is a very important property for SCR catalysts. The reversibility of the different electronic states is also imperative for catalytic activity.

4.7.2. EXAFS

Figure 4.22 shows the results of least-squares refinements of the nearest neighboring Cu-O shell distance and multiplicity for the redox cycling experiment at 350 °C for the hierarchical Cu-H-SAPO-34 (3.9 wt% Cu). The results are compared to those obtained for the Cu-aerogel (8 wt% Cu) from the works of Kristiansen *et al.*[70] The hierarchical Cu-H-SAPO-34 is presented with orange line and diamond markers in the figure, while the blue line/round markers represent the Cu-aerogel.

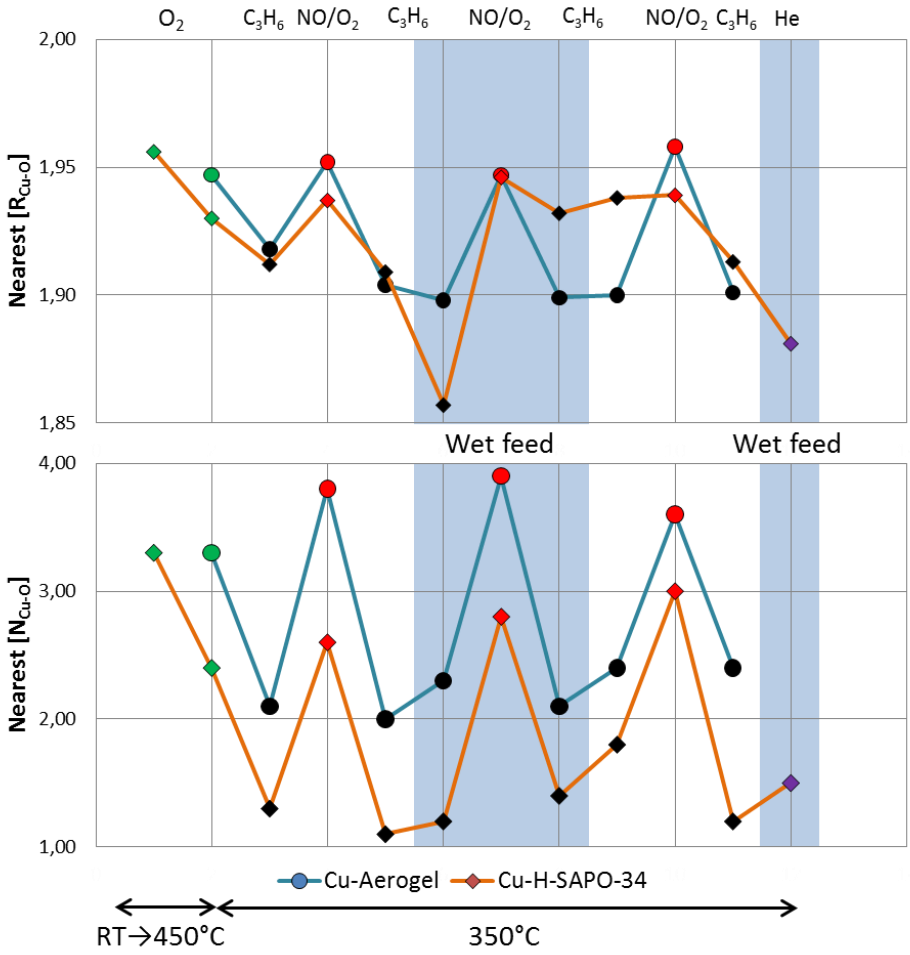

Figure 4.22: Least-squares refinements of nearest Cu-O shell during in-situ redox experiment of sample Cu-H-SAPO34-2 (3.9 wt% Cu) and a Cu-Aerogel from the work of Kristiansen *et al.*[70] Interatomic distances (top) and multiplicities (bottom) during cycling in propene and NO/O_2, and dry/wet feed. Atmosphere is indicated at the very top and by the color of the marker fill; green=O_2, black=propene, red=NO/O_2 and purple=Helium. The tabular values for all refined samples are shown in Appendix E.

The main conclusion to be drawn from these results is that the copper sites are reversibly affected by the change of feed. The repeated reductions and oxidations do produce copper oxides which are able to reduce back to monovalent copper. Even the introduction of steam at high temperatures has no bearing on the material's durability.

The multiplicity generally follows the trend of the Cu-aerogel, however some deviations are observed in the Cu-O interatomic distances, most notably the first section with propene in wet feed. An unusually distance is observed, and whatever the reason, the process is reversible.

5. Discussion

The main purpose of this thesis was two-fold. The first goal was to establish through several scientific techniques whether the synthesized, supposedly hierarchical SAPO-34 material actually contained mesopores, by comparing it to the conventional SAPO-34. If this could be confirmed, then the sample could by right be named hierarchical and further investigations of the materials functional properties could proceed.

Secondly, provided a successful completion of the primary goal, a more practical hypothesis could be probed: Is the hierarchical SAPO-34, containing Cu species, more active for the selective catalytic reduction of NO with propene than the conventional SAPO-34? Catalysis experiments and *in-situ* X-ray absorption spectroscopy was applied for this objective.

5.1 The porous nature of hierarchical SAPO-34

The micropores inherent in the SAPO-34 structure are guaranteed once the chabazite topology has been confirmed. Therefore no additional methods are required to test for their presence. With the exception of ICP-MS, the rest of the general characterization techniques were all directed towards the objective of identifying mesopores in the SAPO-34 particles. These techniques include thermogravimetric analysis and simultaneous differential scanning calorimetry, N_2-physisorption, coke deposition and CHN elemental analysis.

Beginning with the thermogravimetric analysis of as synthesized samples, there is not much to compare to in the literature. Cui *et al.*[45] reported significant differences in both end mass loss and the rates of mass loss before the main event, dependent on mesopore volume. A slight difference in end mass loss could be detected between conventional and hierarchical SAPO-34 in this project, although, smaller than reported differences. In addition, no significant difference in mass loss rate could be observed between water evaporation event and the TEAOH template combustion. As mentioned, an excessively high ramping rate could possibly be responsible for the lack of obvious difference, but the initial TGA data does not point to a sample containing a substantial degree of mesopores in the hierarchical SAPO-34.

N_2-adsorption-desorption isotherms did not show hysteresis loops to such an extreme degree, as was observed by Yang *et al.*,[2] or by Zhu *et al.*[10] However, Yang *et al.*[3] and Cui *et al.*[45] both

report hysteresis plots more in line with the results here obtained. Arguably, the isotherms can take many shapes, and the degree of hysteresis is not necessarily in linear proportion with the specific volume of mesopores. The pore size distributions point to mesopores present in the hierarchical SAPO-34 of sizes around 6 nm. This corresponds to the wide distribution of pore sizes exhibited in the literature[2] of the identical procedure, beginning at 4 nm, with a broad tail stretching to 12 nm.

Following deposition of carbonaceous species onto the sample powders, it was established, through elemental analysis, that the hierarchical SAPO-34 accumulated much more coke than the conventional. Temperature-programmed desorption and subsequent elemental analysis of the coked sample also revealed that the same amount of coke remained on the sample. By linking this information to the almost identical micropore volumes between conventional and hierarchical SAPO-34, this is a very strong sign that the remaining coke was situated in the micropores, and that the excess coke on hierarchical SAPO-34 had been located in the mesopores/macropores.

The post-coke N_2-physisorption results also show a clear hysteresis on the hierarchical SAPO-34 which is not present on the conventional. These results also lead towards mesoporosity in the hierarchical SAPO-34, and at the same time shows that the coke had not clogged the mesopores.

5.2 Selective catalytic reduction and hydrothermal stability

Figure 4.18, which shows the NO conversion in dry and wet feed, provides very useful information about the samples as SCR-catalysts. This SCR-HC-deNO_X experiment was used as a test reaction to identify SCR activity, compare activity and probe the effects of water on the materials during reaction. However, the results cannot be understood as absolutely comparable. The main source of dispute is different copper loadings for the three samples, conventional (1.4 wt%), hierarchical (3.9 wt%) and incorporated conventional (6.8 wt%) SAPO-34. Due to the increased number of active sites for increases metal loading, the conversion often increases too, while the turn-over frequency per active site might not be affected. Taking the loading into account it is still reasonable to argue that the difference between the conventional and hierarchical SAPO-34 is quite large, and that hierarchical

SAPO-34 is active at lower temperatures than conventional SAPO-34. Also noteworthy, is the proximity between hierarchical and incorporated conventional for many of the data points, still considering the difference in Cu loading. This points towards better properties for the hierarchical material, than for the other two samples.

Interestingly, the water feed does not seem to have a particularly adverse effect on any of the samples with respect to NO conversion, or N_2 yield. The conversions are quite similar at 400 and 450 °C, and the minimum temperature for activity is decreased, which is positive.

The redox cycling experiment at 350 °C in dry and wet feed was also compared to the aforementioned study, and the general features were quite similar. The most important information which can be extracted is the reversibility of the copper sites, and this is reflected both in the EXAFS Cu-O interatomic distances, $R_{Cu\text{-}O}$, and first shell multiplicity, $N_{Cu\text{-}O}$, as well as in the XANES pre-edge height. The copper species alternate freely and reversibly in spite of the harsh steaming conditions. The results prove reasonably good hydrothermal stability. When using the pre-edge feature as indicator of valence state fractions, it is generally considered more accurate to use the peak-fitting function in the Athena software.[71] For this purpose, however, which was mainly to corroborate the EXAFS data in analysis of the material's hydrothermal stability and oxidative reversibility, measuring normalized pre-edge height well-suited. The advantage is that rapid analysis of many spectra is done with ease, even for inexperienced users, while peak-fitting is very time consuming and would be poorly suited for measuring the forty data points presented in Figure 4.21. It was the large amount of data points which made presenting the different reaction times facile, *i.e.* that the initial reduction of copper is much faster than the reverse oxidation.

The catalytic and spectroscopic experiments from the work of Kristiansen *et al.*[70] have been replicated in this theses and it is therefore natural to compare the studies at this point. The study was focused mainly on Cu-aerogels, which is interesting to compare to hierarchical SAPO-34 because they both contain mesopores, in contrast to conventional zeolites. The main differences are that aerogels lack acidity, are hydrophobic, and have higher surface areas. From the SCR-HC-deNO_X experiment it is known that the conversion at 350 °C would be 13% in dry feed and 15% in wet feed for hierarchical SAPO-34 (3.9 wt%), compared to 15% in dry feed and ~30% in wet feed for aerogel of similar copper loading (3.5 wt%).

6. Conclusions

The sum of evidence without a doubt identifies the presence of mesopores in the hierarchical SAPO-34 material, making it worthy of its sample name. The average mesopore diameter is 6 nm, although the pore size distribution stretches to around 10 nm. Many of the accumulated results point to a moderate amount of mesopores.

Hierarchical SAPO-34 ion-exchanged with copper is active for selective catalytic reduction with propene (HC-SCR) of NO_X, both in dry and wet feed. The presence of water at high temperatures does not have much of an effect on catalytic activity in either direction. The material has exhibited good hydrothermal stability during cycling of reaction feed, and no irreversible effects have been observed on the copper content or the pore structure. Reduction of Cu(I) to Cu(II) is faster than the corresponding oxidation.

7 Further work

The present ideas for further work are directed mainly towards functionalization of the materials and also catalytic measurements, with corresponding *in-situ* XAS analysis.

Firstly, the copper loading within samples would preferably be tuned so that the catalytic measurements and XAS analysis could be compared without having to take into account the difference in weight percent. Also, two or more different copper loadings on each sample could be prepared in order to optimize the loading with respect to performance versus price. *In-situ* XAS redox cycling, combined with catalytic measurements, of a conventional SAPO-34 with similar copper loading as the hierarchical Cu-H-SAPO-34 would make a very useful comparison.

Many different catalytic experiments are available in order to push the boundaries of the catalyst, and gain knowledge about its nature. Specifically Time-on-stream at operating temperature would be interesting, considering the coke deposition results. It is now established that the hierarchical samples accumulate more coke within a given time window, but the literature states that conventional SAPO-34 cokes much quicker during the MTO reaction than hierarchical samples.

Currently, small amounts of hierarchical H-SAPO34-2, and -3 are being investigated with High resolution transmission electron microscopy (HR-TEM) at the University of Glasgow, in order to gain information on the mesopores, however, analyses are not yet complete. Applying such a technique on zeotypes is quite challenging, and it will be exciting to see if the experts are able determine anything new about the pore system.

8. References

1. K. Momma and F. Izumi, *Journal of Applied Crystallography*, 2011, 44, 1272-1276.
2. H. Yang, Z. Liu, H. Gao and Z. Xie, *Journal of Materials Chemistry*, 2010, 20, 3227-3231.
3. S.-T. Yang, J.-Y. Kim, H.-J. Chae, M. Kim, S.-Y. Jeong and W.-S. Ahn, *Materials Research Bulletin*, 2012, 47, 3888-3892.
4. J. Perez-Ramirez, C. H. Christensen, K. Egeblad, C. H. Christensen and J. C. Groen, *Chemical Society Reviews*, 2008, 37, 2530-2542.
5. H. Yahiro and M. Iwamoto, *Applied Catalysis A: General*, 2001, 222, 163-181.
6. S. E. Manahan, *Environmental chemistry*, Ninth edn., 2010.
7. I. Chorkendorff and J. W. Niemantsverdriet, in *Concepts of Modern Catalysis and Kinetics*, Wiley-VCH Verlag GmbH & Co. KGaA, 2005, DOI: 10.1002/3527602658.ch10, pp. 377-400.
8. T. Ishihara, M. Kagawa, F. Hadama and Y. Takita, *Journal of Catalysis*, 1997, 169, 93-102.
9. M. Y. Kustova, S. B. Rasmussen, A. L. Kustov and C. H. Christensen, *Applied Catalysis B: Environmental*, 2006, 67, 60-67.
10. J. Zhu, Y. Cui, Y. Wang and F. Wei, *Chemical Communications*, 2009, DOI: 10.1039/B902661D, 3282-3284.
11. J. Wasserstrom, in *Slate*, 2013, ch. Foreigners.
12. S. Roy and A. Baiker, *Chem Rev*, 2009, 109, 4054-4091.
13. I. Chorkendorff and J. W. Niemantsverdriet, in *Concepts of Modern Catalysis and Kinetics*, Wiley-VCH Verlag GmbH & Co. KGaA, 2005, DOI: 10.1002/3527602658.ch1, pp. 1-21.
14. I. Chorkendorff and J. W. Niemantsverdriet, in *Concepts of Modern Catalysis and Kinetics*, Wiley-VCH Verlag GmbH & Co. KGaA, 2005, DOI: 10.1002/3527602658.ch5, pp. 167-214.
15. P. Granger and V. I. Parvulescu, *Chemical Reviews*, 2011, 111, 3155-3207.
16. Y. Zhang and M. Flytzani-Stephanopoulos, *Journal of Catalysis*, 1996, 164, 131-145.
17. N. Takahashi, H. Shinjoh, T. Iijima, T. Suzuki, K. Yamazaki, K. Yokota, H. Suzuki, N. Miyoshi, S.-i. Matsumoto, T. Tanizawa, T. Tanaka, S.-s. Tateishi and K. Kasahara, *Catalysis Today*, 1996, 27, 63-69.
18. G. D. Lionta, S. C. Christoforou, E. A. Efthimiadis and I. A. Vasalos, *Industrial & Engineering Chemistry Research*, 1996, 35, 2508-2515.
19. H. Nishiguchi, S. Kimura, T. Ishihara and Y. Takita, *Research on Chemical Intermediates*, 1998, 24, 391-399.
20. J. Liang, H. Li, S. Zhao, W. Guo, R. Wang and M. Ying, *Applied Catalysis*, 1990, 64, 31-40.
21. P. Atkins, *Shriver and Atkins' Inorganic Chemistry*, Oxford University Press, 2010.
22. R. F. Lobo, M. Tsapatsis, C. C. Freyhardt, S. Khodabandeh, P. Wagner, C.-Y. Chen, K. J. Balkus, S. I. Zones and M. E. Davis, *Journal of the American Chemical Society*, 1997, 119, 8474-8484.
23. Z. International, http://www.zeolyst.com/our-products/standard-zeolite-powders/zsm-5.aspx, http://www.zeolyst.com/our-products/standard-zeolite-powders/zsm-5.aspx, Accessed 29. april, 2014.
24. I. Yamane and T. Nakazawa, in *Studies in Surface Science and Catalysis*, eds. A. I. Y. Murakami and J. W. Ward, Elsevier, 1986, vol. Volume 28, pp. 991-1000.
25. S. Li, J. L. Falconer and R. D. Noble, *Advanced Materials*, 2006, 18, 2601-2603.
26. M. Hartmann and L. Kevan, *Chemical reviews*, 1999, 99, 635-664.
27. F. Schmidt, S. Paasch, E. Brunner and S. Kaskel, *Microporous and Mesoporous Materials*, 2012, 164, 214-221.
28. S. Wilson and P. Barger, *Microporous and Mesoporous Materials*, 1999, 29, 117-126.
29. C. Baerlocher, L. B. McCusker, D. Olson and W. M. Meier, *Atlas of zeolite framework types*, Published on behalf of the Structure Commission of the International Zeolite Association by Elsevier, Amsterdam, 2007.

30. S. W. Kaiser, Google Patents, 1985.
31. B. M. Lok, C. A. Messina, R. L. Patton, R. T. Gajek, T. R. Cannan and E. M. Flanigen, Google Patents, 1984.
32. S. T. Wilson, B. M. Lok and E. M. Flanigen, Google Patents, 1982.
33. I. M. Dahl, H. Mostad, D. Akporiaye and R. Wendelbo, *Microporous and Mesoporous Materials*, 1999, 29, 185-190.
34. K. S. W. Sing, D. H. Everett, R. A. W. Haul, L. Moscou, R. A. Pierotti, J. Rouquerol and T. Siemieniewska, in *Handbook of Heterogeneous Catalysis*, Wiley-VCH Verlag GmbH & Co. KGaA, 2008, DOI: 10.1002/9783527610044.hetcat0065.
35. J. C. Groen, L. A. A. Peffer and J. Perez-Ramrez, *Microporous and Mesoporous Materials*, 2003, 60, 1-17.
36. D. Chen, H. P. Rebo, K. Moljord and A. Holmen, in *Studies in Surface Science and Catalysis*, eds. C. H. Bartholomew and G. A. Fuentes, Elsevier, 1997, vol. Volume 111, pp. 159-166.
37. D. Chen, H. P. Rebo and A. Holmen, *Chemical Engineering Science*, 1999, 54, 3465-3473.
38. Z. Li, J. Martínez-Triguero, P. Concepción, J. Yu and A. Corma, *Physical Chemistry Chemical Physics*, 2013, 15, 14670-14680.
39. H. van Heyden, S. Mintova and T. Bein, *Chemistry of Materials*, 2008, 20, 2956-2963.
40. Y. Tian, L. Fan, Z. Wang, S. Qiu and G. Zhu, *J. Mater. Chem.*, 2009, 19, 7698-7703.
41. T. Fjermestad, S. Svelle and O. Swang, *The Journal of Physical Chemistry C*, 2013, 117, 13442-13451.
42. T. Fjermestad, M. Zokaie, S. Svelle and O. Swang, 2013.
43. L. R. Aramburo, J. Ruiz-Martínez, L. Sommer, B. Arstad, R. Buitrago-Sierra, A. Sepúlveda-Escribano, H. W. Zandbergen, U. Olsbye, F. M. F. de Groot and B. M. Weckhuysen, *ChemCatChem*, 2013, 5, 1386-1394.
44. J. Yao, H. Wang, S. P. Ringer, K.-Y. Chan, L. Zhang and N. Xu, *Microporous and Mesoporous Materials*, 2005, 85, 267-272.
45. Y. Cui, Q. Zhang, J. He, Y. Wang and F. Wei, *Particuology*, 2013, 11, 468-474.
46. K. Möller, B. Yilmaz, R. M. Jacubinas, U. Müller and T. Bein, *Journal of the American Chemical Society*, 2011, 133, 5284-5295.
47. J. Kim, M. Choi and R. Ryoo, *Journal of Catalysis*, 2010, 269, 219-228.
48. J. W. Cahn, *Acta Metallurgica*, 1961, 9, 795-801.
49. M. Zamadics, X. Chen and L. Kevan, *The Journal of Physical Chemistry*, 1992, 96, 2652-2657.
50. M. Zamadics, X. Chen and L. Kevan, *The Journal of Physical Chemistry*, 1992, 96, 5488-5491.
51. K. Mathisen, D. G. Nicholson, A. M. Beale, M. Sanchez-Sanchez, G. Sankar, W. Bras and S. Nikitenko, *The Journal of Physical Chemistry C*, 2007, 111, 3130-3138.
52. E. L. Uzunova, H. Mikosch and J. Hafner, *The Journal of Physical Chemistry C*, 2008, 112, 2632-2639.
53. E. L. Uzunova, F. Göltl, G. Kresse and J. Hafner, *The Journal of Physical Chemistry C*, 2009, 113, 5274-5291.
54. R. Martínez-Franco, M. Moliner, C. Franch, A. Kustov and A. Corma, *Applied Catalysis B: Environmental*, 2012, 127, 273-280.
55. M. Newville, *Consortium for Advanced Radiation Sources, University of Chicago (USA)[http://xafs. org]*, 2004.
56. D. C. Koningsberger, B. L. Mojet, G. E. van Dorssen and D. E. Ramaker, *Topics in Catalysis*, 2000, 10, 143-155.
57. T. Kristiansen, J. A. Stovneng, M. A. Einarsrud, D. G. Nicholson and K. Mathisen, *Journal of Physical Chemistry C*, 2012, 116, 20368-20379.
58. K. Mathisen, M. Stockenhuber and D. G. Nicholson, *Physical chemistry chemical physics : PCCP*, 2009, 11, 5476-5488.

59. T. Kristiansen, K. Mathisen, M. A. Einarsrud, M. Bjorgen and D. G. Nicholson, *Journal of Physical Chemistry C*, 2011, 115, 19260-19268.
60. E. S. R. F. (ESRF), http://www.esrf.eu/about/synchrotron-science/synchrotron.
61. J. Ghijsen, L. Tjeng, J. Van Elp, H. Eskes, J. Westerink, G. Sawatzky and M. Czyzyk, *Physical Review B*, 1988, 38, 11322.
62. H. A. Jahn and E. Teller, *Proceedings of the Royal Society of London. Series A, Mathematical and Physical Sciences*, 1937, 220-235.
63. J. Niemantsverdriet, *Spectroscopy in Catalysis*, Wiley-VCH, 2008.
64. G. Fagerlund, *Mat. Constr.*, 1973, 6, 239-245.
65. S. J. Gregg and K. S. W. Sing, *Adsorption, surface area and porosity*, Academic Press, London, 1982.
66. E. P. Barrett, L. G. Joyner and P. P. Halenda, *Journal of the American Chemical Society*, 1951, 73, 373-380.
67. R. Pierotti and J. Rouquerol, *Pure Appl Chem*, 1985, 57, 603-619.
68. V. S. Ramachandran and J. J. Beaudoin, *Handbook of analytical techniques in concrete science and technology: principles, techniques and applications*, Elsevier, 2000.
69. L. J. France, D. C. Apperley, E. J. Ditzel, J. S. J. Hargreaves, J. P. Lewicki, J. J. Liggat and D. Todd, *Catalysis Science & Technology*, 2011, 1, 932-939.
70. T. Kristiansen and K. Mathisen, *J. Phys. Chem. C*, 2014, 118, 2439-2453.
71. á. Ravel and M. Newville, *Journal of synchrotron radiation*, 2005, 12, 537-541.

9 Appendices

Appendix A: Risk evaluation

Enhet: Inst for kjemi **Dato: 26.8.2012**
Linjeleder: Marie-Laure Olivier
Deltakere ved risikovurderingen (m/ funksjon): Karina Mathisen (førsteamanuensis), Trygve Jakobsen (Msc kandidat)

ID nr	Aktivitet fra kartleggings-skjemaet	Mulig uønsket hendelse/ belastning	Vurdering av sannsyn-lighet (1-5)	Vurdering av konsekvens: Mennesk e (A-E)	Ytre miljø (A-E)	Øk/ materiell (A-E)	Om-dømme (A-E)	Risiko-verdi	Kommentarer/status Forslag til tiltak
E2-117 - 1	Uorganisk syntese	Inhalering/søl/spill av organisk amin på hud evt øyner	2	A	A	A	A	2A	Hansker, briller, avtrekk
		Søl/spill av syre/base på hud evt øyner	4	A	A	A	A	4A	Hansker og briller. Kun fortynnede syrer.
		Inhalering fint silikapulver	2	A	A	A	A	2A	
		Overtrykk							Ikke vurdert helsefarlig i små mengder v/ sjelden eksponering. Ansiktsmasker?

		høytrykksautoklav kan gi eksplosjon	2	B	A	A	A	2B	Opplæring gis. Sikkerhetsventil innstallert på alle autoklaver.
E2-117 - 2	Arbeid med HF	Søl/spill på hud evt øyner	1	C	B	B	B	1C	Krever flussyrekurs, godkjent beskyttelsesutstyr og følgeperson
E2-117 - 3	Bruk av høytemperaturovn (inntil 1200 grader)	Forbrenningsskader, amin avgasser, mulig produksjon av CO ved kalsinering	2	A	A	A	A	2A	Thermoresistente hansker, opplæring kreves. Ovn plassert i avtrekk.
E2-117 - 4	Vask med Kongevann	Søl/spill på hud evt øyner.Utvikling av gass.	2	A	A	A	A	2A	Hansker, briller og avtrekk. Vaskeprosedyre gitt i tilfelle søl. Krever følgeperson.
E2-117 – 11	Ionebyttingsprosedyrer	Søl/spill av syre eller baser på hud evt øyner	4	A	A	A	A	4A	Hansker og briller. Fortynnede syrer og baser.
E2-117 – 14	Jones reduktor	Søl/spill av syre på hud evt øyner. Utvikling av hydrogen gass.	4	A	A	A	A	4A	Hansker, briller og avtrekk. Fortynnede syrer og baser.
E2-117 – 16	Arbeid med flytende nitrogen	Forfrysningsskader	2	A	A	A	A	2A	Ansiktskjerm og hansker
E2-117 – 18	Arbeid med forskjellige typer gass	Gasslekkasje. Eksplosjonsfare. Kvelning.	2	C	A	C	C	2C	Gassdetektor for hydrogen, CO og hydrokarboner er installert. Jobbe alene alarm ved bruk av CO. Gassflasker ikke over 10 liter, festet på vegg etter forskrifter. Krever

									opplæring. Laben er utstyrt med kortlås for å unngå tilgang for uvedkommede.
E2-117 - 19	Arbeid med syrer og baser	Søl/spill av syre på hud evt øyner.	4	A	A	A	A	4A	Hansker og briller. Kun bruk av fortynnede syrer og baser. Mye til vasking.
E2-117-21	Katalysemålinger i in situ celle	Gasslekkasje, forbrenning	3	B				3B	Åpen varmekilde, nytt oppsett bestilt (se E2-117-22). For gass se E2-117-18.
E2-117-22	Katalysemålinger i tubeovn	Gasslekkasje, forbrenning	1	B				1B	Lukket varmesystem. For gass se E2-117-18.
KLB 1	XRD instrumentanalyse	Röntgenstråler	1	C				1C	Ingen reell eksponeringsfare
KLB 2	XAS dataopptak	Elektrisk støt Forbrenningsskade Eksponering for röntgenstråler Rahmanlaser	3 3 1 1	B B C B				3B 3B 1C 1B	24 V spenningskilde Åpen varmekilde Gjøres alltid under tilsyn. Egne strenge sikkerhetstiltak ved ESRF og Maxlab Grønn laser, 532 nm. Lav intensitet, brukes eget øyevern.
KLB 3	TGA instrumentanalyse	Gasslekkasje, forbrenning	1	B				1B	Opplæring gis på forhånd
KLB 4	ICP-MS instrumentanalyse	Søl/spill av HF og HNO_3 på hud evt. øyne	1	C	B	B	B	1C	Krever godkjent beskyttelsesutstyr og opplæring gis på forhånd

Konsekvens ***Risikoverdi (beregnes hver for seg):***

Sannsynlighet vurderes etter følgende kriterier:

Svært liten 1	Liten 2	Middels 3	Stor 4	Svært stor 5
1 gang pr 50 år eller sjeldnere	1 gang pr 10 år eller sjeldnere	1 gang pr år eller sjeldnere	1 gang pr måned eller oftere	Skjer ukentlig

Konsekvens vurderes etter følgende kriterier:

Gradering	Menneske	Ytre miljø Vann, jord og luft	Øk/materiell	Omdømme
E **Svært Alvorlig**	Død	Svært langvarig og ikke reversibel skade	Drifts- eller aktivitetsstans >1 år.	Troverdighet og respekt betydelig og varig svekket
D **Alvorlig**	Alvorlig personskade. Mulig uførhet.	Langvarig skade. Lang restitusjonstid	Driftsstans > ½ år Aktivitetsstans i opp til 1 år	Troverdighet og respekt betydelig svekket
C **Moderat**	Alvorlig personskade.	Mindre skade og lang restitusjonstid	Drifts- eller aktivitetsstans < 1 mnd	Troverdighet og respekt svekket
B **Liten**	Skade som krever medisinsk behandling	Mindre skade og kort restitusjonstid	Drifts- eller aktivitetsstans < 1uke	Negativ påvirkning på troverdighet og respekt
A **Svært liten**	Skade som krever førstehjelp	Ubetydelig skade og kort restitusjonstid	Drifts- eller aktivitetsstans < 1dag	Liten påvirkning på troverdighet og respekt

Risikoverdi = Sannsynlighet x Konsekvens

Beregn risikoverdi for Menneske. Enheten vurderer selv om de i tillegg vil beregne risikoverdi for Ytre miljø, Økonomi/materiell og Omdømme. I så fall beregnes disse hver for seg.

Til kolonnen ”Kommentarer/status, forslag til forebyggende og korrigerende tiltak”:
Tiltak kan påvirke både sannsynlighet og konsekvens. Prioriter tiltak som kan forhindre at hendelsen inntreffer, dvs. sannsynlighetsreduserende tiltak foran skjerpet beredskap, dvs. konsekvensreduserende tiltak.

Appendix B: Additional diffractograms

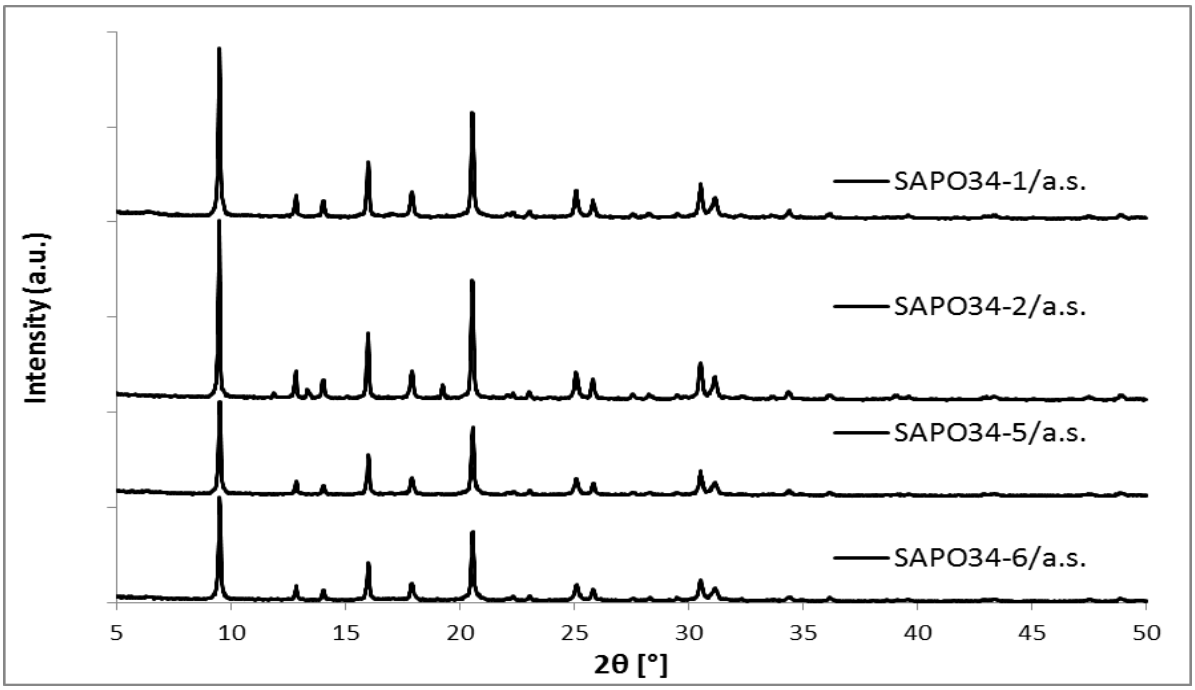

Figure 9.1: Powder diffraction patterns of as synthesized conventional samples SAPO34-(1, 2, 5 and 6).

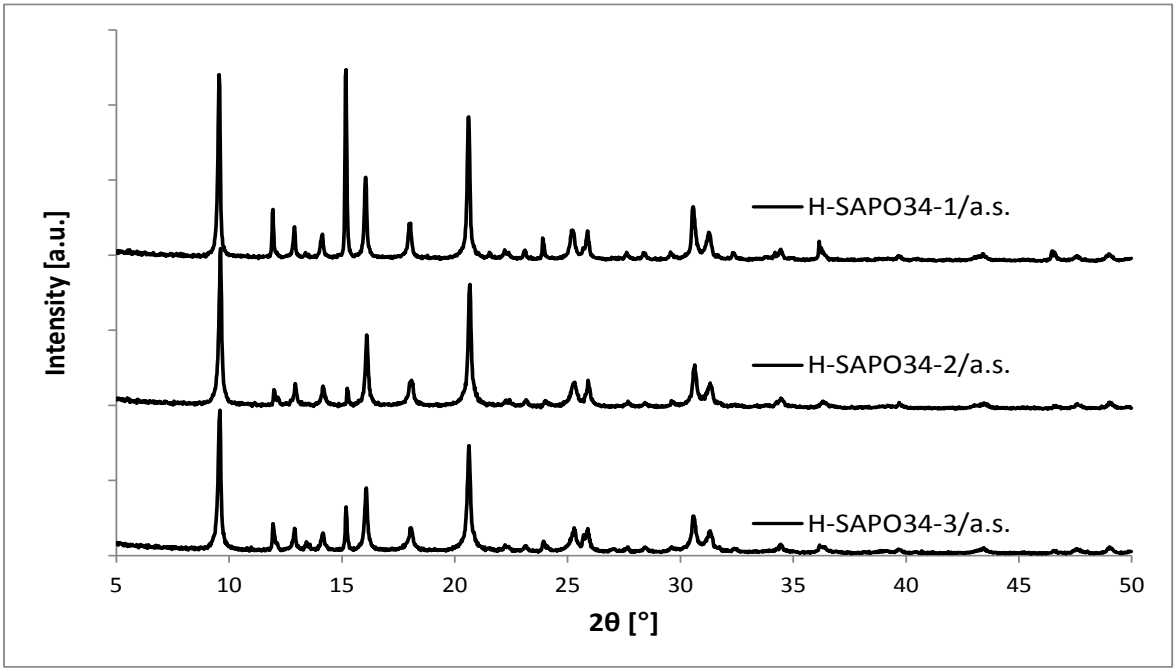

Figure 9.2: Powder diffraction patterns of as synthesized hierarchical samples H-SAPO34-(1-3)

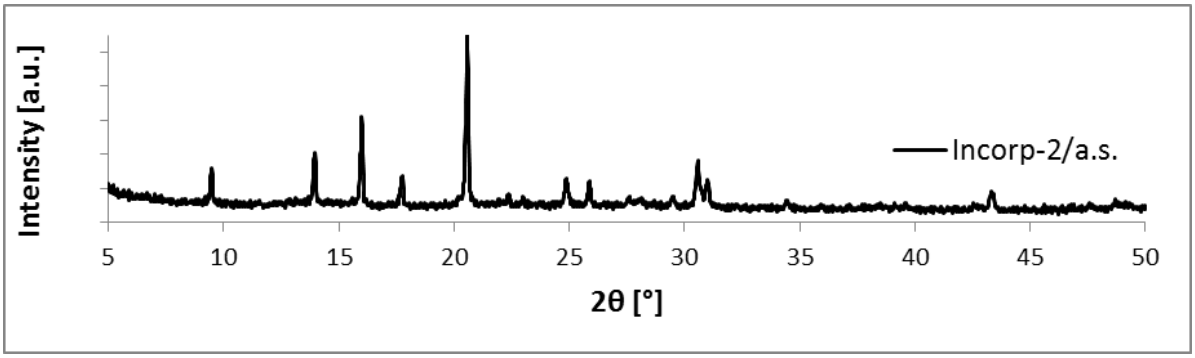

Figure 9.3: Powder diffraction pattern of as synthesized incorporated CuSAPO-34 (Incorp-2).

Appendix C: TGA results before and after coke deposition

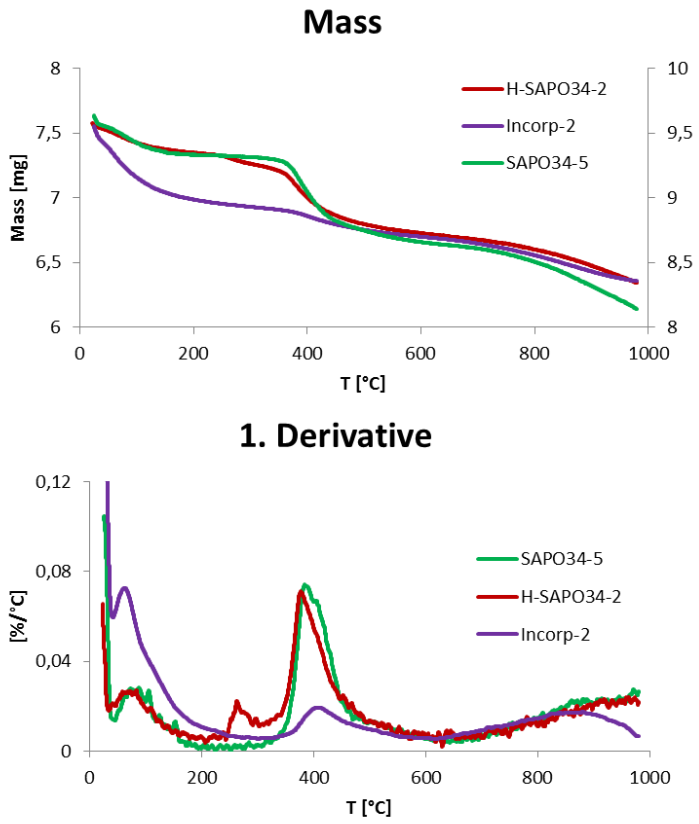

Figure 9.4: TPD profiles of conventional (green), hierarchical (red) and incorporated conventional (purple) SAPO-34 after coke deposition. Masses are shown up top, and 1. Derivative of masses at the bottom.

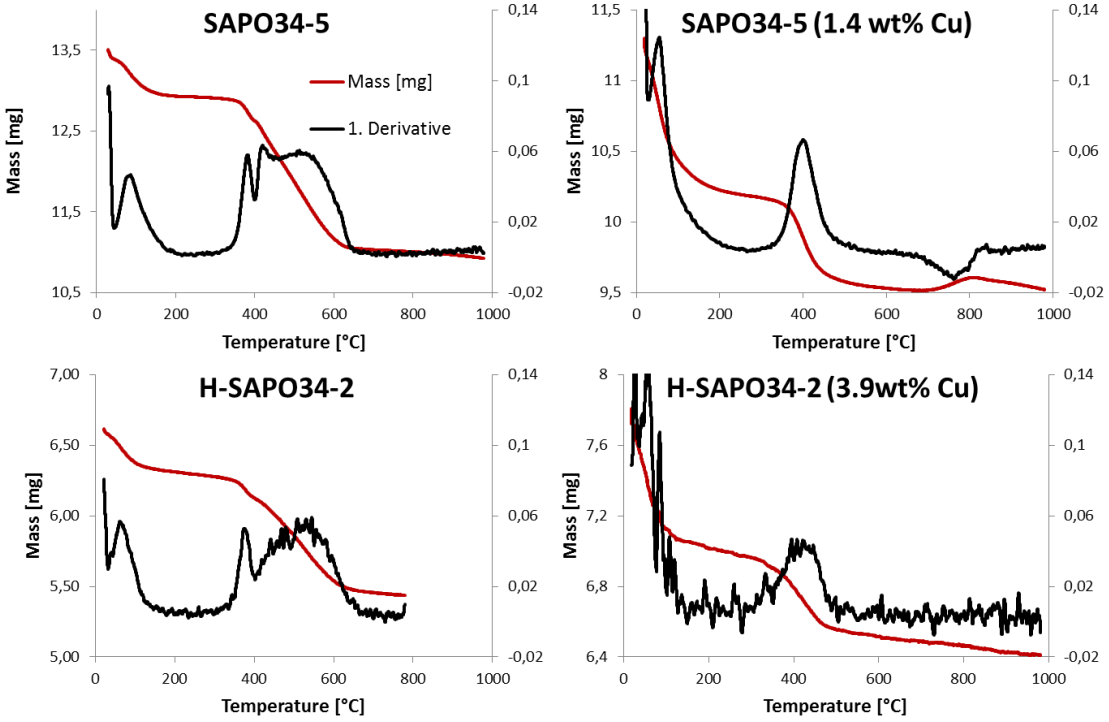

Figure 9.5: TPO profiles of conventional SAPO-34 with and without copper (top) and hierarchical SAPO-34 with and without copper (bottom). The red curves represent mass, and the black curves are 1. derivative of mass.

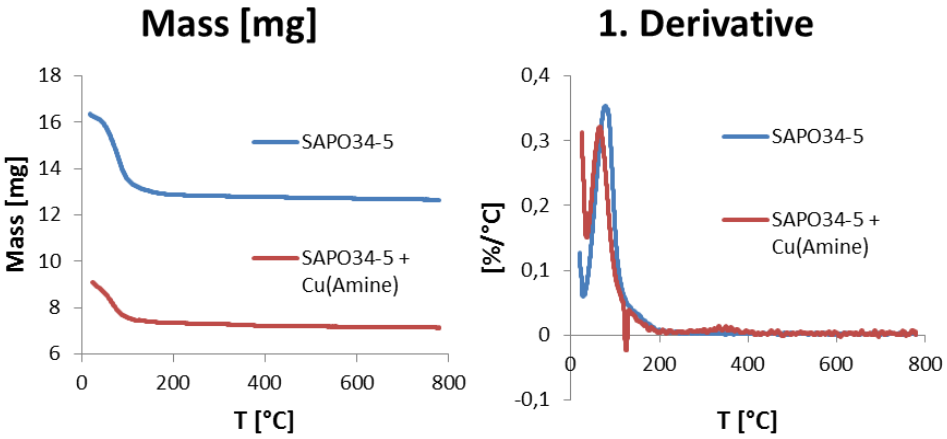

Figure 9.6: Conventional SAPO34-5 with (blue) and without (red) copper (1.4 wt%). Mass is shown on the left and 1. dreivative on the right.

Appendix D: TPR SCR-HC-deNO$_X$

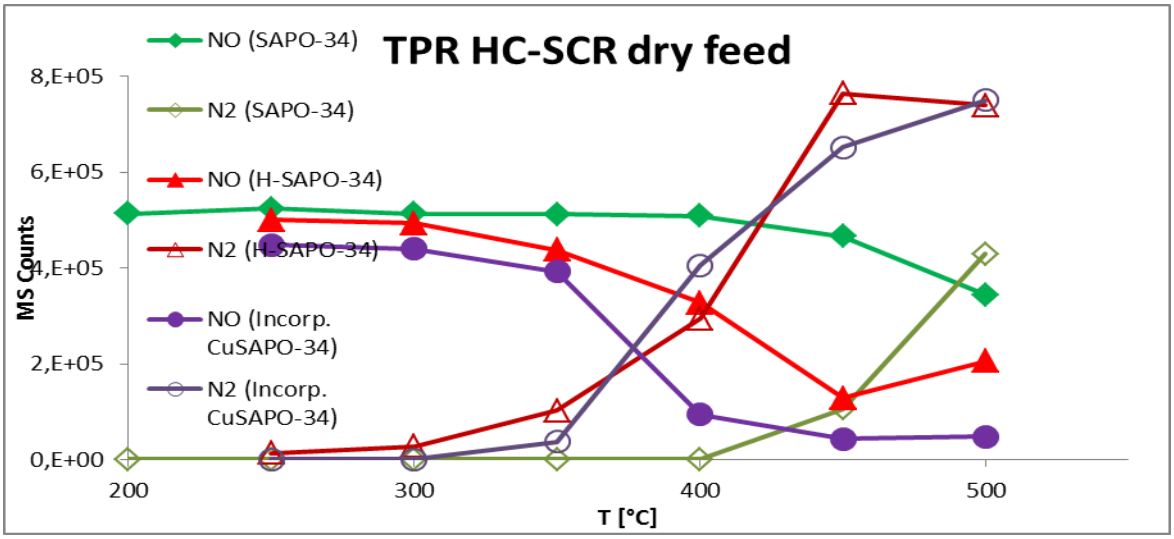

Figure 9.7: Temperature-programmed SCR-HC-deNOx in dry feed. The MS intensities of NO and N2 for for conventional, hierarchical and incorporated conventional SAPO-34 are shown in green, red and purple, respectively.

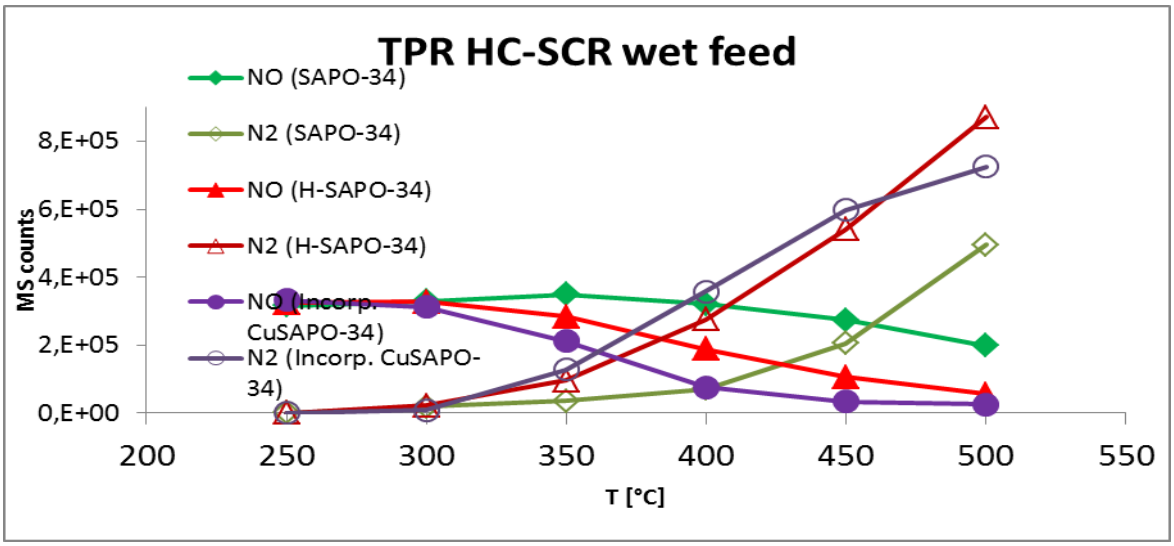

Figure 9.8: Temperature-programmed SCR-HC-deNOx in wet feed. The MS intensities of NO and N2 for for conventional, hierarchical and incorporated conventional SAPO-34 are shown in green, red and purple, respectively.

Appendix E: EXAFS refinements

Table 9.1: Results from EXAFS least-squares refinements collected at the Cu K-edge for the in-situ hierarchical H-SAPO34-2 (3.9 wt% Cu).

Ox. State	Section	T [°C]	Atm.	Shell	N	r [Å]	R [%]	E_F [eV]	AFAC	$2\sigma^2$ [Å^2]
1	Cu_2O	25	Sample holder	Cu-O	2	1,858(4)	35,79	-6,8(4)	0,74(3)	0,005(1)
				Cu--Cu	12	3,043(6)				0,041(2)
2	$Cu(OH)_2$	25	Sample holder	Cu-O	4	1,965	27,54	-5,466	0,7906	0,009(1)
				Cu-O	2	*			*	
				Cu---Cu	2	2,957				0,01(1)
				Cu---Cu	4	2,799				0,08(1)
2	1	25	O_2	Cu-O	3,3(1)	1,956(4)	32,22	-6,7(4)	0,7906	0,008(1)
				Cu-O	1,1(3)	2,28(3)				0,02(1)
2	2	450	O_2	Cu-O	2,4(1)	1,930(6)	45,49	-3,5(6)	0,79	0,013(2)
1	3	350	C_3H_6	Cu-O	1,3(1)	1,912(8)	45,44	-2,0(8)	0,74	0,009(2)
2	4	350	NO + O_2	Cu-O	2,6(1)	1,937(6)	39,14	-6,2(5)	0,7906	0,012(2)
1	5	350	C_3H_6	Cu-O	1,1(1)	1,909(7)	45,98	-3,2(8)	0,74	0,002(1)
1	6	350	C_3H_6 (wet)	Cu-O	1,2(1)	1,857(7)	46,9	1(1)	0,74	0,002(1)
2	7	350	NO + O_2 (wet)	Cu-O	2,8(1)	1,946(6)	37,67	-6,2(5)	0,7906	0,015(2)
1	8	350	C_3H_6 (wet)	Cu-O	1,4(1)	1,932(7)	39,75	-4,2(6)	0,74	0,008(2)
				Cu--Cu	1,5(1)	2,26(3)				0,04(1)
1	9	350	C_3H_6	Cu-O	1,8(1)	1,938(8)	43,2	-4,0(7)	0,74	0,012(2)
2	10	350	NO + O_2	Cu-O	3,2(2)	1,943(9)	53,45	-6,3(6)	0,7906	0,018(3)
1	11	350	C_3H_6	Cu-O	1,2(1)	1,913(7)	47,86	-4,1(9)	0,74	0,003(1)
1	12	350	He (Wet)	Cu-O	1,5(1)	1,881(8)	46,78	-2,6(8)	0,74	0,006(2)